

726640

RADC-TR-71-114  
Final Technical Report  
June 1971



## MEASUREMENT AND ANALYSIS OF SPECTRAL SIGNATURES

The Ohio State University

Approved for public release;  
distribution unlimited.

Reproduced by  
**NATIONAL TECHNICAL  
INFORMATION SERVICE**  
Springfield, Va. 22151

**Rome Air Development Center  
Air Force Systems Command  
Griffiss Air Force Base, New York**

When US Government drawings, specifications, or other data are used for any purpose other than a definitely related government procurement operation, the government thereby incurs no responsibility nor any obligation whatsoever; and the fact that the government may have formulated, furnished, or in any way supplied the said drawings, specifications, or other data is not to be regarded, by implication or otherwise, as in any manner licensing the holder or any other person or corporation, or conveying any rights or permission to manufacture, use, or sell any patented invention that may in any way be related thereto.

ACCESSION NO.	
CBTU	WHITE SECTION
280	DUFF SECTION <input type="checkbox"/>
REMARKS / JULY 1978	<input type="checkbox"/>
BY	
DISTRIBUTION/AVAILABILITY CODES	
004	MAIL 211/2 SPECIAL
<i>[Handwritten signature]</i>	

Do not return this copy. Retain or destroy.

UNCLASSIFIED

Security Classification

**DOCUMENT CONTROL DATA - R & D**

(Security classification of title, body of abstract and indexing annotation must be entered when the overall report is classified)

1. ORIGINATING ACTIVITY (Corporate author) The Ohio State University Department of Electrical Engineering Columbus, Ohio 43212	2a. REPORT SECURITY CLASSIFICATION UNCLASSIFIED
	2b. GROUP N/A

3. REPORT TITLE

MEASUREMENT AND ANALYSIS OF SPECTRAL SIGNATURES

4. DESCRIPTIVE NOTES (Type of report and inclusive dates)  
Final Report 24 February 1970 to 24 February 1971

5. AUTHOR(S) (First name, middle initial, last name)

ElectroScience Laboratory

6. REPORT DATE June 1971	7a. TOTAL NO. OF PAGES 92	7b. NO. OF REFS 13
8a. CONTRACT OR GRANT NO. F30602-69-C-0231  Job Order No. 45060000  Task No. 05	8b. ORIGINATOR'S REPORT NUMBER(S) OSURF 2784-2  9d. OTHER REPORT NO(S) (Any other numbers that may be assigned (this report) RADC-TR-71-114	

10. DISTRIBUTION STATEMENT

Approved for public release; distribution unlimited.

11. SUPPLEMENTARY NOTES RADC Project Engineer: Daniel L. Tauroney (OCTT) AC 315 330-2925	12. SPONSORING MILITARY ACTIVITY Rome Air Development Center (OCTT) Griffiss Air Force Base, New York 13440
---	---

13. ABSTRACT

An experimental and analytical study of a particular time-domain signature for radar space object identification is described. Measured data presented for several simple metallic shapes which demonstrate the direct relationships between the physical properties of a radar target and its time-domain signature are presented. Valid time-domain signature waveforms obtained by combining three-frequency low resonance scattering data and short pulse radar data are also presented. Finally, a new, approximate technique for producing a three dimensional target image from time-domain signature data at three look angles is described and illustrated with computer-drawn isometric views of simple shapes.

DD FORM 1 NOV 1968 1473

UNCLASSIFIED

Security Classification

**UNCLASSIFIED**

Security Class: UNCLASSIFIED

14. KEY WORDS	LINK A		LINK B		LINK C	
	ROLE	WT	ROLE	WT	ROLE	WT
Inverse scattering Radar signature Radar time-domain scattering Radar Electromagnetic scattering theory Short-pulse radar						

**UNCLASSIFIED**

Security Classification

SAC-Orifice AFB BY 15 JUL 71-90

MEASUREMENT AND ANALYSIS OF SPECTRAL SIGNATURES

ElectroScience Laboratory  
The Ohio State University

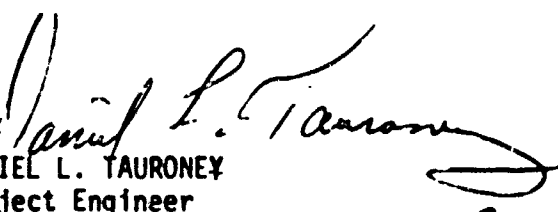
Approved for public release;  
distribution unlimited.

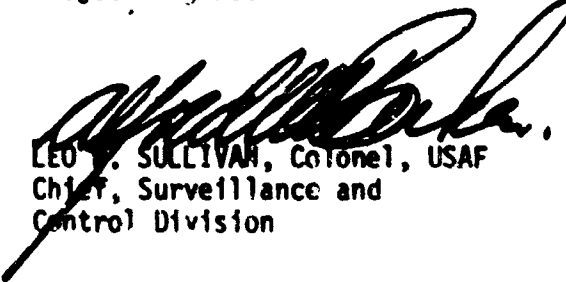
## FOREWORD

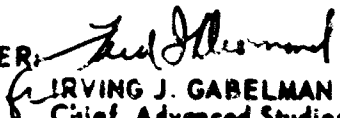
This report, OSURF 2784-2, was prepared by the ElectroScience Laboratory, Department of Electrical Engineering, The Ohio State University, Columbus, Ohio. Research was conducted for Rome Air Development Center, Griffiss Air Force Base, New York, under Contract F30602-69-C-0231, Job Order 45060000, Task 05. Daniel L. Tauroney (OCTT) was the RADC Project Engineer.

This report has been reviewed by the Information Office, OI, and is releasable to the National Technical Information Service.

This technical report has been reviewed and is approved.

Approved:   
DANIEL L. TAURONEY  
Project Engineer

Approved:   
LEO J. SULLIVAN, Colonel, USAF  
Chief, Surveillance and  
Control Division

FOR THE COMMANDER:   
IRVING J. GABELMAN  
Chief, Advanced Studies Group

## ABSTRACT

An experimental and analytical study of a particular time-domain signature for radar space object identification is described. Measured data presented for several simple metallic shapes, which demonstrate the direct relationships between the physical properties of a radar target and its time-domain signature are presented. Valid time-domain signature waveforms obtained by combining three-frequency low resonance scattering data and short pulse radar data are also presented. Finally, a new, approximate technique for producing a three-dimensional target image from time-domain signature data at three look angles is described and illustrated with computer-drawn isometric views of simple shapes.

## EVALUATION

This effort had significant results in developing a technique which gives a three-dimensional target image from a time domain signature. It emphasized the importance of low resonance region data to constrain the volume of the target and that the approach is adaptable to present-day radar technology. The short pulse plus three resonance region cw responses can be used to obtain the size and shape of satellite-type targets and has future use in the space object identification and classification area.

  
DANIEL L. TAURNEY  
Project Engineer

## TABLE OF CONTENTS

Chapter	page
I. INTRODUCTION	1
II. MEASURED DATA	2
III. COMBINATION OF SHORT-PULSE AND RESONANT REGION DATA	23
IV. RADAR IMAGING USING THE TIME-DOMAIN RESPONSE	51
V. CONCLUSIONS	76
REFERENCES	78
APPENDIX	80

## I. INTRODUCTION

The research conducted on this program is directed toward new and improved designs for space object identification radars. A new approach via discrete multiple-frequency samples of the target's echo signal in its low resonance range is studied. Such an approach is suggested by the known relationships between the ramp response waveform of an object, which can be produced synthetically from these data, and the physical properties of the object.<sup>1,2,3</sup>

The principal goals of the program are:

- 1) The design and instrumentation of a unique reflection measurement facility capable of rapidly and accurately sampling the echo signal of a target in amplitude and phase at 10 harmonic frequencies,  $f_o(f_o)10f_o$ , spanning the low resonance range of the target.
- 2) The development of new techniques for exploiting the direct relationships between the physical properties of a radar target and its ramp, step and impulse response waveforms in identification schemes.
- 3) To suggest and illustrate procedures whereby data from short pulse radars could be integrated with low resonance region data to further refine the identification capabilities of 2).

In this report, our progress toward these goals is described. Briefly, the measurement system in 1) has been constructed and is operational. Scattering data on several representative target shapes have been collected, and the accuracy and repeatability of these results established. Under item 2), techniques have been developed which produce isometric images of the objects using the ramp response waveforms for three mutually orthogonal views. These techniques also appear to be feasible using much more spatially restricted views of the object. Under item 3), procedures for producing step and impulse response waveforms of an object from a combination of low resonance range samples and short pulse data have been suggested and illustrated using actual radar data. Thus substantial progress toward the design of a space object identification radar has been made.

## II. MEASURED DATA

A series of ten-frequency complex spectral response measurements on representative targets were made during this project in order to further study the characteristics and utility of ramp response waveforms for radar signature work. The specific metallic targets, which are detailed in accompanying figures, are:

1. a 2:1 circular cylinder, Fig. 1.
2. A 2:1 circular cylinder with a spherical cap, Fig. 2.
3. A 2:1 circular cylinder with a conical cap; Fig. 3.
4. A 2:1 circular cylinder with a smaller 1:1 cylinder on one end, Fig. 4.
5. A cube, Fig. 5.
6. A 60° cone, Fig. 6.
7. A half-spheroid, Fig. 7.
8. A 3:1 sphere-capped cylinder with a side-mounted stub, Fig. 8.

A set of metallic spheres with diameters of 1/2", 3/4", 1", 1-1/4", 1-1/2", 1-3/4" and 2" were also measured and used as calibration references during this program.

The system used for these measurements was described in an earlier report.<sup>4</sup> In brief, it is a coherent c.w. radar cross-section measurement system operating at frequencies of 1.082, (1.082), 10.82 GHz. The use of slow target motion to produce an interference pattern permits simultaneous measurement of the complex scattered signal at several frequencies. At present, simultaneous measurements are performed within the frequency bands 1-2 GHz, 2-4 GHz, 4-7 GHz, and 7-11 GHz, with rapid sequencing of the different bands. The photograph in Fig. 9 shows the log-periodic-fed, 3 ft diameter dish antennas used for transmitting and receiving, and the target pedestal which has computer-controlled rotation and linear motion. Because separate transmit and receive antennas are used, scattering at a 20° bistatic angle is actually measured by this system. However, for the frequencies and target sizes used, the true backscatter is very nearly identical to the 20° bistatic response.

The experimental procedure presently used with this system provides calibration and accuracy checks on each target measurement run. Measurements of a no target case, and of at least two reference spheres accompany each target measurement run. Then the computer calibration sub-program subtracts the background data, normalizes the background-free data to produce exact complex cross-section values for the "reference sphere", and checks system accuracy and linearity by comparing calculated and measured cross-sectional data for the different-sized "check" sphere(s). A data run is accepted only if its check sphere results are accurate to within specifications presented in the Appendix.

Our experience has indicated at least two sources of the measured data variation. The disturbance of the field configuration by the styrofoam support seems to affect the X-band measurements. "Long-term" drift,

caused by repositioning of absorber panels, pedestals, etc. for other measurements being performed in our anechoic room, is the second factor. On a given day, repeatability of the measurements range typically from 3% in amplitude and  $30^\circ$  in phase at the higher frequencies to 1%,  $1^\circ$  at the lower frequencies, which is considerably better than the long-term repeatability obtained for a complete data set. It is clear that the dedication of an anechoic room solely to these measurements, and a redesign of the target pedestal to maintain the target positioning accuracy while creating less field disturbance in the target region would improve the accuracy of the present measurement system.

Complex spectral return data for the measured targets are presented in the Appendix, where the signal magnitude is the square-root of echo area, in centimeters, and the phase reference is the geometric center of the object. Scaling can be used to apply these data to other targets of identical shape but different size from those measured. For a target object  $N$  times as large as our measured object, the magnitudes are multiplied by  $N$  to yield data on the larger object for frequencies which are reduced by a factor of  $N$ . Thus, if the dimensions of the targets in Fig. 1-8 were in feet rather than centimeters, the square root of echo area would be given in feet rather than centimeters, at frequencies from 35.43 MHz to 354.3 MHz.

The ramp response is obtained from these complex spectral data using a 10-frequency Fourier cosine series, where each component is weighted by a factor  $-1/n^2$ ,  $n$  being the harmonic number. Multiplying the results by  $(\pi/4) \cdot (1.00/1.08)$  yields the normalized ramp response defined in Reference 3, whose amplitude is approximately  $\sim 1/\pi$  times the cross-sectional area, vs twice-times-distance along the target object. Some representative ramp response waveforms for various target objects are shown in Figs. 10 through 17. Specifically, the waveforms correspond to:

- Fig. 10; a 2:1 cylinder (Fig. 1) at endfire and broadside.
- Fig. 11; sphere capped cylinder (Fig. 2) at nose-on, broadside and tail-on.
- Fig. 12; cone-cylinder (Fig. 3) at nose-on, broadside, and tail-on.
- Fig. 13; step cylinder (Fig. 4) at nose-on, broadside, and tail-on.
- Fig. 14; cube (Fig. 5) at broadside and  $45^\circ$ .
- Fig. 15; cone (Fig. 6) at  $0^\circ$ .
- Fig. 16; half-spheroid (Fig. 7) at  $0^\circ$
- Fig. 17; large sphere-capped cylinder (Fig. 8) with stub  $\parallel$  and  $\perp$  to E-field,  $0^\circ$ .

Of course the ramp waveforms may also be scaled similarly to the spectral data. Multiplication of the distance scale by  $N$  and the amplitude by  $N^2$  yields the ramp waveform for a target  $N$  times larger than the measured sample.

The waveforms of Figs. 10 through 16 are assumed to be valid ramp response waveforms; i.e., the waveform for a single, nonperiodic ramp discontinuity would be virtually identical to the one presented using the illuminating ramp discontinuity with a period of 1.08 GHz. The large sphere-capped cylinder target model is too large for its waveforms to be valid, however. The response for this object has a duration which is longer than the period of the incident waveform. Thus, the response for successive illuminating pulses overlap and the resulting periodic waveform would change for a single illuminating ramp discontinuity. The waveforms of this object, shown in Fig. 17, definitely are characteristic of the object, and the orientation of the stub is indicated by the measured waveforms. However, the geometrical features of the valid ramp response do not hold in this instance.

The other target waveforms tend to confirm two major properties of the ramp response. First, the amplitude of the waveform is approximately  $-1/\pi$  times the target cross-sectional area vs distance along the line-of-sight. Second, the total area under the curve is proportional to the Rayleigh coefficient, and hence object volume.

Figure 18 shows a scatter diagram which demonstrates the correlation between actual target volume and the predicted volume obtained from the measured ramp response waveforms.

The area under a rigorous ramp-response waveform is obtained by simple integration. For our Fourier series plots, however, the D.C. level of the waveform is shifted so that the value of the integral is zero. Thus, the area under the ramp response is proportional to the D.C. offset of the waveform region just prior to the target response region. Multiplication of the D.C. offset in  $\text{cm}^2$  by the total period (27.7 cm), and by  $\pi$  results in the volume estimate of Fig. 18. It is seen that most points lie within the  $\pm 10\%$  contours, and that all except one group lie within the  $\pm 20\%$  contours. The group of points which depart greatly from actual volume are for the cylindrical objects, oriented broadside to the incident field, with their major axis parallel to the E-field (horizontal polarization). For vertical polarization, the volume prediction for this same target orientation is almost identical to the actual volume. It thus appears that the constant of proportionality between the area under the ramp response and the target volume is a function of the polarization of the interrogating field with respect to the body. However, if the incident E field is polarized perpendicular to the major axis, it appears that a proportionality constant of  $\pi$  gives good results for all targets measured. Furthermore, the ratio of maximum to minimum volume estimate seems approximately equal to the aspect ratio of the silhouette, as will be discussed later.

In Fig. 19, the ramp waveform is compared to  $-1/\pi$  times the actual target cross-sectional area for the 2:1 cylinder. Taking into consideration the risetime limitations of the ramp waveform, general agreement is seen.

The greatest difference in the two curves is seen in the shadow region of the object. The plot in Fig. 20, which compares cross sectional area and ramp response for the step-cylinder at  $180^\circ$  indicates that the step can be seen in the ramp response even though it is completely shadowed at this orientation. The plot of ramp response and actual cross section for the 2:1 cylinder perpendicular to the line-of-sight is shown in Fig. 21. Notice that the fit is much closer for  $\mathbf{E}$  perpendicular to the cylinder axis, and that the fit is not as good as for endfire for either  $\mathbf{E}$  field polarization. The amount of ringing following the main portion of the ramp response waveform seems to be indicative of its geometrical accuracy. It is noticed that the ringing is much more prominent for the broadside cylinder waveform of Fig. 21 than the endfire cylinder waveform of Fig. 19. Further studies should be made in this area in order to discover modifications of the waveform, based on the amount of ringing, to produce a more accurate cross-sectional area vs distance estimate.

Thus, our measurement series has produced interesting complex spectral data, lying in the Rayleigh and resonance range, for several target shapes of practical interest. Also, the ramp response waveforms obtained from the above data tend to confirm two properties of the ramp response derived from previous analysis and measurement of very simple metallic target shapes; that the waveform amplitude is proportional to target cross-sectional area, and that the total area under the waveform is proportional to target volume. In addition, some new general properties of the ramp response have been noticed in our results, which could provide a basis for further analytical investigation of its characteristics:

- 1) The area under the ramp waveform is polarization sensitive, and the ratio of its maximum to minimum value provides an estimate of the aspect ratio of the target silhouette.
- 2) If the  $\mathbf{E}$  field is oriented perpendicular to the major axis of the target silhouette, the proportionality constant between the body volume and total waveform area appears to be  $1/\pi$ .
- 3) The amount of ringing in the ramp response waveform is indicative of the correlation between the ramp response amplitude and the target cross sectional area vs distance (to the first zero crossing).

The system which produced these data constitutes a valuable experimental facility for our laboratory, and is still continuously in use. In fact, further improvements are being contemplated. A much larger and faster, time-shared instrumentation computer system is presently being acquired by our laboratory, and our system will be converted to utilize it as soon as it becomes available. Spectrum equalization and improved target mounting techniques are also being considered.



Fig. 1. 2:1 circular cylinder model 1.

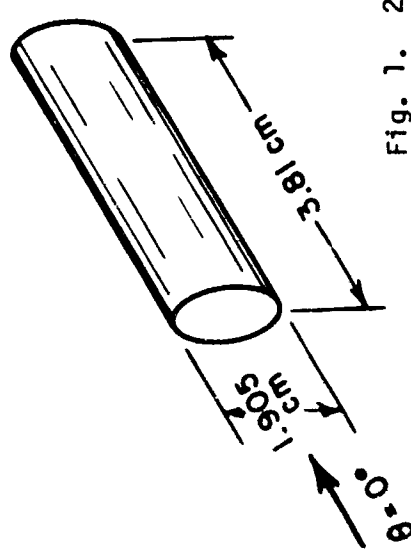


Fig. 2. Sphere-capped cylinder model 1.

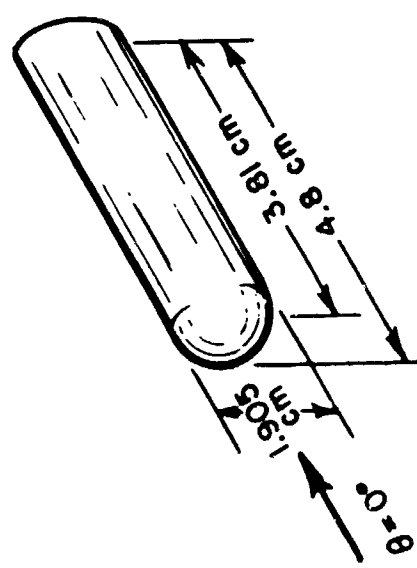




Fig. 3. Cone-cylinder model.

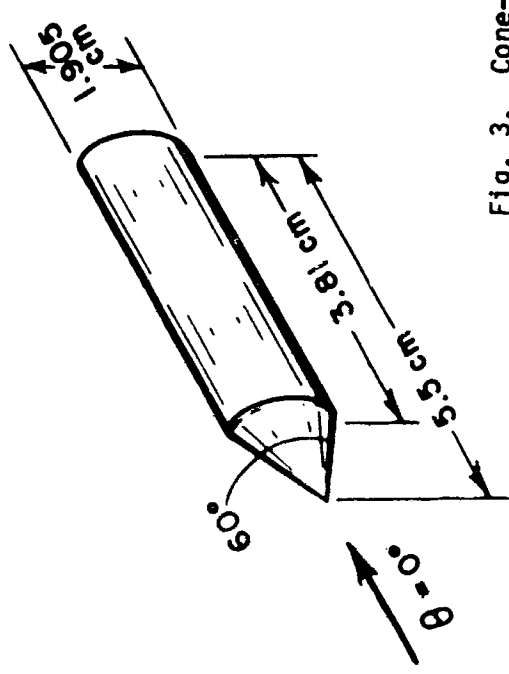


Fig. 4. Step-cylinder model.

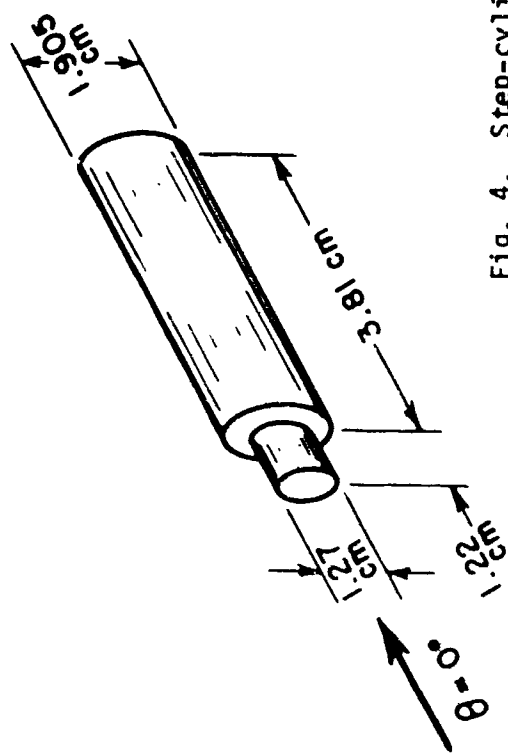




Fig. 5. Cube model.

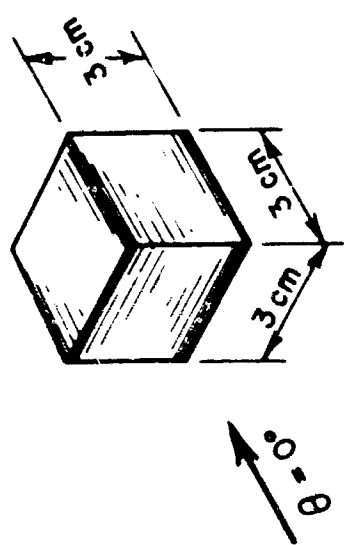


Fig. 6. Cone model.

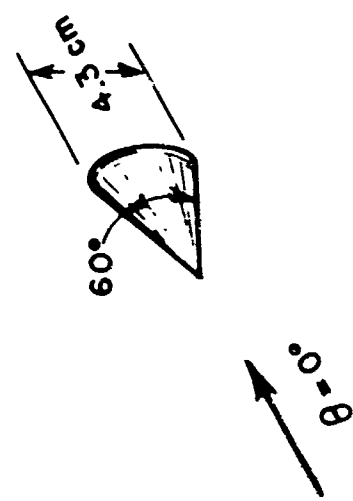




Fig. 7. Half-spheroid model.

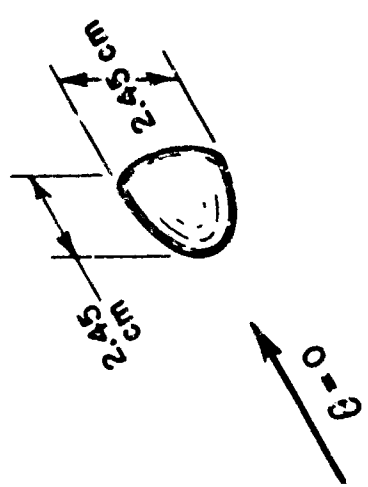
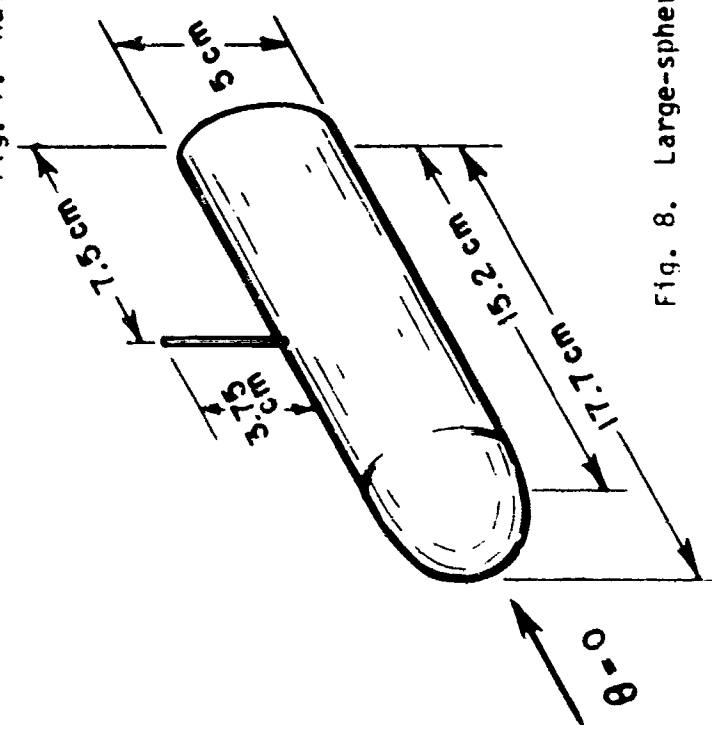


Fig. 8. Large-sphere-capped cylinder model.



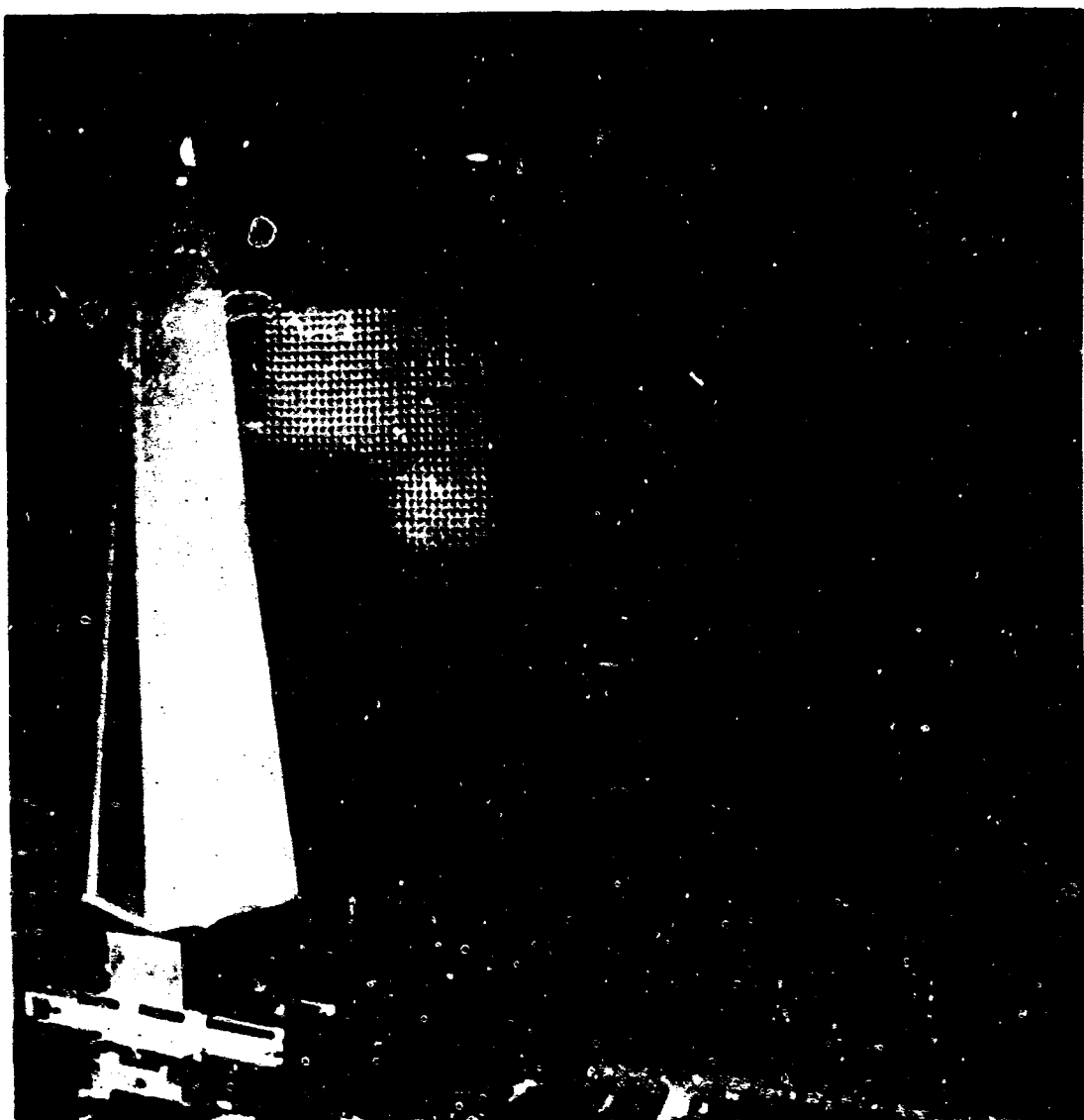


Fig. 9. Target pedestal and system antennas.

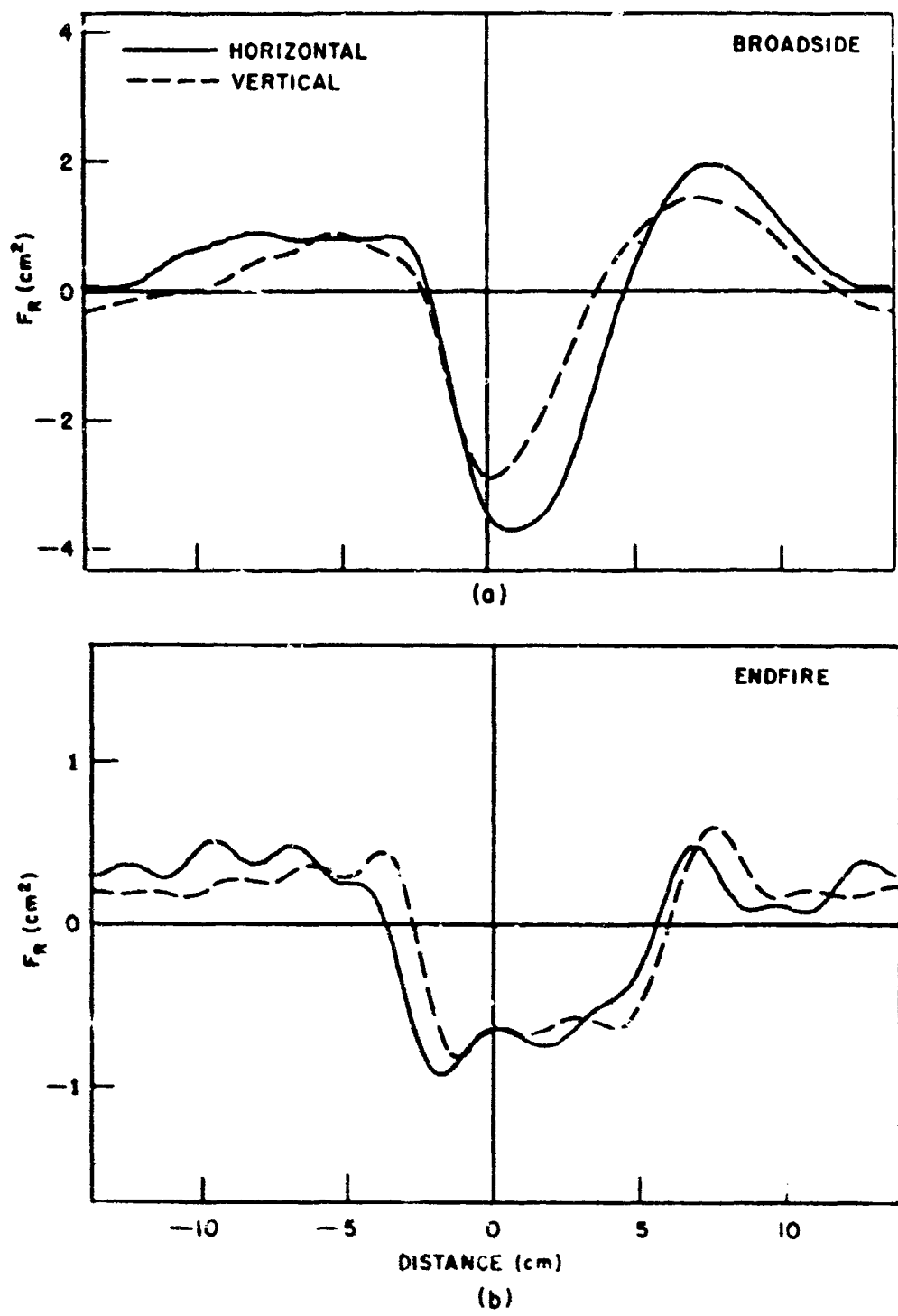


Fig. 10. Ramp response waveforms for 2:1 cylinder.

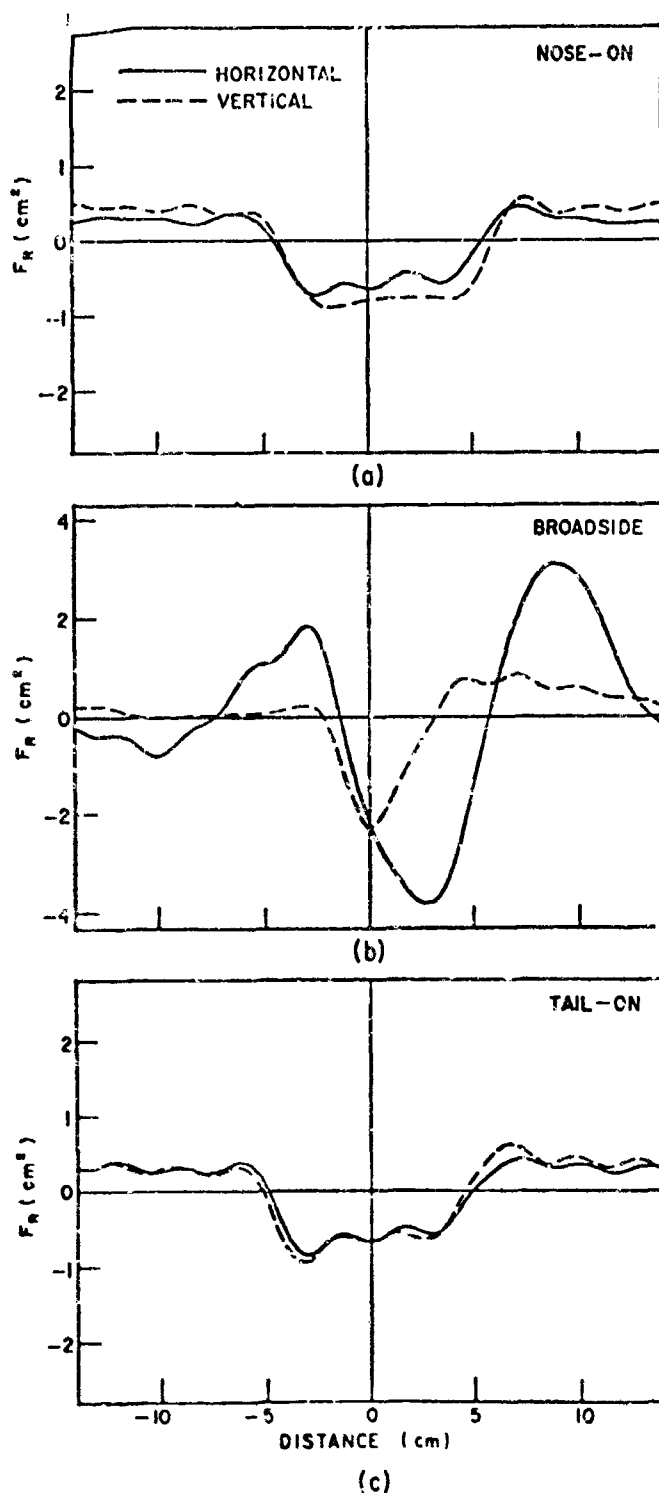


Fig. 11. Ramp response waveforms for sphere-capped cylinder.

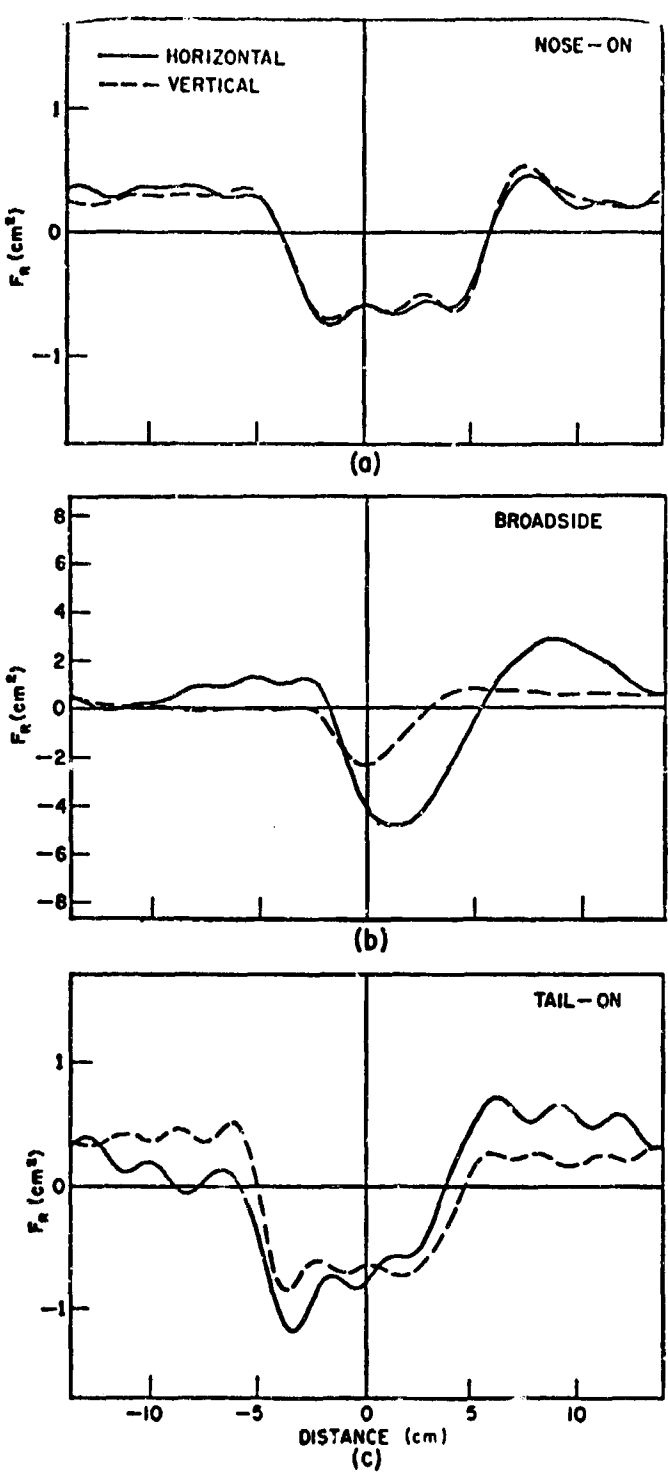


Fig. 12. Ramp response waveforms for cone-cylinder.

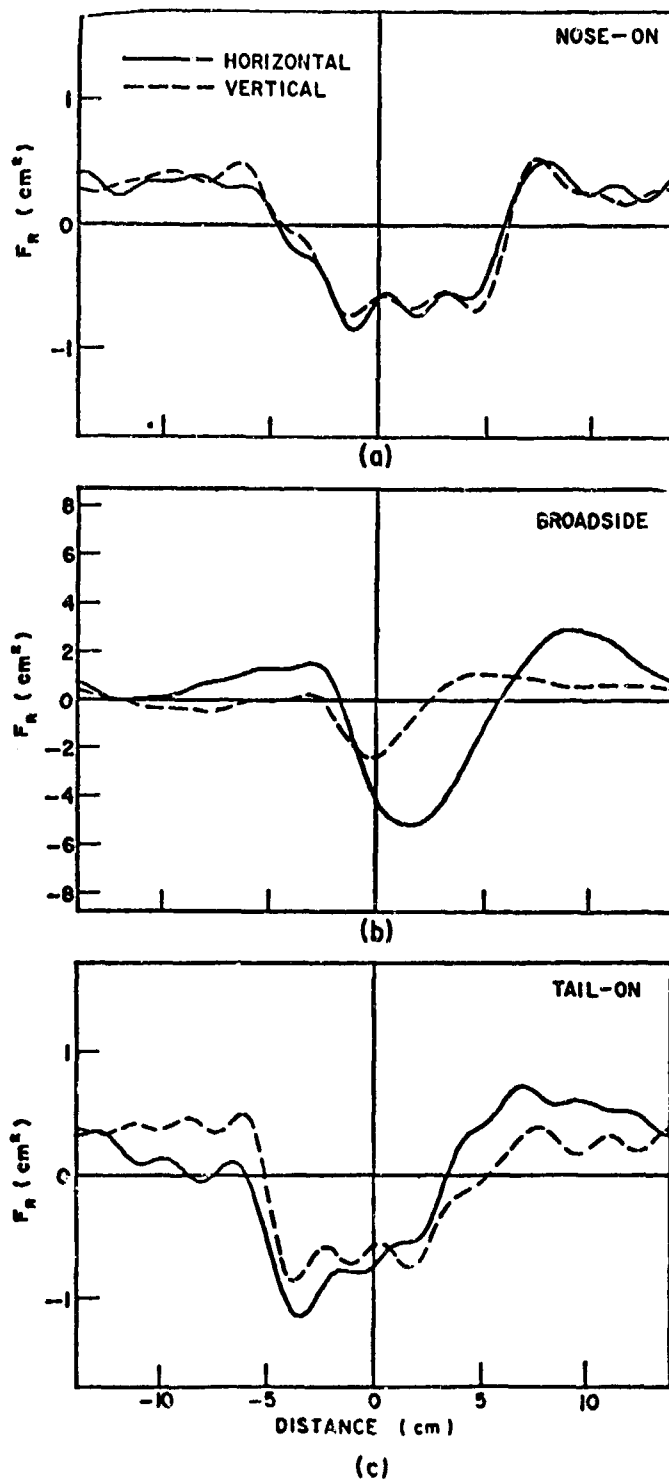
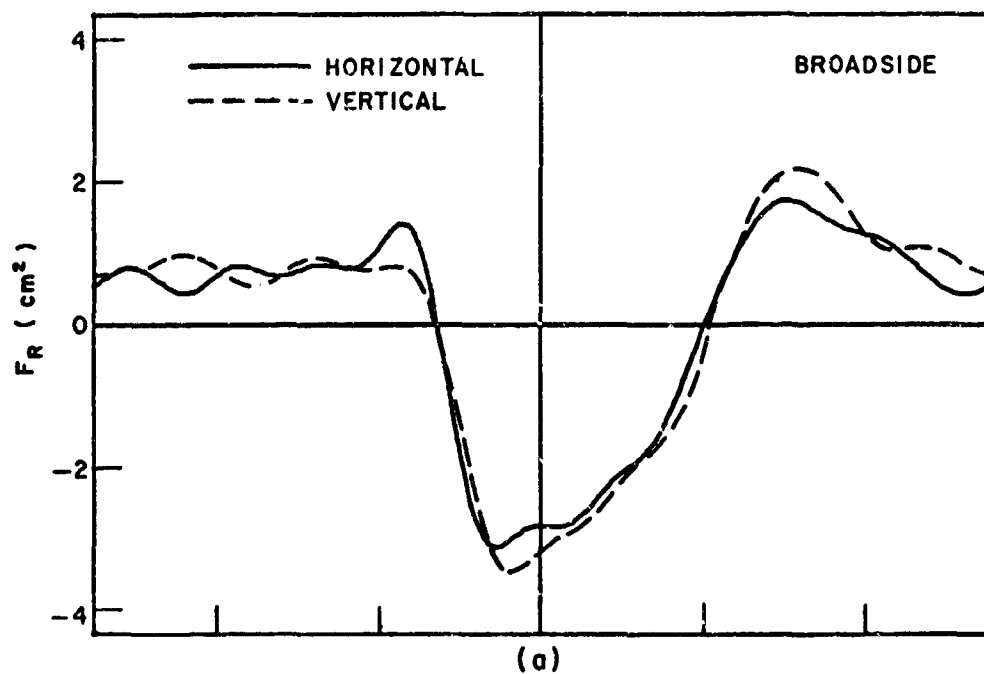
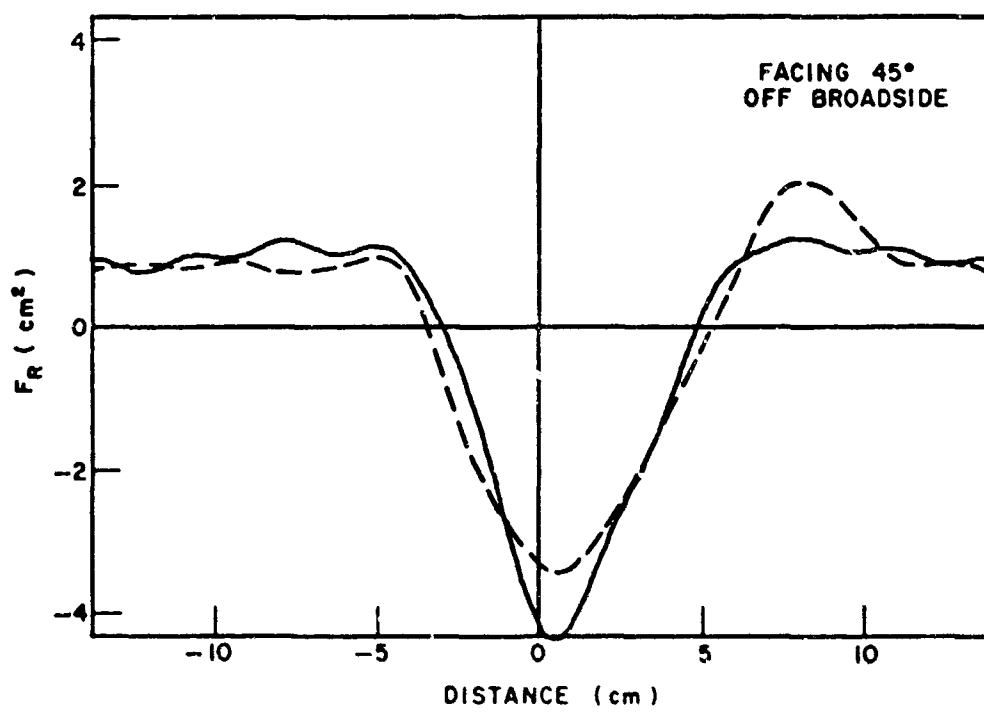


Fig. 13. Ramp response waveforms for step-cylinder.



(a)



(b)

Fig. 14. Ramp response waveforms for cube.

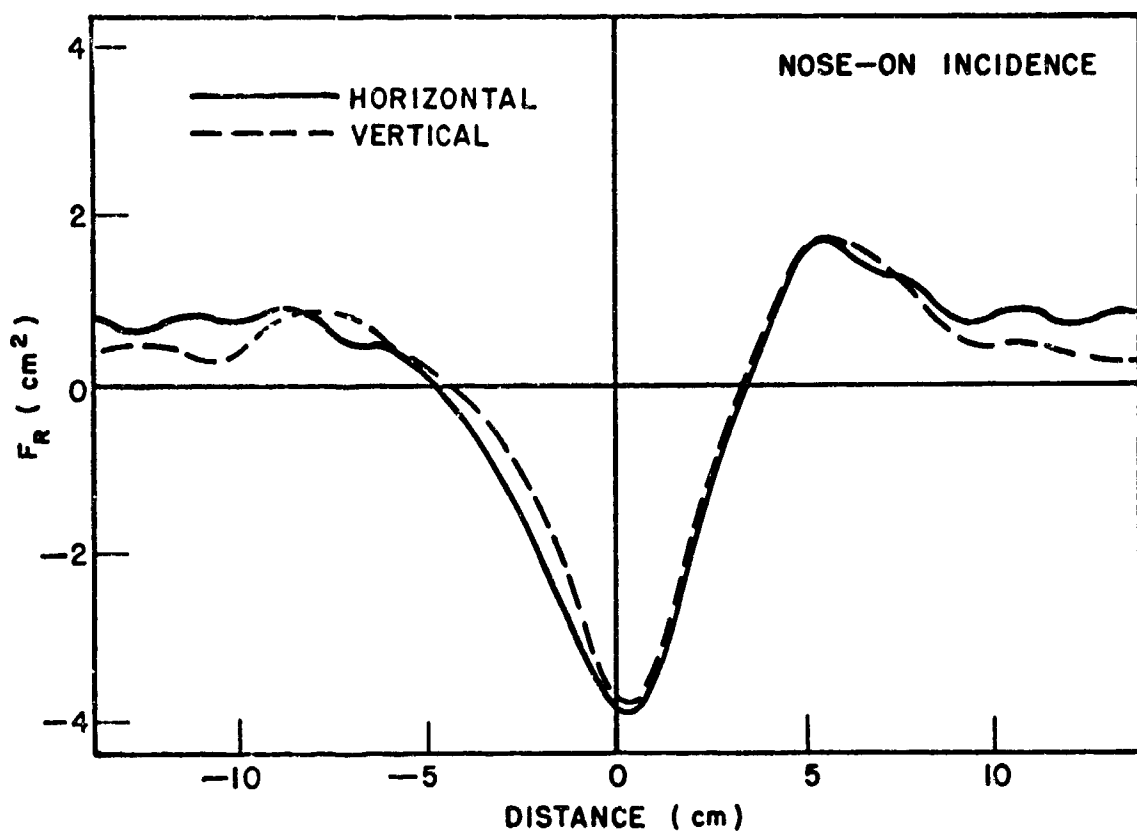


Fig. 15. Ramp response waveforms for cone.

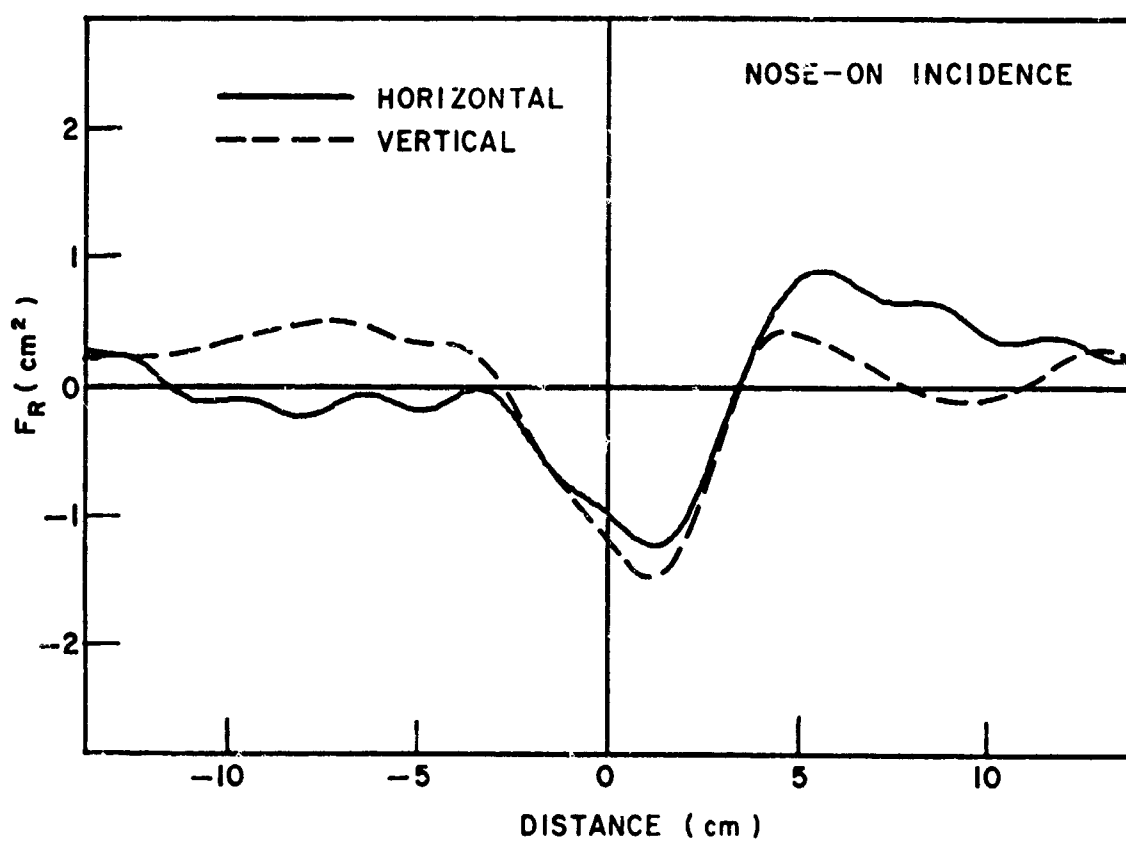


Fig. 16. Ramp response waveforms for half-spheroid.

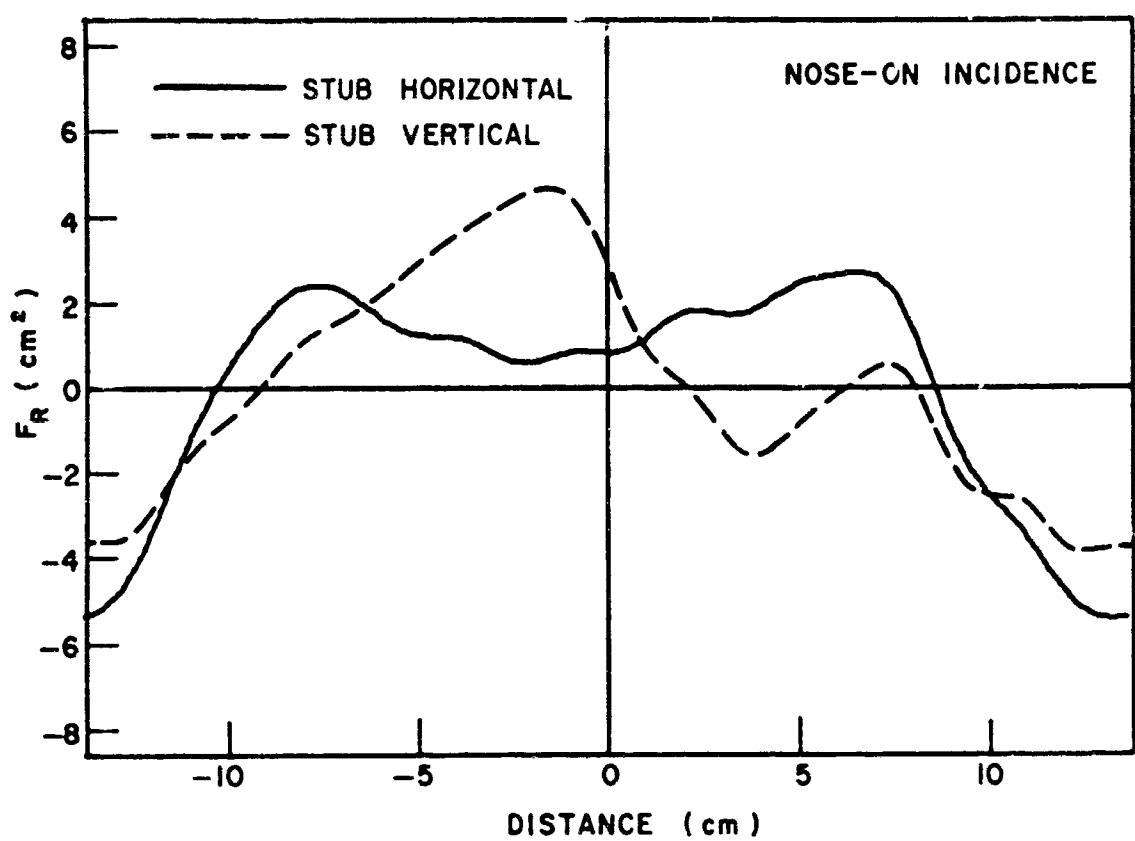


Fig. 17. Ramp response waveforms for large sphere-capped cylinder.

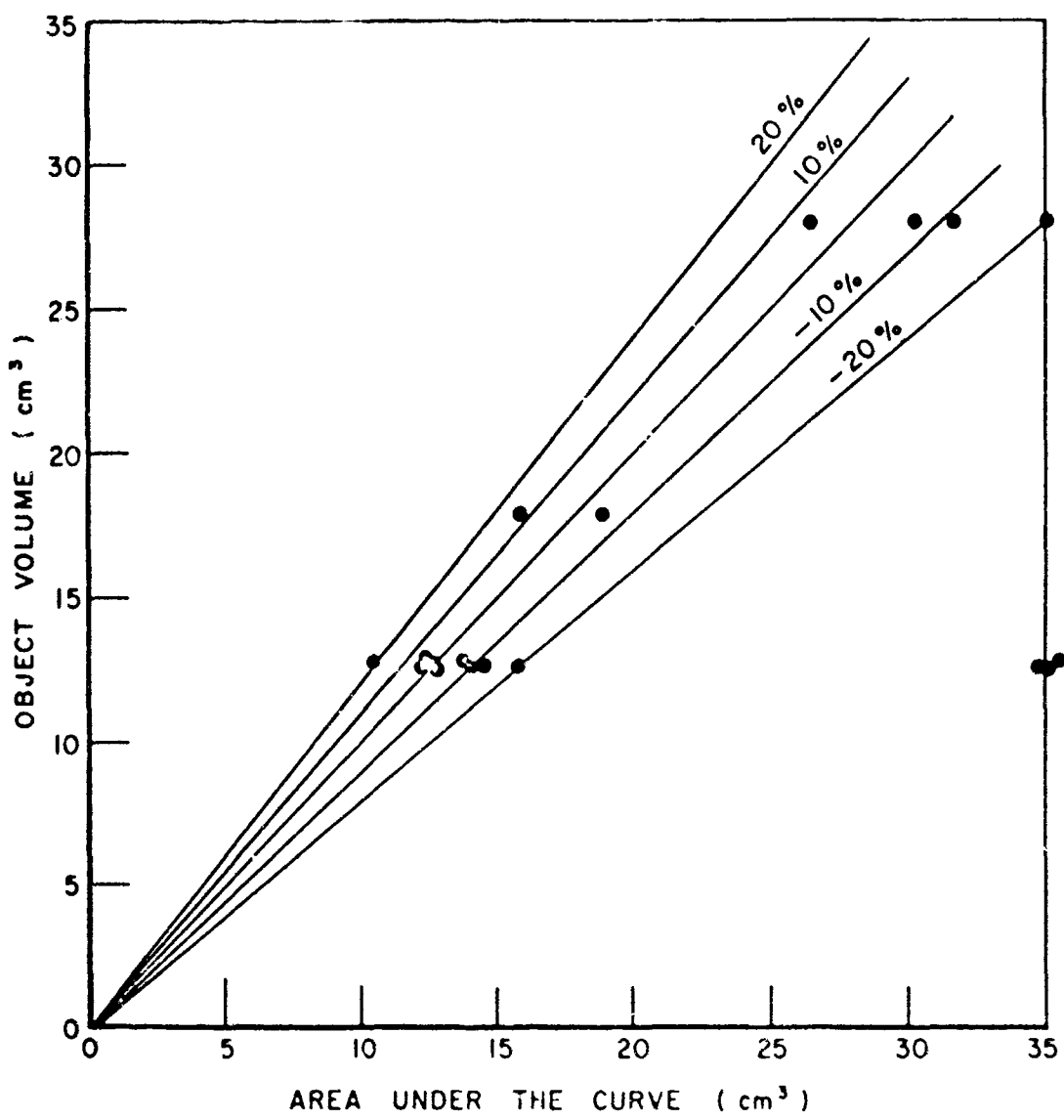


Fig. 18. Actual vs predicted object volume, using area under ramp response.

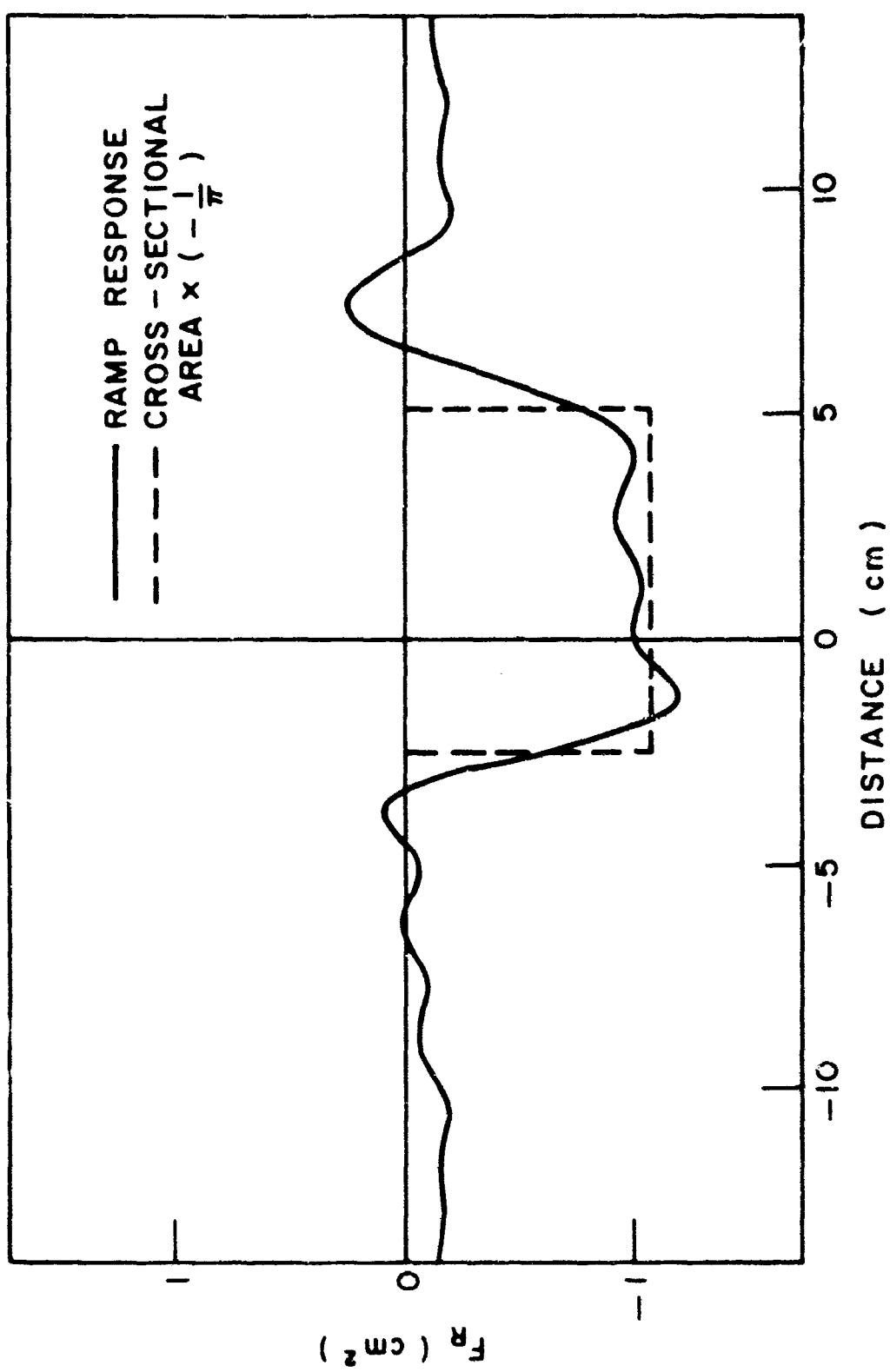


Fig. 19. Cross-sectional area times  $\left(-\frac{1}{\pi}\right)$  vs ramp response for step cylinder, endfire orientation.

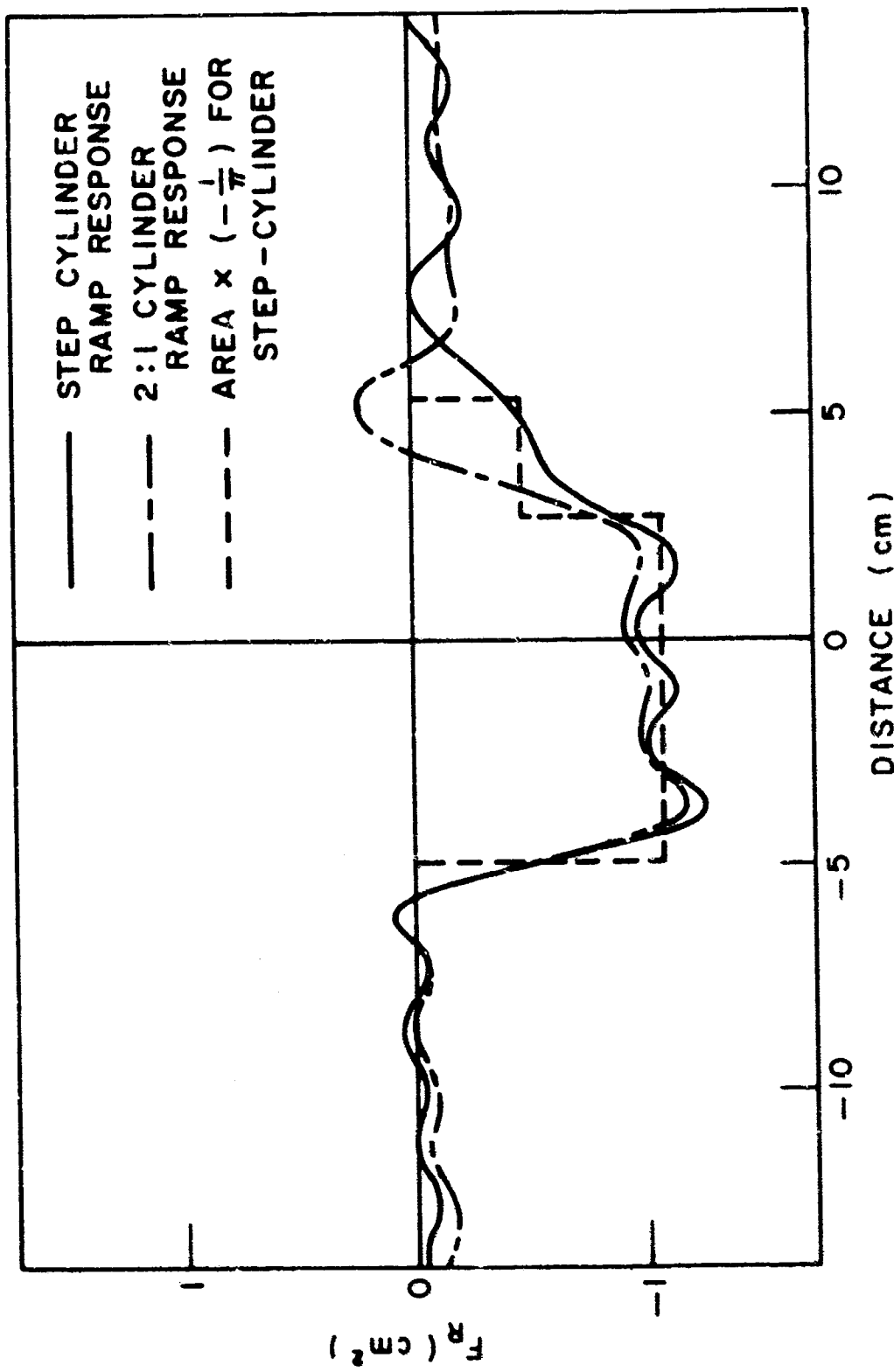


Fig. 20. Cross-sectional area times  $(-\frac{1}{n})$  vs ramp response for step-cylinder, backfire orientation (2:1 cylinder ramp included for reference).

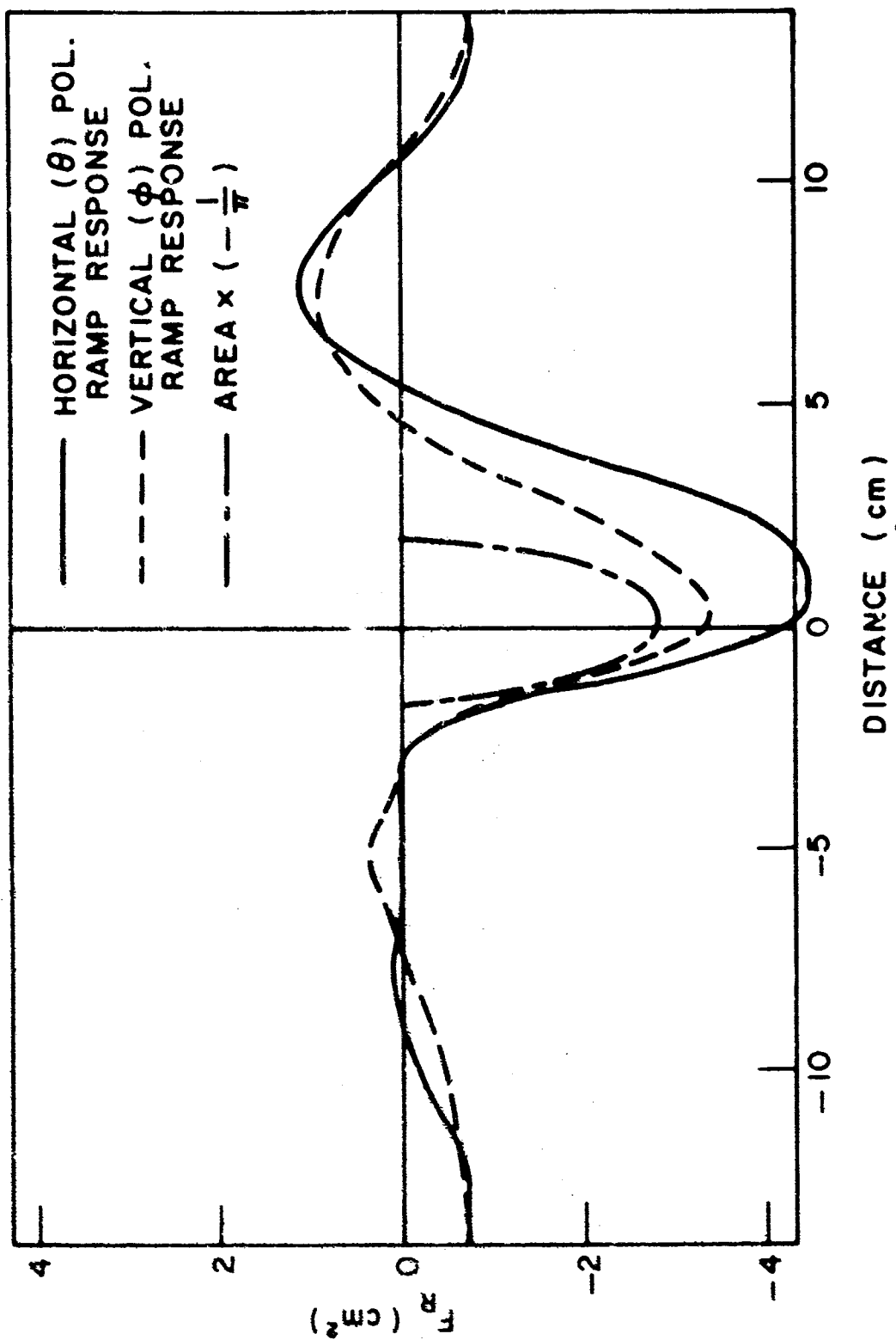


Fig. 21. Cross-sectional area times  $(-\frac{1}{t})$  vs ramp response for 2:1 cylinder, broadside orientation.

### III. COMBINATION OF SHORT-PULSE AND RESONANT REGION DATA

Short pulse radar systems are now a practical tool. One of the goals of this study is to demonstrate that scattered fields from a target obtained through the resonance region can be used to supplement the short pulse scattered field waveform to achieve target identification. The short pulse scattered field waveform is first used to isolate and classify various scattering centers on the target. The frequency spectrum of the short pulse must be sufficiently broad to achieve this result. The complete spectrum of the scattered fields of each scattering center can then be computed, once it is so classified. However, the dominant scattered fields of the target in the resonance region are associated with the gross features of the target instead of the detailed structure of the individual scattering centers. Thus if the complex scattered field spectrum generated by the scattering centers is supplemented by the spectrum of the scattered fields obtained in the resonance region, a more accurate very wide band scattered field spectrum can be generated. The likelihood of success of various target recognition schemes would be greatly enhanced by the availability of such data.

An important question to be discussed is the complexity of the system required to achieve the supplementary resonant frequency scattered field data. It will be seen that this can be accomplished with the addition of as few as three harmonically related radar frequencies operating in the appropriate frequency band.

The time domain response waveforms represent an important technique for the classification of radar targets and their subsequent identification. The ElectroScience Laboratory has generated a library of such waveforms where the incident field waveform is either periodic ramp, step or impulse functions. Various target signature techniques have been based on this data. This approach is to be used to combine the short pulse scattered field and the resonant scattered field data. The success of the technique is then judged by comparison with existing known scattered field waveforms.

The sphere, whose time response is rigorously known, is used to illustrate the characteristics of the short-pulse and the resonant-frequency data. The three canonic time-domain waveforms for a sphere are shown in Fig. 22. A computer program which constructs a Fourier Series approximation to these waveforms was used to examine the contributions made by different frequencies to the total waveform. Fifty harmonic terms are included in the canonic waveforms given in Fig. 23, where  $.1 \leq a/\lambda \leq 5$ . Comparison with Fig. 22 shows that except for the Gibb's phenomenon resulting from termination at 50 harmonics, these approximate waveforms are accurate. For a 1 meter diameter sphere, these waveforms would represent the result of measurement at 60 MHz, 120 MHz, ... 3 GHz through

the frequency band. The shape of the illuminating waveforms for such a wideband system are shown in Fig. 24. A short pulse system having a frequency bandwidth of 2.4 - 3.0 GHz can be simulated by using only harmonics 41-50 of the above waveform data. For the resulting illuminating waveforms shown in Fig. 25 a and b, the step and impulse responses are shown in Fig. 25 c and d. Because of the  $1/\omega^2$  weighting, the short pulse data makes essentially no contribution to the ramp response waveform for this smooth shape, and its response is not shown. For the step and impulse waveforms, the short pulse return occurs strongly only at discontinuities in the canonic waveforms - corresponding to the step or impulse terms at the specular point on the sphere. Since this specular point is the only scattering center for this shape, this result is expected. The creeping wave term which produces the cusp in the canonic impulse response is masked by the range sidelobes of the specular point response in the short pulse return data.

The resonant region data, obtained using harmonics 1-10, are shown in Fig. 26. Again, the normalization is consistent with Fig. 23. The relative accuracy of the ramp response waveform clearly illustrates why it is suggested as a significant signature. For the step and impulse responses, which are more indicative of shape details, the resonant region data is obviously less complete. As expected, the greatest error occurs at discontinuities of the canonic waveforms. If, in order to simplify the system, only five frequencies are used, the further degraded waveforms of Fig. 27 result.

Because the short pulse return occurs precisely where the low-frequency data is least accurate, these figures indicate that the two types of data can be profitably combined. It is also obvious from these figures, however, that simple addition of the returns does not result in an improved waveform approximation. For example, addition of low-frequency and short-pulse data for the sphere impulse response results in the waveforms of Fig. 28. On the other hand, if the character of the scattering center is identified, its complete spectral response can be generated and this combined with a greatly reduced quantity of resonant frequency data to achieve the desired result. A brief examination of short pulse return characteristics was made in order to utilize this data properly to construct much more accurate time domain waveforms.

The development of short pulse radar systems has resulted in the ability to resolve in range the scattering centers of a target. A further improvement would be the ability to classify the type of scattering center corresponding to the returned signal. Each type of scattering center exhibits a characteristic frequency dependence of the scattered field which can be expressed as  $F(\omega) \propto a_0(j\omega)$  or a linear combination of such terms. Table I gives the correspondence of several common scattering centers.

TABLE I

$\nu = 0$	Geometrical optics term from a doubly curved surface, <u>or</u> backscatter by a straight finite length edge.
$\nu = -\frac{1}{2}$	scattering due to doubly-diffracted edge scattered fields
$\nu = 1$	specular scattering by a flat plate
$\nu = -1$	tip scattering (e.g., a cone tip)

Of course more complicated dependence upon frequency exists such as the scattering caused by creeping waves, antennas, or cavities. The types cited above will suffice for this preliminary investigation.

The means of identifying these scattering centers is the Fourier transformation

$$(1) \quad f(t) = \int_{-\infty}^{\infty} (j\omega)^{\nu} e^{j\omega t} d\omega.$$

However, we are interested in identification using measured data over a bandwidth corresponding to the radar pulse, i.e.,

$$(2) \quad f(t) = \int_{\omega_0 - \omega'}^{\omega_0 + \omega'} (j\omega)^{\nu} e^{j\omega t} d\omega$$

where  $\omega_0$  is the center frequency and  $2\omega'$  is the bandwidth. An identification technique which utilizes the phase of the carrier with respect to the center of the pulse return envelope has been proposed to obtain the identification from this short pulse data. We can model such a system using the computer. We assume that we can sample the return signal at a number of discrete frequencies in the band. Further, we down-convert such that the band  $\omega - \omega'$  to  $\omega + \omega'$  corresponds to the range  $\omega = 0$  to  $\omega = 2\omega'$ . Using a periodic train of shifted cosine pulses with a baseline width of  $T/m$  units to sample, we now replace Eq. (2) by

$$(4) \quad f(t) = \sum_{n=1}^M \Lambda(n) (jn\omega_0)^{\nu} e^{jn\omega_0 t}, \quad 0 < t < T$$

where

$$T = 2\pi/\omega_0 \text{ and,}$$

$$\Lambda(n) = \frac{1}{T} \frac{\sin\left(\frac{n\pi}{m}\right)}{\left(\frac{n\pi}{m}\right)} \frac{m^2}{m^2 - n^2} .$$

The fundamental frequency  $\omega_0$  is chosen to be  $\omega_0 = 2\omega'/m$ . Utilizing this Fourier Inversion,<sup>5</sup> we can now examine the time response corresponding to the types of scattering centers.

A computer program was prepared for the ElectroScience Laboratory Minimal Informer and responses for the various scattering centers were calculated for a band limited signal of 3.0 to 3.5 GHz. Samples were taken at 0.01 GHz intervals. This sampling interval yields accuracy to 3 significant figures in the resulting time response. The results are shown in Fig. 29. These time domain waveforms present the down-converted signal, where the local oscillator signal is synchronized with the envelope of the original return. The "real" waveform corresponds to a L.O. which is in phase with the envelope peak, whereas a L.O. signal in quadrature to the envelope peak results in the "Imaginary" waveform. Note that each center has a characteristic response, which differs from the response of the other types of scattering center. Figure 29 is plotted to relative scales as the shape of the response was of most interest in this preliminary study. These waveforms demonstrate that the down-conversion process preserves the shape of the pulse return envelope, but the down-converted waveform has only one carrier cycle beneath the envelope. Thus, if the down-conversion process is properly synchronized to the center of the envelope, the phase relationship between the carrier and envelope center is preserved, and is much more easily identified in the down-converted result. The relative amplitudes of the "real" and "imaginary" down-converted waveforms yield phase values for the carrier at the center of the envelope for the various scattering center types as given in Table II.

TABLE II

Relative Phase

$\gamma = 0$	$0^\circ$
$\gamma = -\frac{1}{2}$	$-45^\circ$
$\gamma = 1$	$+90^\circ$
$\gamma = -1$	$-90^\circ$
$\gamma = \frac{1}{2}$	$+45^\circ$

Another geometry of interest exists when two scattering centers of the same or different types occur at different ranges. For example let

$$F(j\omega) = (j\omega)^0 + (ju)^0 e^{-2jkR}$$

where the origin is taken at the first center and the range distance between the center is R. The real part of the down-converted waveform for such

a combination is shown in Fig. 30 for various values of  $R$ . The expected result is obtained. That is if the scattering centers are not resolved by the incident pulse, they coalesce into a single pulse and cannot be readily identified. Also of interest is the case where we have two scattering centers which differ, such as

$$F(j\omega) = (j\omega)^0 + A(j\omega)^{-1} e^{-j2kR}.$$

A result for this case is shown in Figs. 31 where  $A = 300$  for normalization. In this case the nature of the second  $(j\omega)^{-1}$  scattering center is obscured by the range dependence. However it may prove possible to remove this ambiguity by knowing the range difference  $R$  and using the computer software to interrogate each scattering center in turn.

It thus appears possible to process short-pulse radar information utilizing the carrier-envelope relationship to identify the nature of simple scattering centers. A further investigation into envelope-center synchronizing techniques, system accuracy obtainable, and identification of more complex scattering centers seems advisable for a more thorough understanding of the use of these waveforms for scattering center identification.

Use of the short pulse response to identify as well as locate the scattering centers permits it to be used to estimate the time-domain waveforms and finally to be combined with lower or resonant frequency data for a greatly improved response waveform. Again using the sphere for illustrative purposes, the short pulse response has been used to identify the specular scattering point. The short-pulse derived response waveforms for the specular point only for incident impulse and step waveforms are shown in Fig. 32.

The two types of data can now be combined by using the low frequency approximate waveform for harmonics 1-10 and the derived short pulse approximate waveform for harmonics 11-50 of the composite response waveform. The resulting approximate waveforms are shown in Fig. 33.

The figures show that the combined data waveforms are significantly improved over both the resonant region data and short pulse data waveforms of Figs. 26 and 32. In fact, the step response approximation differs from the true response by less than 1%. The impulse response approximation also shows excellent agreement with the true impulse, with a very slight error in the region of the creeping wave return. The ramp waveform is indistinguishable from the true response except for a shift in the D.C. level. A set of combined response waveforms using the 1st through 5th resonant region harmonics plus short pulse data are shown in Fig. 34. Step and ramp response waveforms for a sphere using the first 3 harmonics plus short pulse data are shown in Fig. 35. It is seen that the addition of just a few resonant region frequencies to the short pulse data yields time domain response waveform approximations which have all the correct features, and are in very good agreement with the rigorous waveforms.

Some combined waveforms using experimental data are presented next. The response waveforms of a conducting cube oriented so that its vertical faces are at 45° angles to the line-of-sight have been generated for horizontal and vertical incident polarizations, utilizing short pulse data from Reference 6.

The envelope amplitude vs distance waveforms used in our study are shown in Fig. 46 of Reference 6. In the absence of phase data, the scattered fields from the scattering centers was postulated as is predicted by scattering theory. In general, the phase information presented in Reference 6 is not directly applicable to our scattering center identification technique because it is not referenced to the envelope center as our method requires. However, the good agreement between expected and measured phase behavior when delay is taken into account,<sup>7</sup> indicates that the basic information is available for identification. An extended computerized data manipulation of these data in order to further study identification and canonic waveform approximation is recommended in the future.

In order to combine resonant region and short pulse data, the short pulse returns were converted to cm, using the thin wire reference target for normalization. Then our ten-frequency data were scaled by a factor of 10.25 to represent a 30.8 cm cube (corresponding to the short pulse data). The equivalent measurement frequencies, after this scaling, are 106 MHz, 212 MHz, ... 1060 MHz. The resulting short pulse derived waveform approximations are shown in Fig. 36. The ten frequency resonant region approximations are shown in Fig. 37. The combined approximate waveforms, using ten harmonics plus short pulse data, are shown in Fig. 38. The waveforms using five harmonics plus short pulse data are shown in Fig. 39. Finally, approximate waveforms using three harmonics plus short pulse data are shown in Fig. 40.

Unlike the sphere, rigorous canonic waveforms have not been calculated for the cube with 45° orientation. However, the general features of these approximations merit discussion, since they seem indicative of the accuracy which has been obtained.

Considering first the ramp response waveforms, it is noted that both polarizations produce similar waveforms which are approximately triangular, as the target cross-section vs line-of-sight would predict. It is seen again that the resonant region harmonics primarily affect these waveforms with short pulse data sharpening some of the corners.

The step response waveforms are quite distinct for the orthogonal polarizations. It is noted that the steps in the short pulse approximation and those of the ten harmonic approximation occur at approximately the same times. Thus, some agreement between the two types of data is evident. In the rear portion of the step response waveforms, the resonant region data add considerably to the waveform shape. It is possible that this contribution is caused by multiply diffracted waves which are masked by the short pulse data. As for the sphere, it is seen that the addition

of just three resonant region harmonics to the short pulse data results in a waveform which is hardly changed by the addition of more data except in the creeping wave region.

A study of the permissible range of target sizes for valid waveforms using just three harmonics has also been made. The shape of the responses for an incident step waveform for spheres such that  $.03^2 \leq a/\lambda \leq .2$  at the fundamental frequency are shown in Fig. 41. It is seen that for  $a/\lambda = .033, .067, .1, \dots$  the waveform leading step no longer starts at zero, making it difficult to deduce the starting point of the response waveform. Thus  $a/\lambda \approx .05$  at the fundamental seems to be the lower limit on target size for valid step waveforms using three harmonics. For  $a/\lambda \approx .2, .4, .6$ , the duration of the target response is considerably longer than the fundamental period, and overlap of succeeding response waveforms changes the shape of the main response region noticeably. Thus it appears that the combined step waveform using three low harmonics is valid for  $.1 < d/\lambda_f < .3$ , where  $d$  is the maximum object dimension and  $\lambda_f$  is the fundamental wavelength. This conclusion is based on the response waveforms for a sphere, and should be further investigated for objects of quite different shape.

It is seen that the impulse waveforms are the most closely related to the short pulse data, and that the amplitude of the resonant region contributions is small compared to the impulsive portions of the waveform. Thus, a greater dynamic range is necessary to accurately reproduce all impulse response characteristics. It is also noted that reducing the number of harmonics for combination with the short pulse data has more effect on the impulse waveform shape than for the other waveforms. The impulse response waveforms for both sphere and cube are greatly affected by the termination of their Fourier series approximations after 50 terms, which gives rise to the noticeable ringing around the impulsive waveform portions. A revised computer program, with a tapered frequency spectrum should produce waveforms of comparable detail which do not include as much ringing. Since all high harmonic terms are specified once the scattering center is identified such a modification would not require any change in the short pulse measurement technique.

Some general conclusions on combining short pulse and low frequency data can be made on the basis of the above waveforms. First, it is evident that the step is the best response waveform for combining the two types of data. Both types of data make significant contributions to its shape. It is more indicative of shape detail and polarization properties than the ramp response, and it is more representative of gross target features and requires less dynamic range than the impulse response.

Valid step waveform approximations appear to be possible using short pulse data plus three resonant region harmonics, provided the target maximum dimension lies between  $1/10$  and  $3/10$  of the fundamental wavelength. Thus, as an example, it would appear possible to construct valid step waveforms for targets between  $3'$  and  $10'$  in maximum dimension using low frequencies of 30, 60, and 90 MHz along with short pulse data.

One major problem in using HF frequencies for satellite identification involves propagation through the ionosphere. For most of the next decade, however, the critical frequency pertaining to continuous (day and night) ionospheric propagation will be below approximately 10 MHz for propagation in the direction of the zenith. Thus, it appears that a system with a 30 MHz fundamental frequency should be dependably usable for angles less than 60° from the zenith.

Another problem involved with HF frequency radar applications is the antenna requirement. However, recent development of a new type of compact wide-band HF antenna<sup>8</sup> seems to have alleviated this concern.

It seems, therefore, that the addition of low resonance-region frequencies to short-pulse data to produce greatly improved time domain response waveforms is feasible for satellite-size targets.

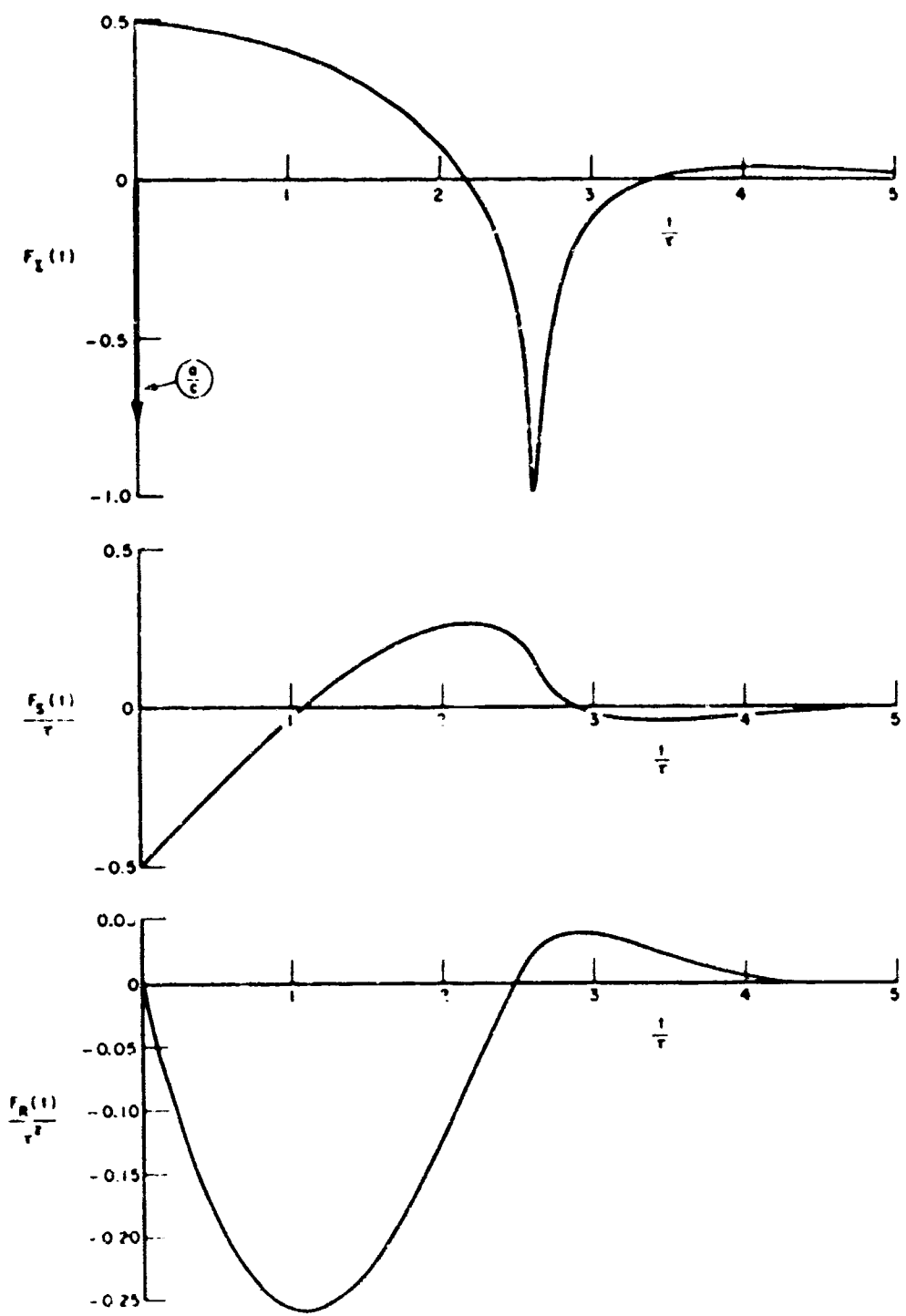


Fig. 22. Rigorous sphere time-domain response waveforms.

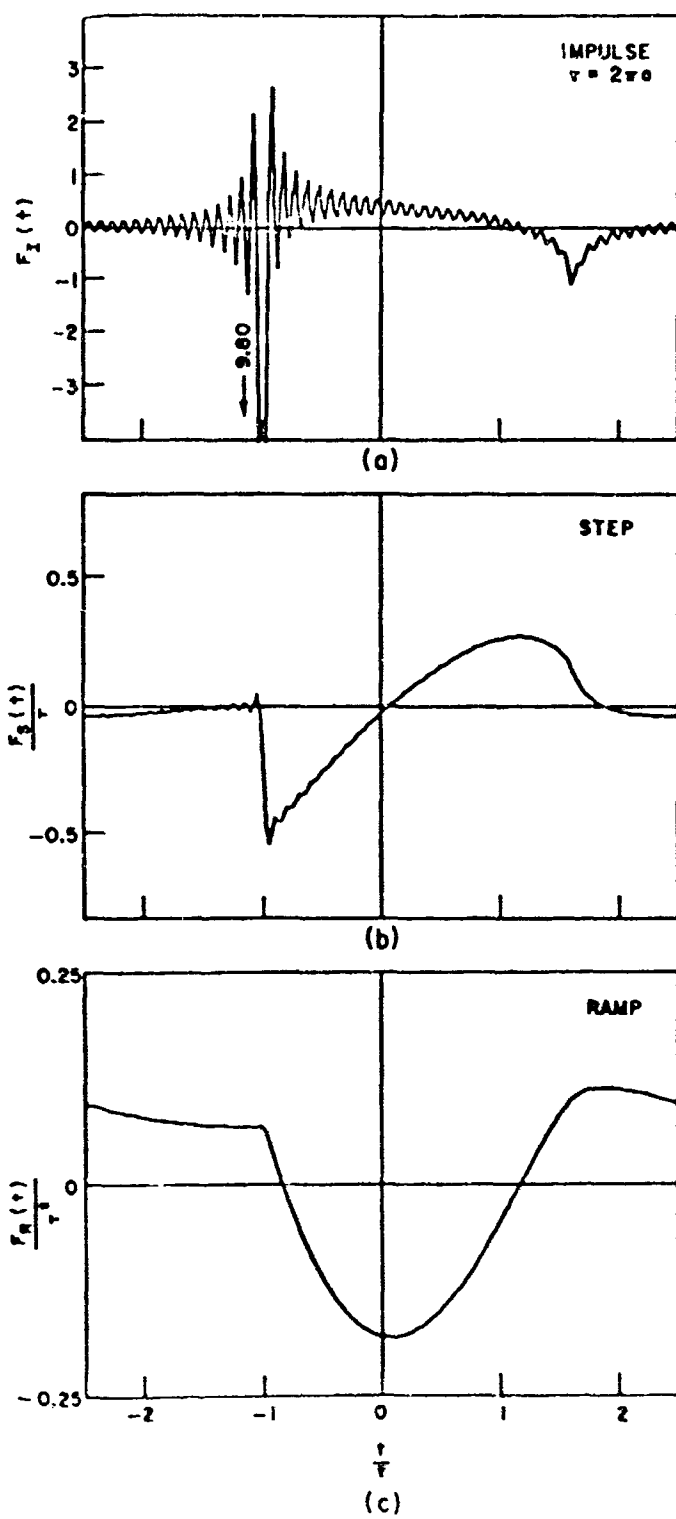


Fig. 23. Fifty-harmonic approximate sphere response waveforms.

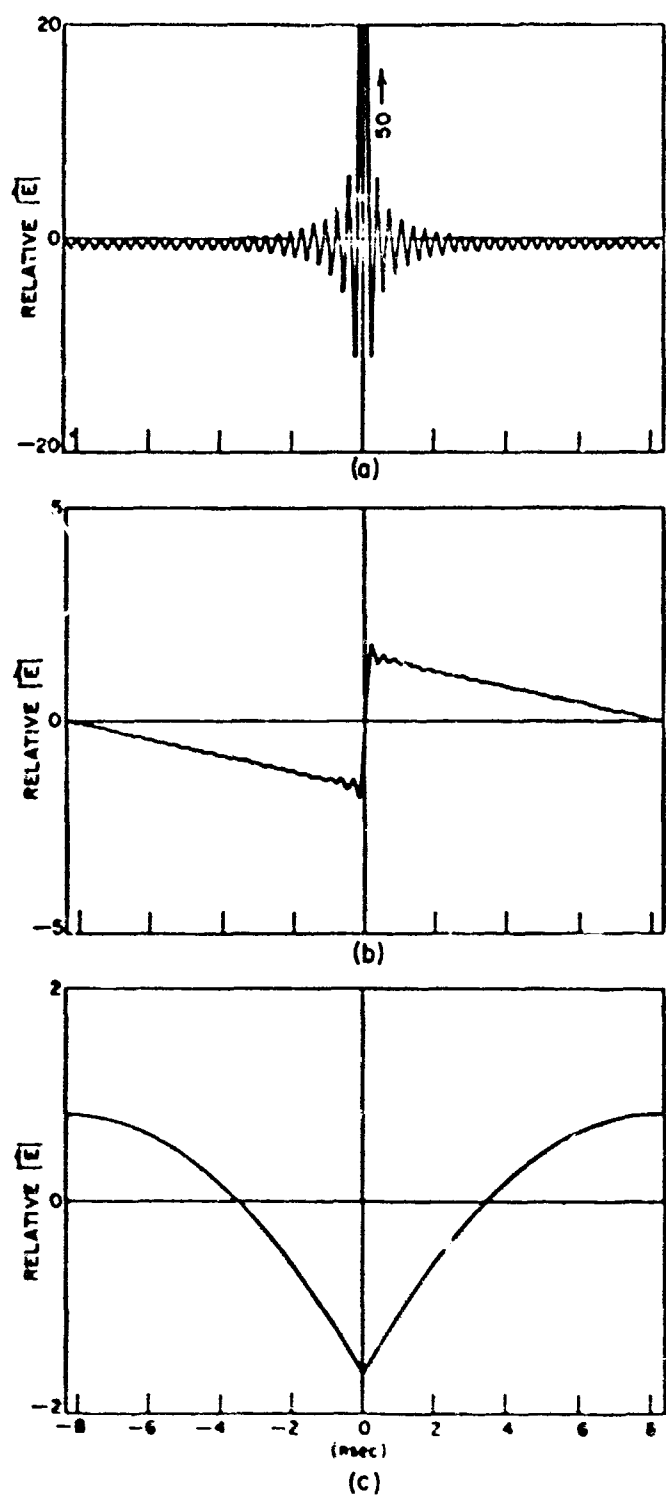


Fig. 24. Fifty-harmonic approximate excitation waveforms.

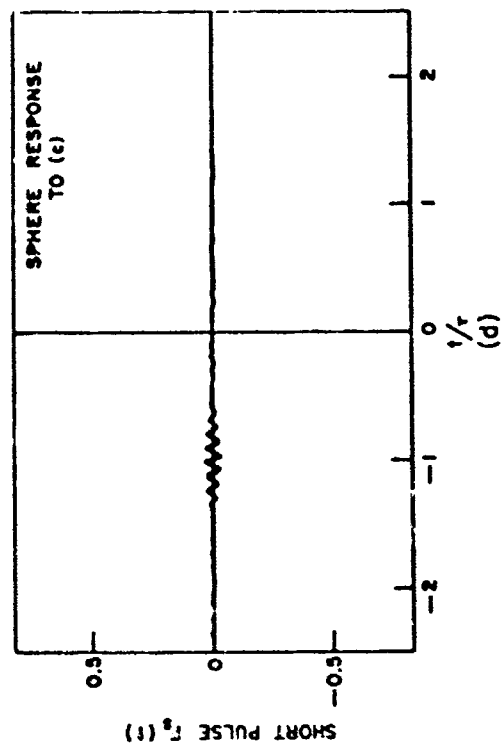
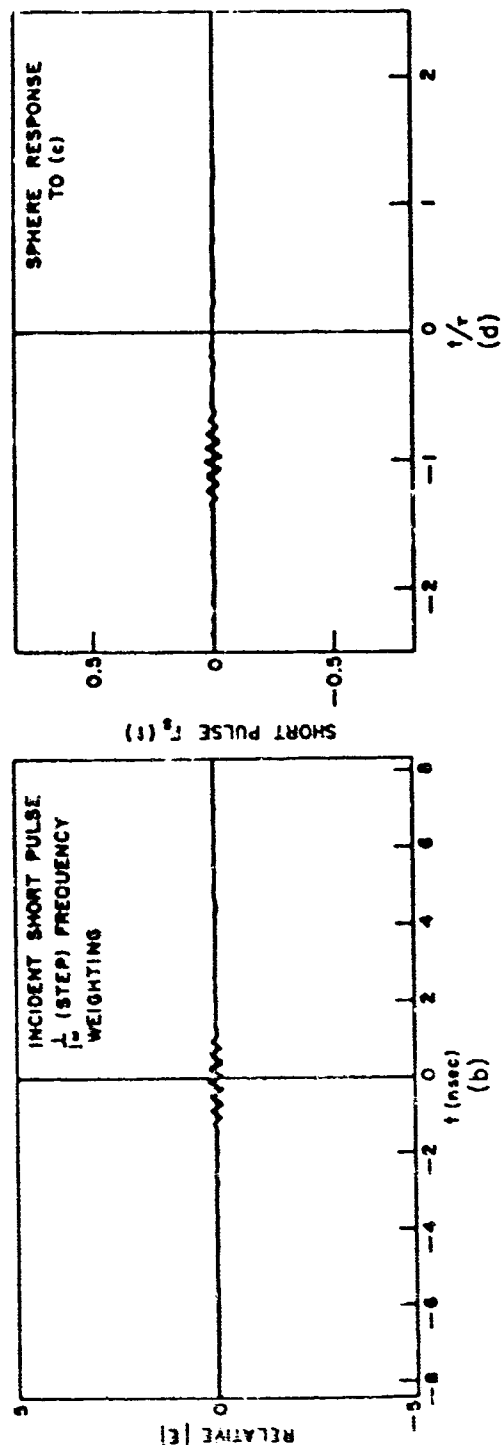
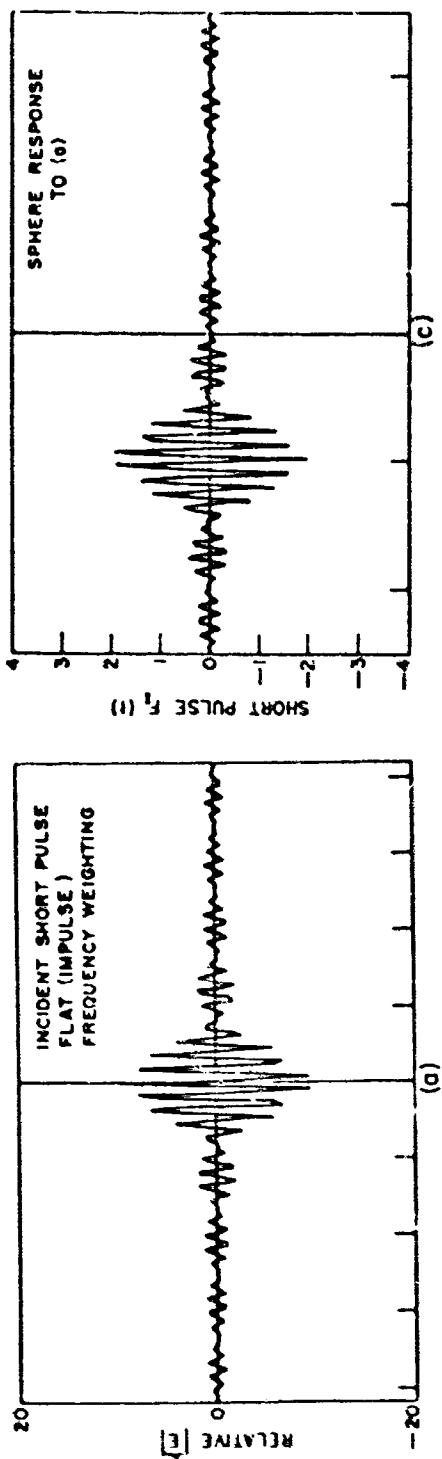


Fig. 25. Simulates short-pulse incident and sphere response waveforms.

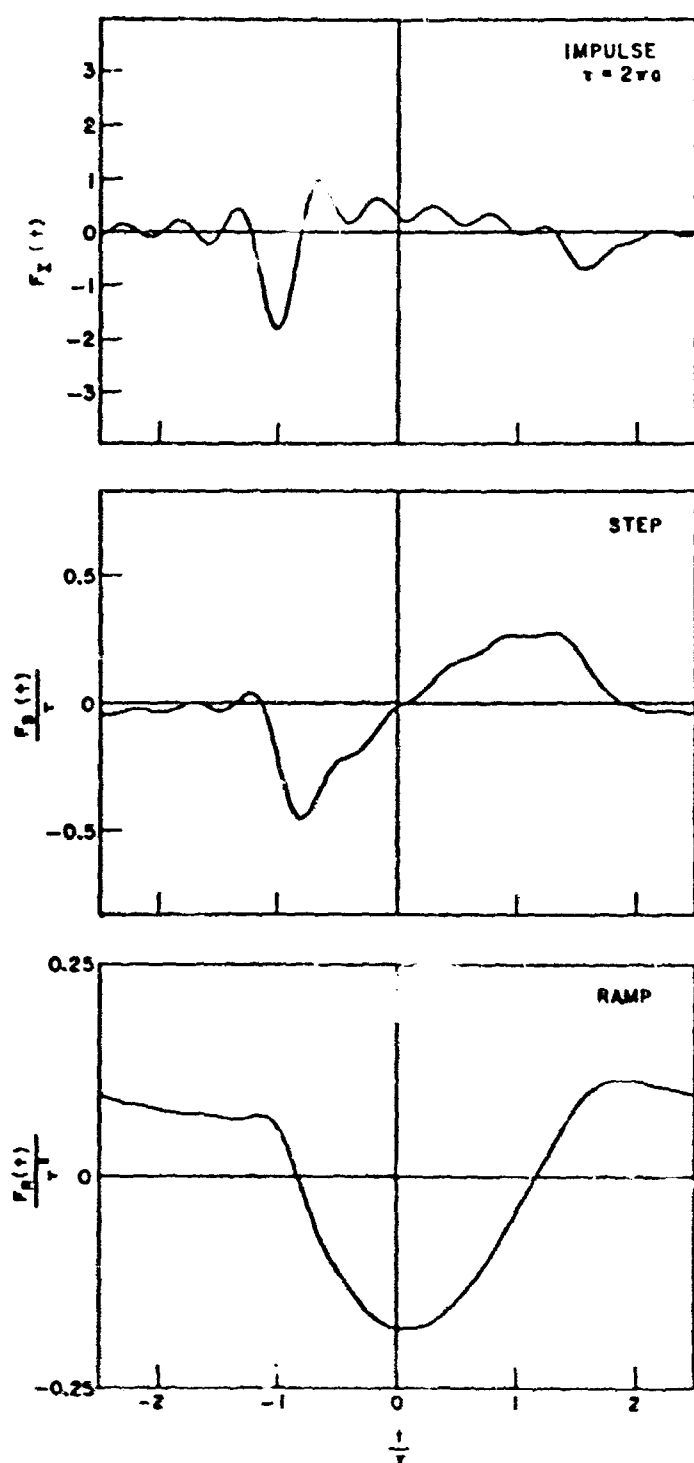


Fig. 26. Ten-harmonic approximate sphere response waveforms.

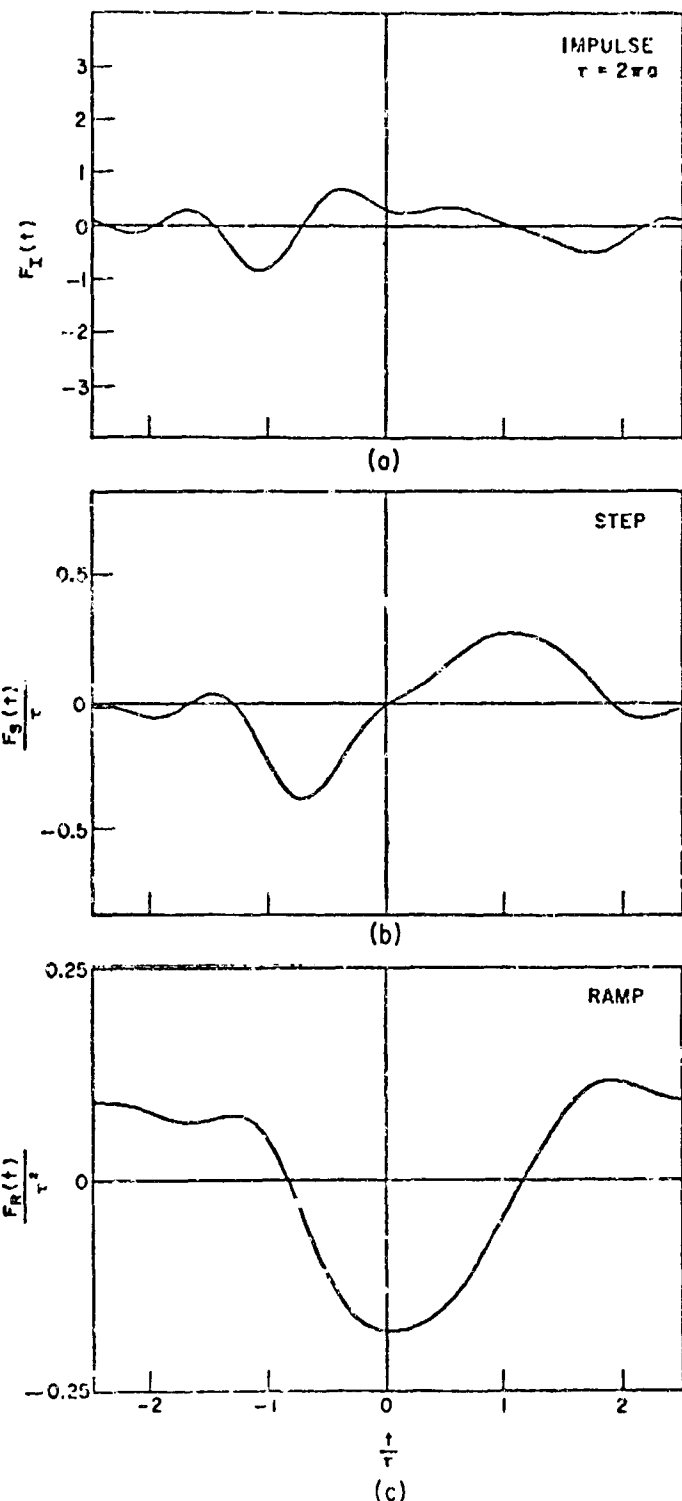


Fig. 27. Five-harmonic approximate sphere response waveforms.

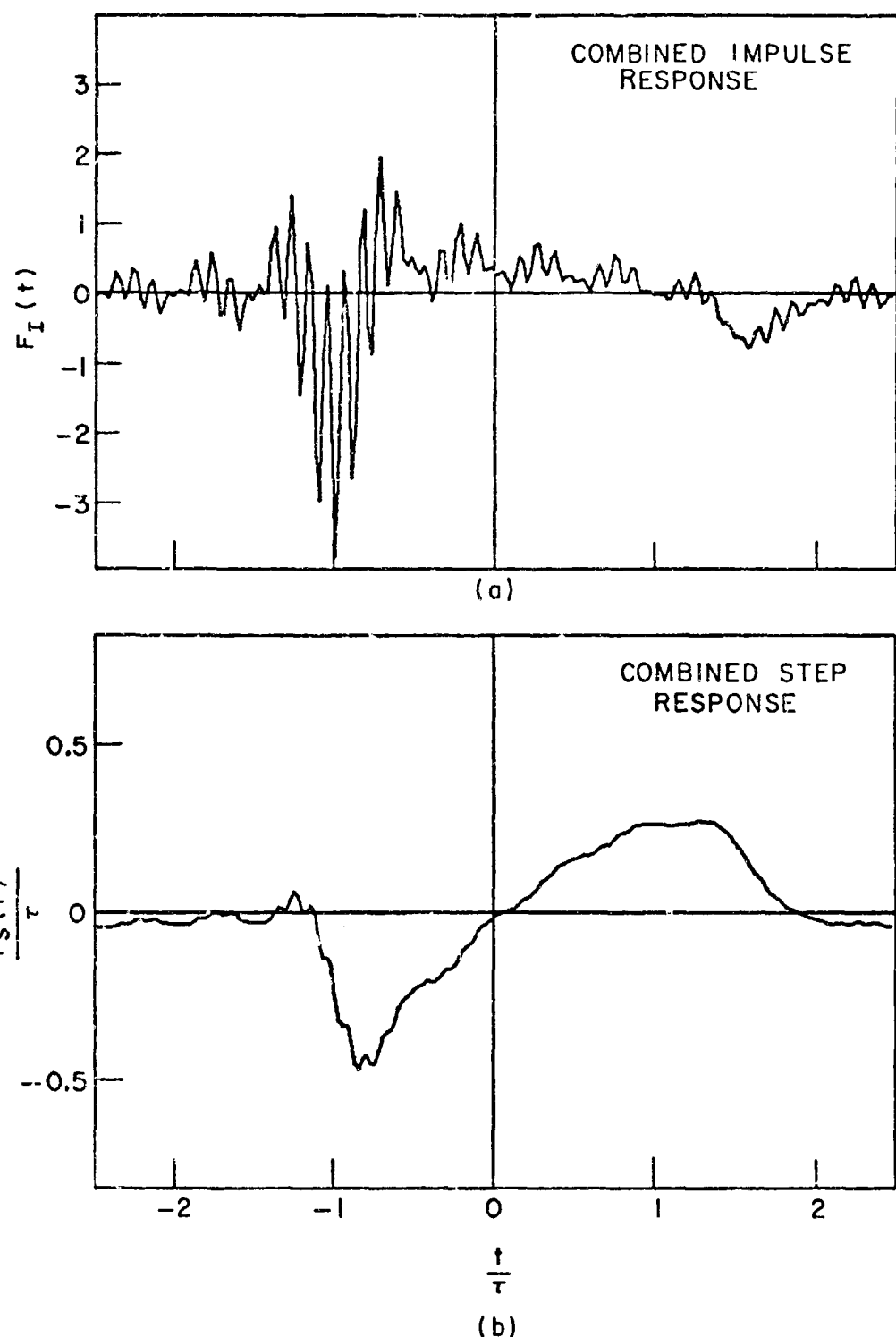


Fig. 28. Unmodified combination of short-pulse and resonance region sphere step and impulse response waveforms.

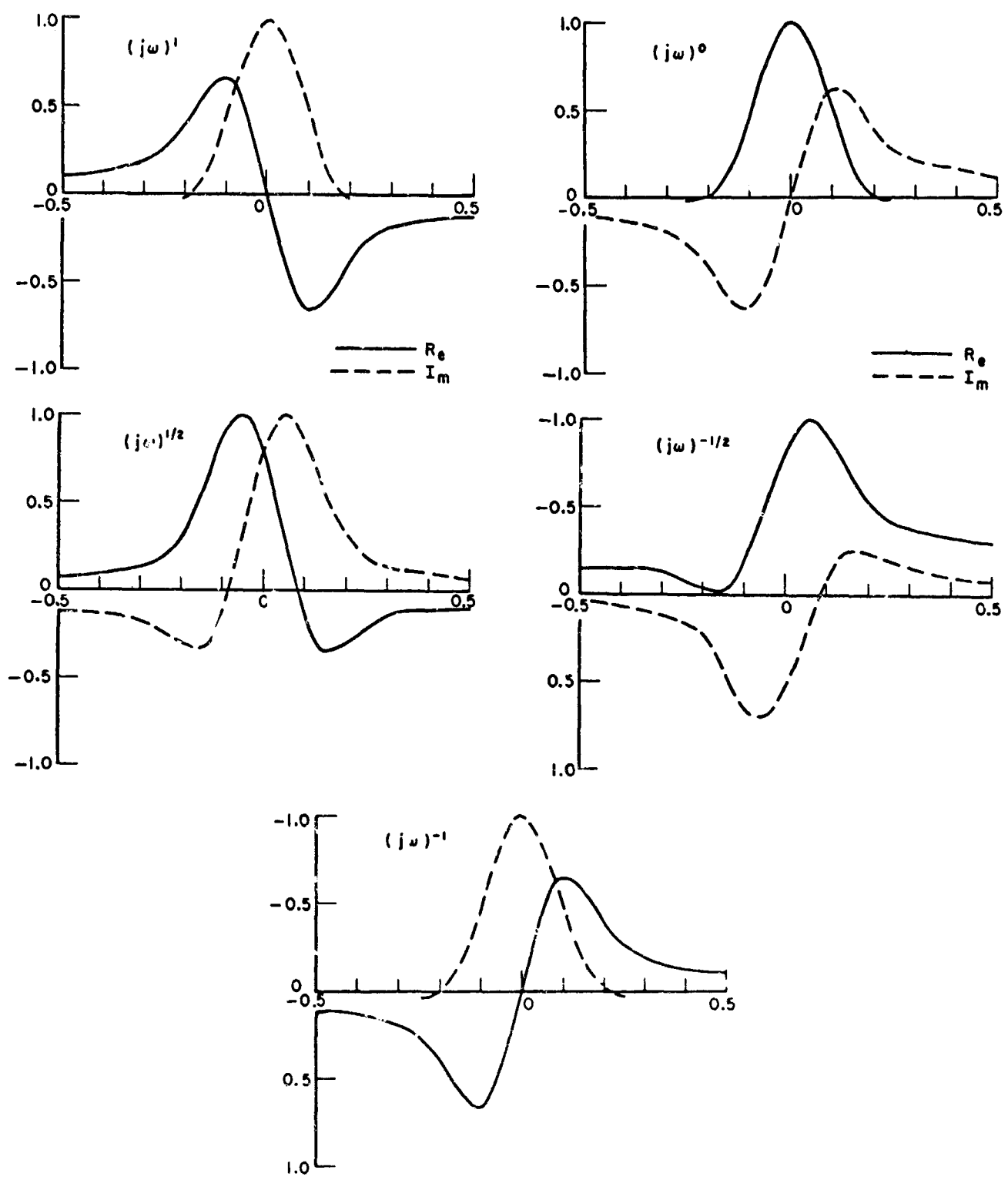


Fig. 29. Down-converted short-pulse waveforms for scattering centers with various frequency behavior characteristics.

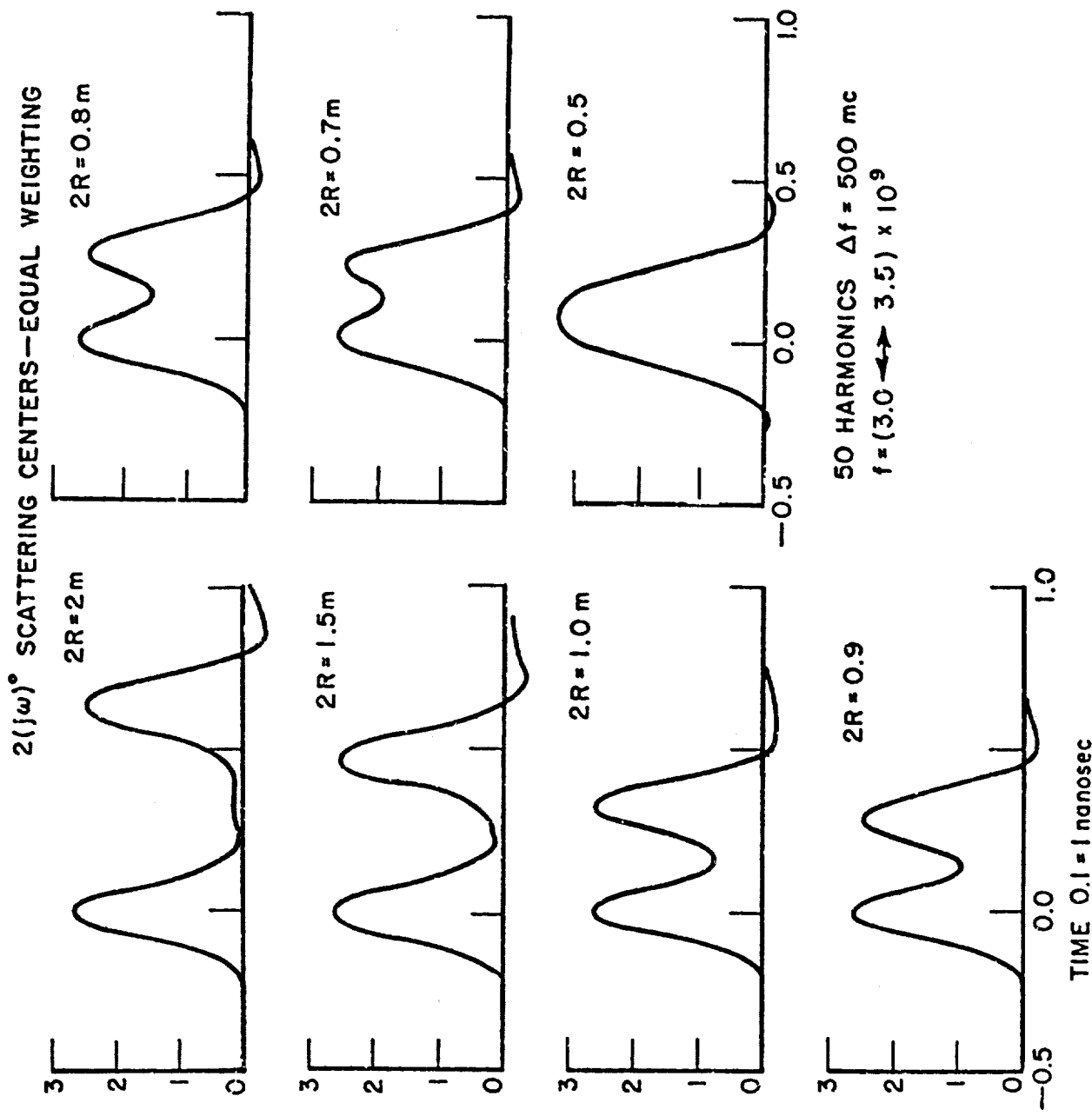


Fig. 30. Real part of the down-converted short-pulse waveform for two types of scattering centers,  $(j\omega)^0$  and  $(j\omega)^{-1}$ , vs range difference  $R$ .

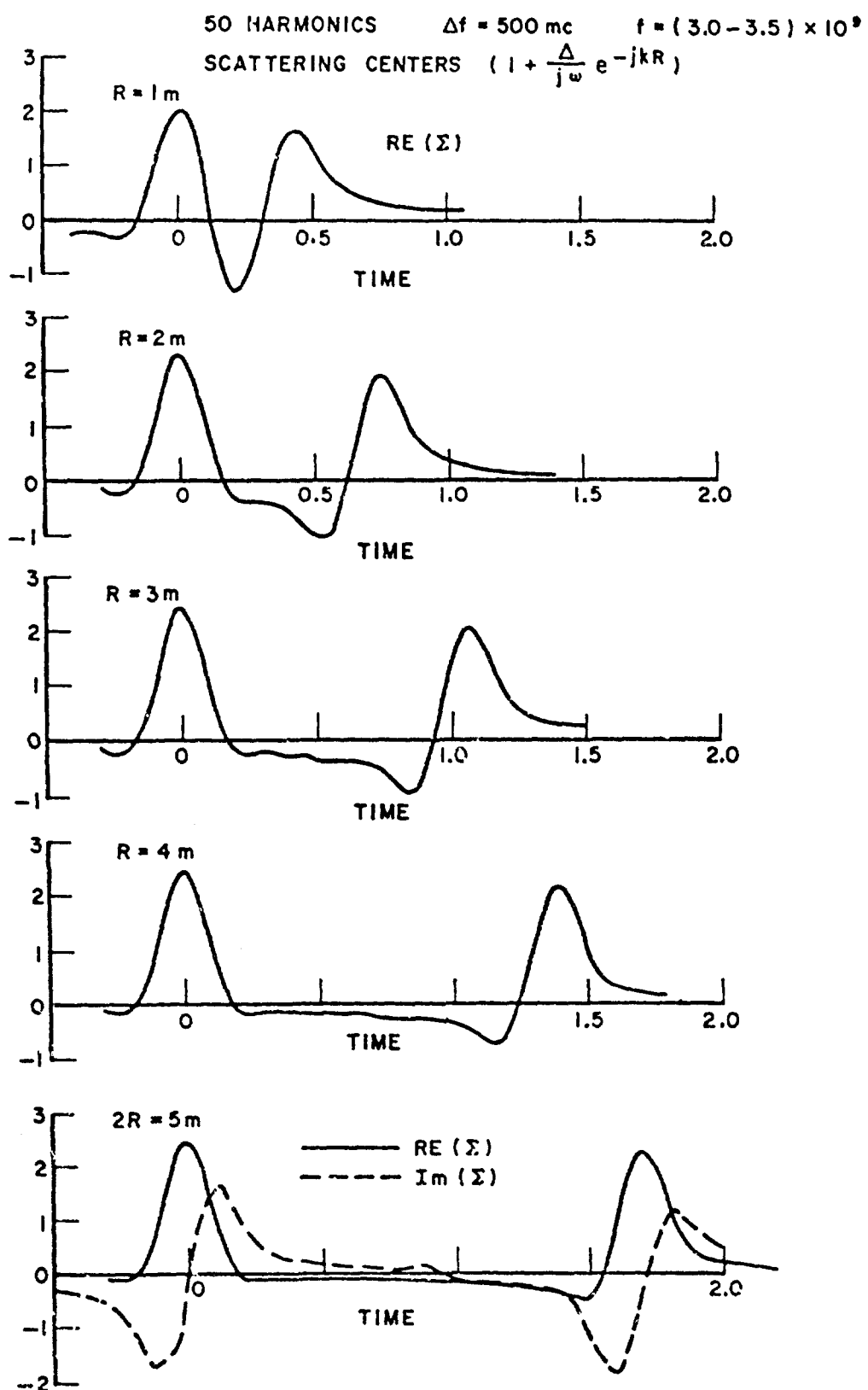


Fig. 31. Real part of the down-converted short-pulse waveform for two types of scattering centers,  $(j\omega)^0$  and  $(j\omega)^{-1}$ , vs range difference  $R$ .

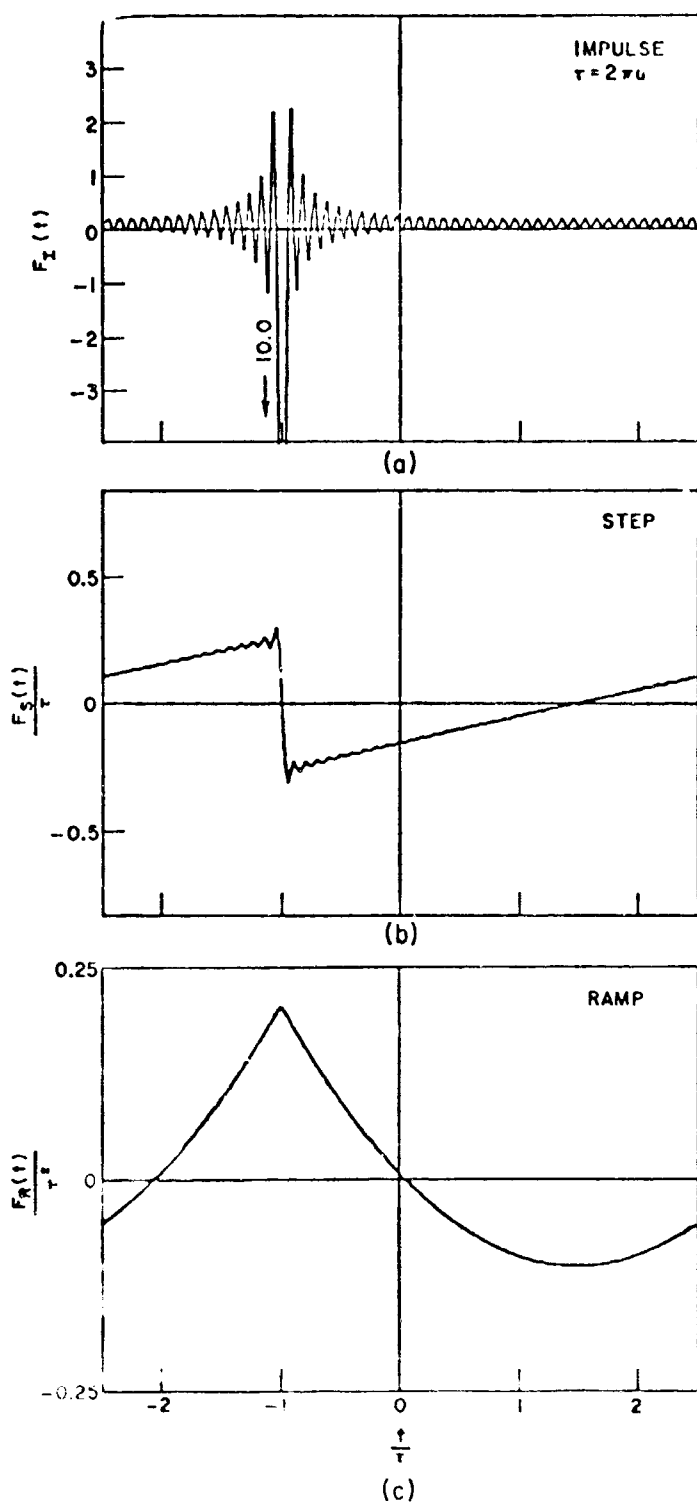


Fig. 3c. Short-pulse derived approximate impulse and step response waveforms for the sphere.

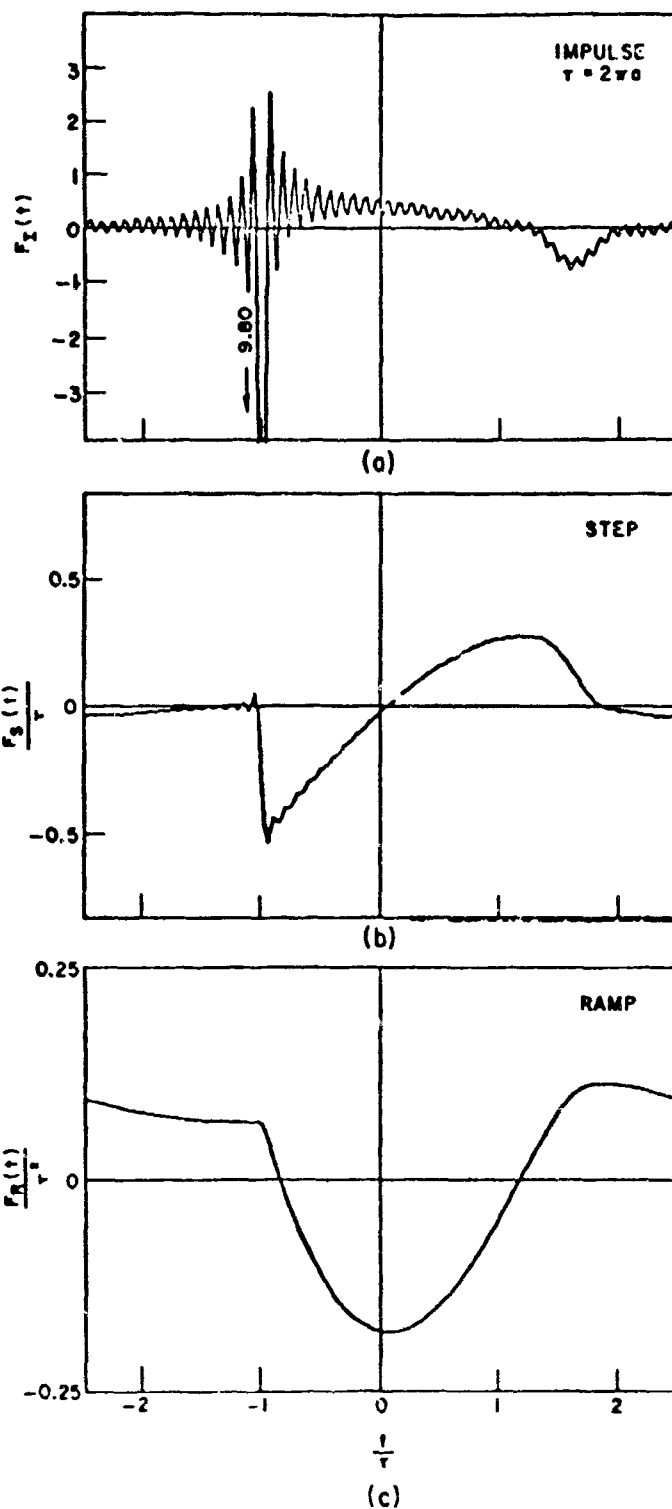


Fig. 33. Combined short-pulse and resonant region approximate sphere response waveforms. 1-10 resonant region harmonics used.

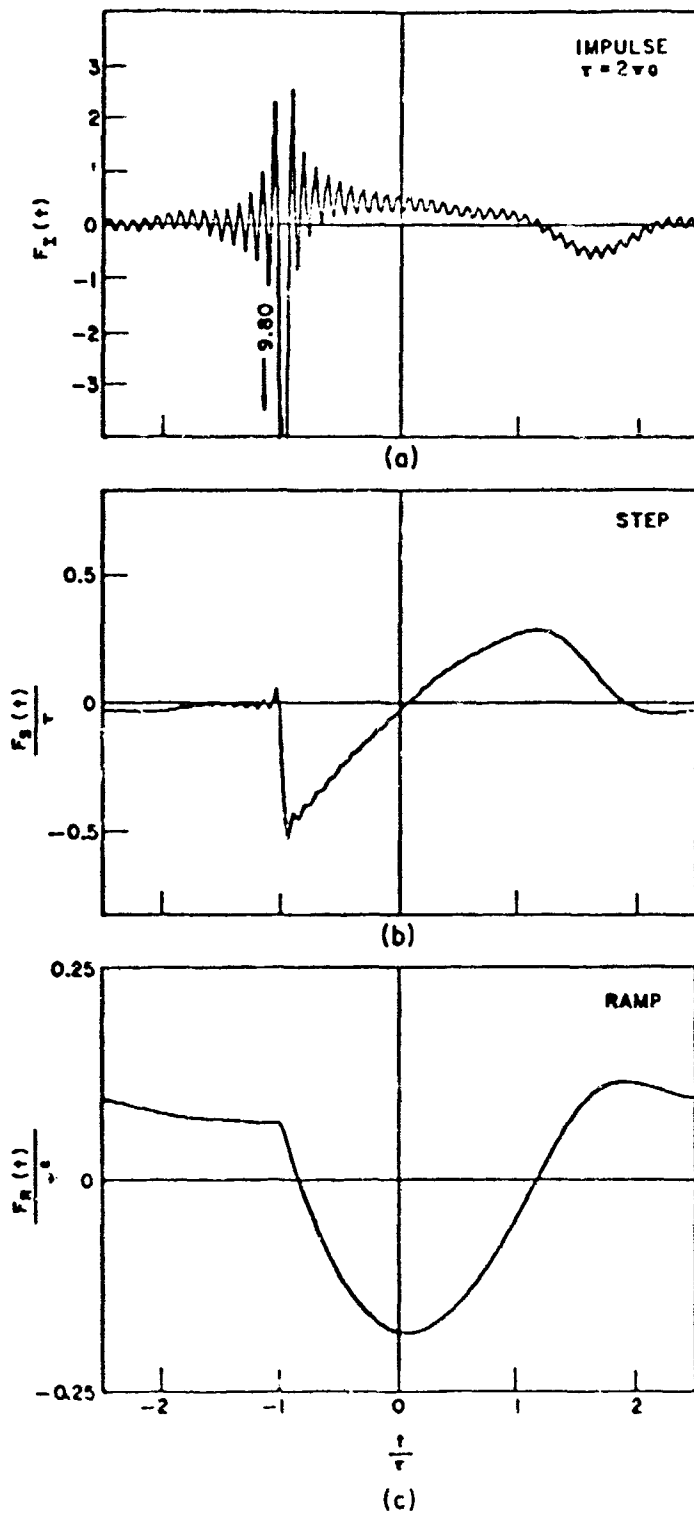


Fig. 34. Combined short-pulse and resonant region approximate sphere response waveforms. 1-5 resonant region harmonics used.

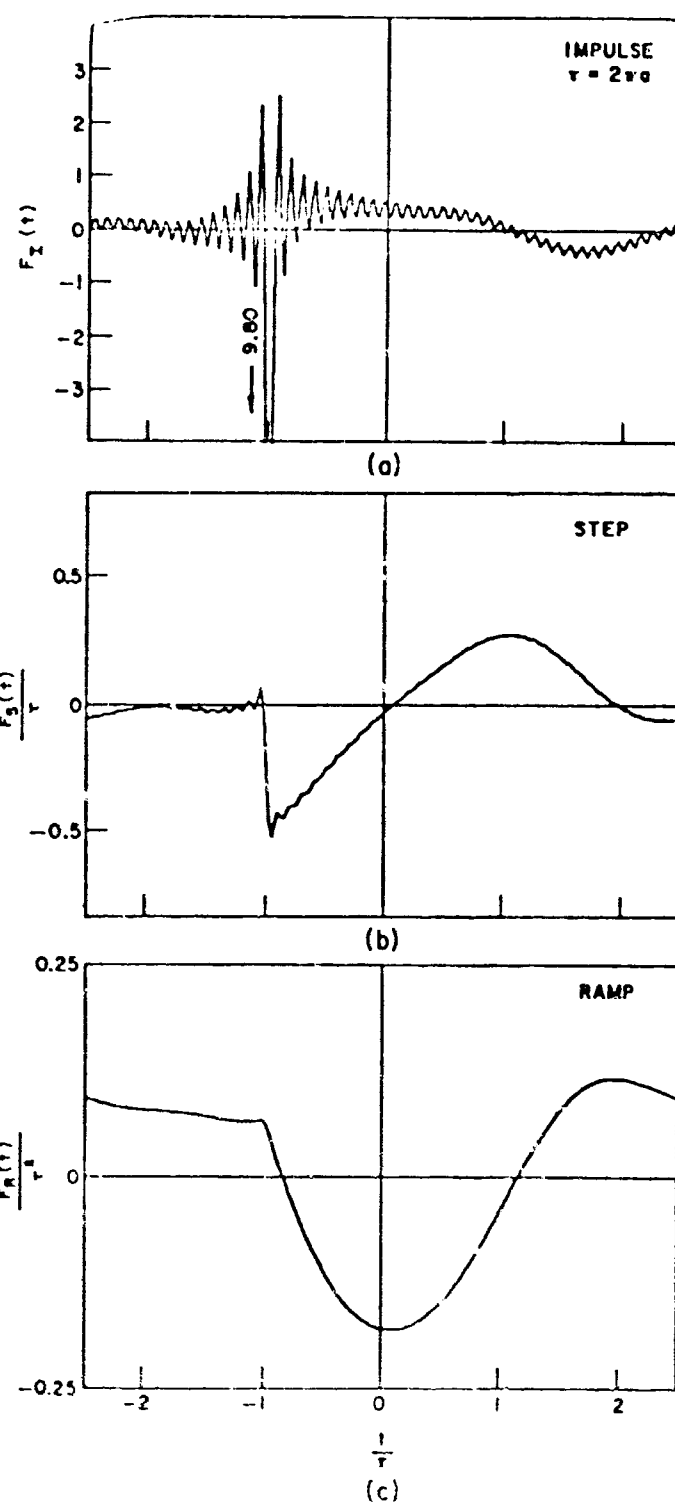


Fig. 35. Combined shear loading and resonant region approximate sphere step and ramp response waveforms. 1-3 resonant region harmonics.

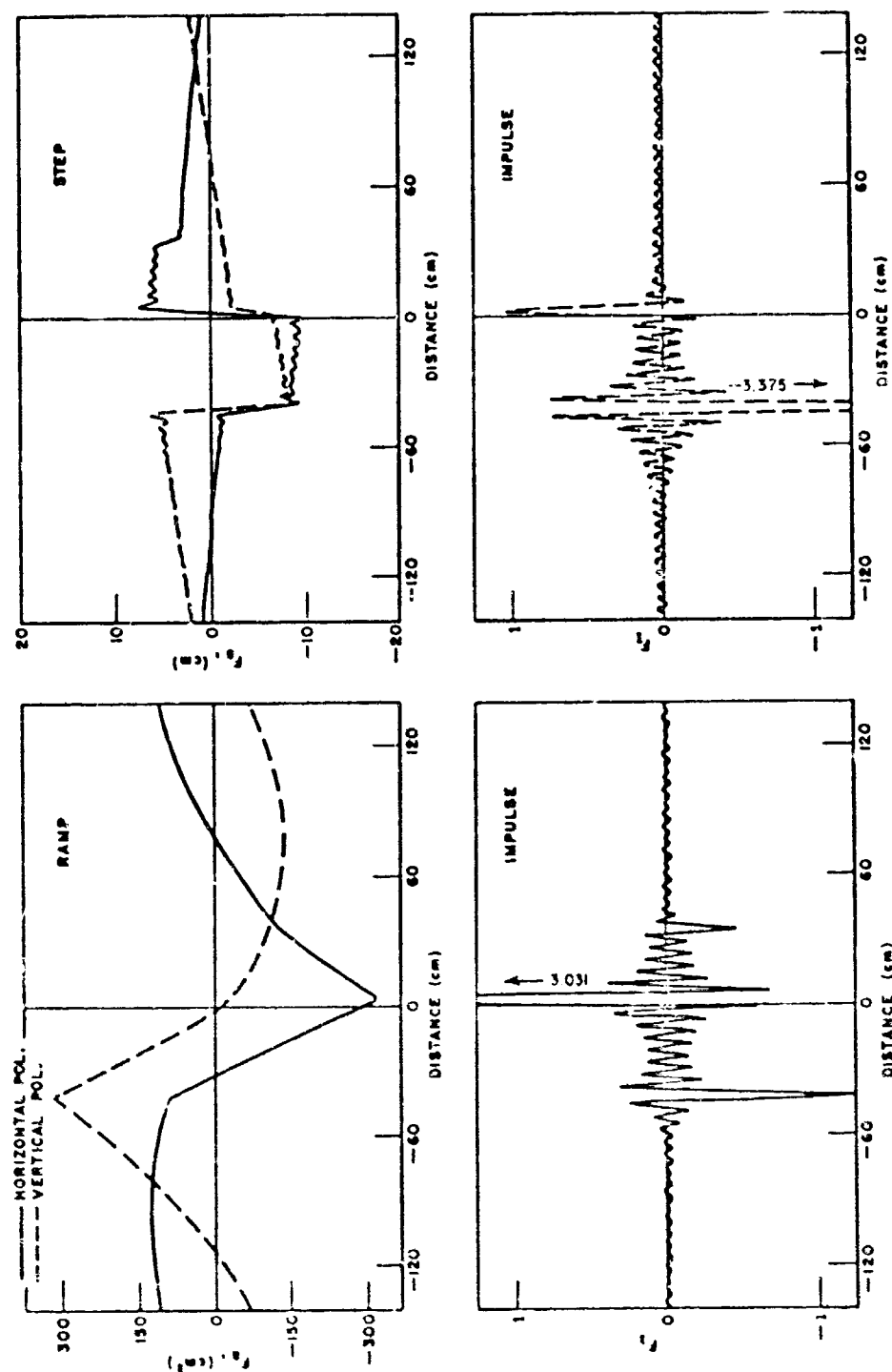


Fig. 36. Short-pulse derived approximate response waveforms for the tube, 450 orientation.

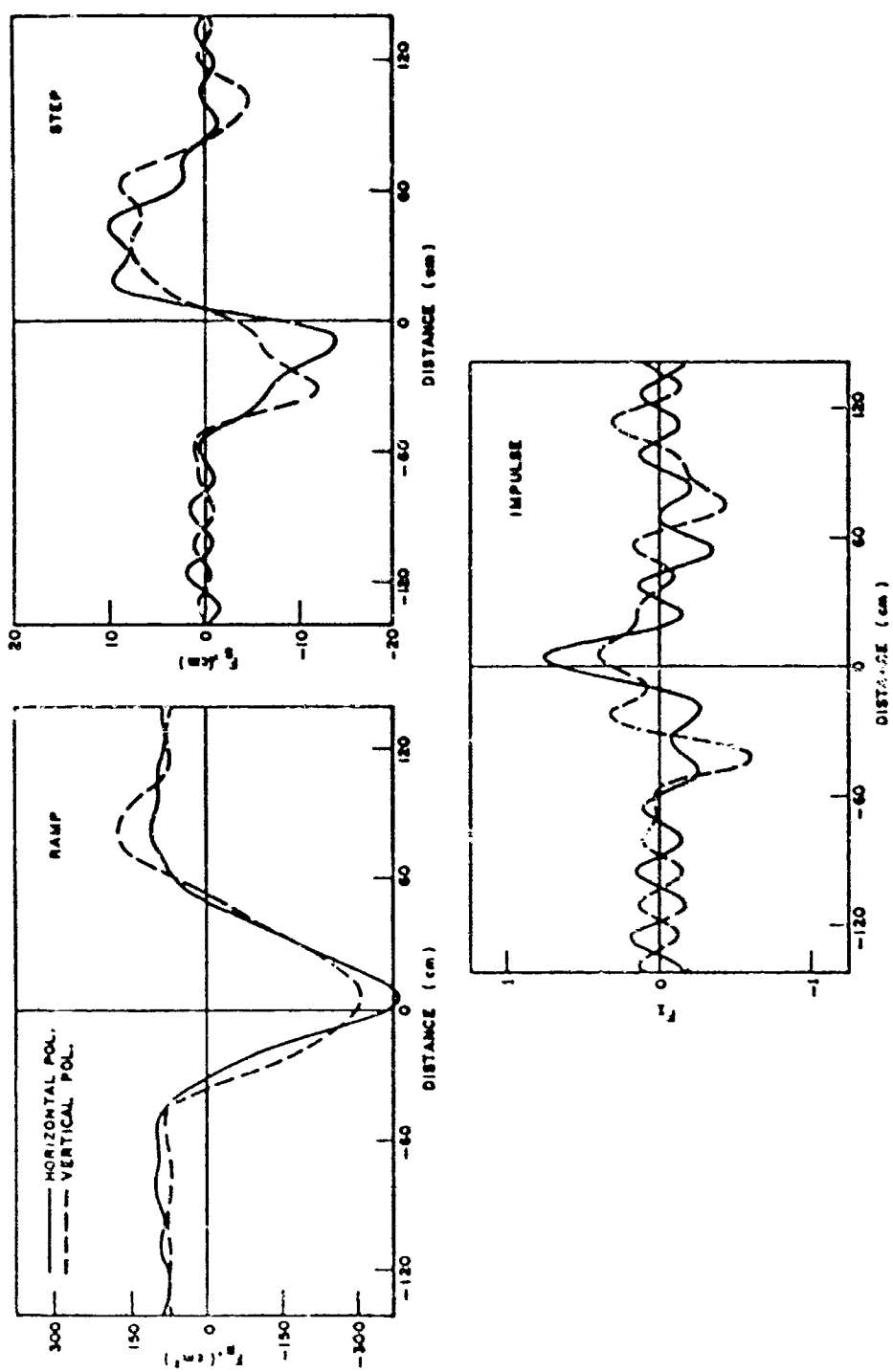


Fig. 37. Ten-frequency resonant region approximate response waveforms for the cube, 450 orientation.

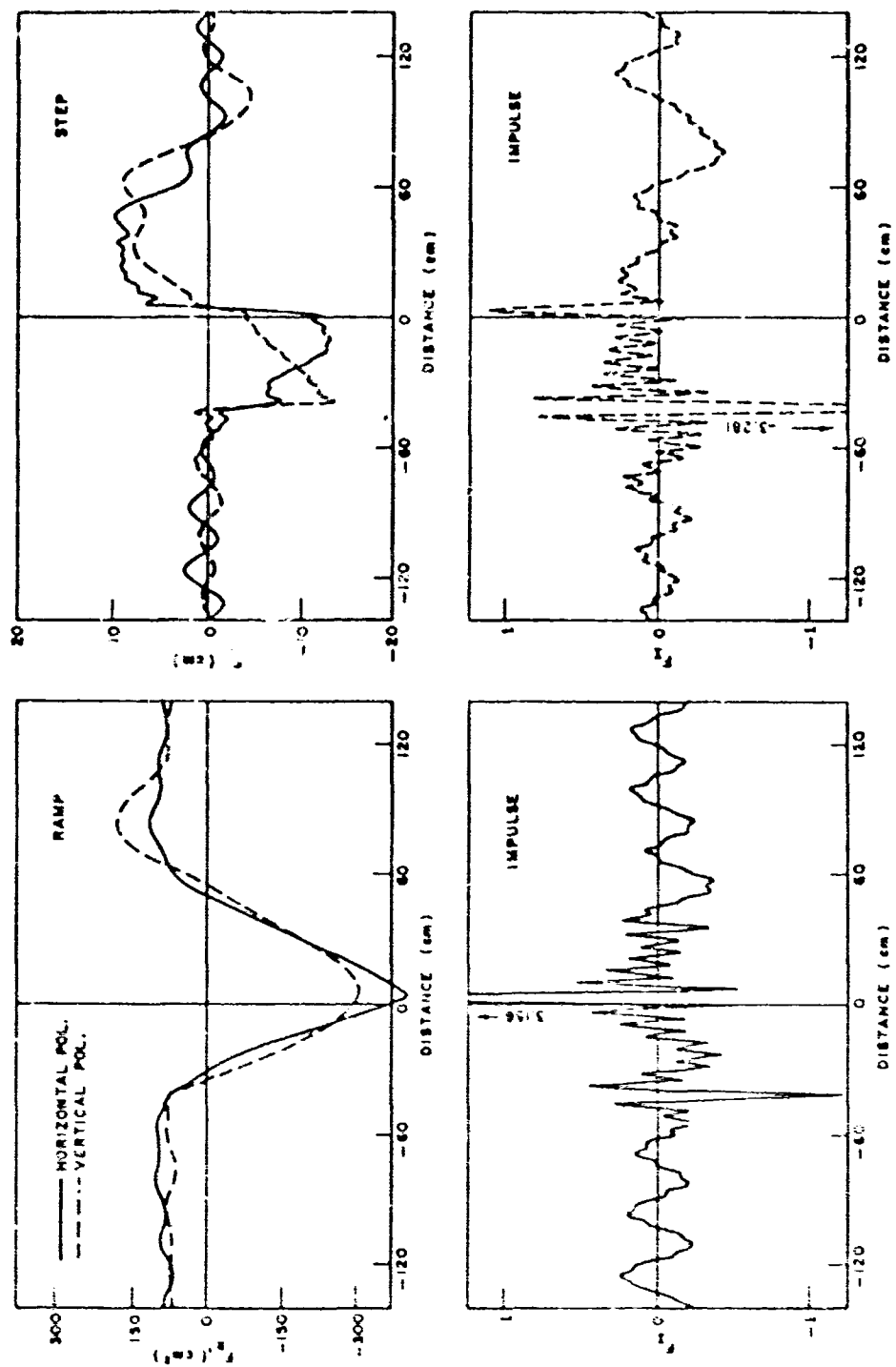


FIG. 38. Combined short-pulse and resonant region approximate response waveforms for the cube, 45° orientation. 10 resonant region harmonics used.

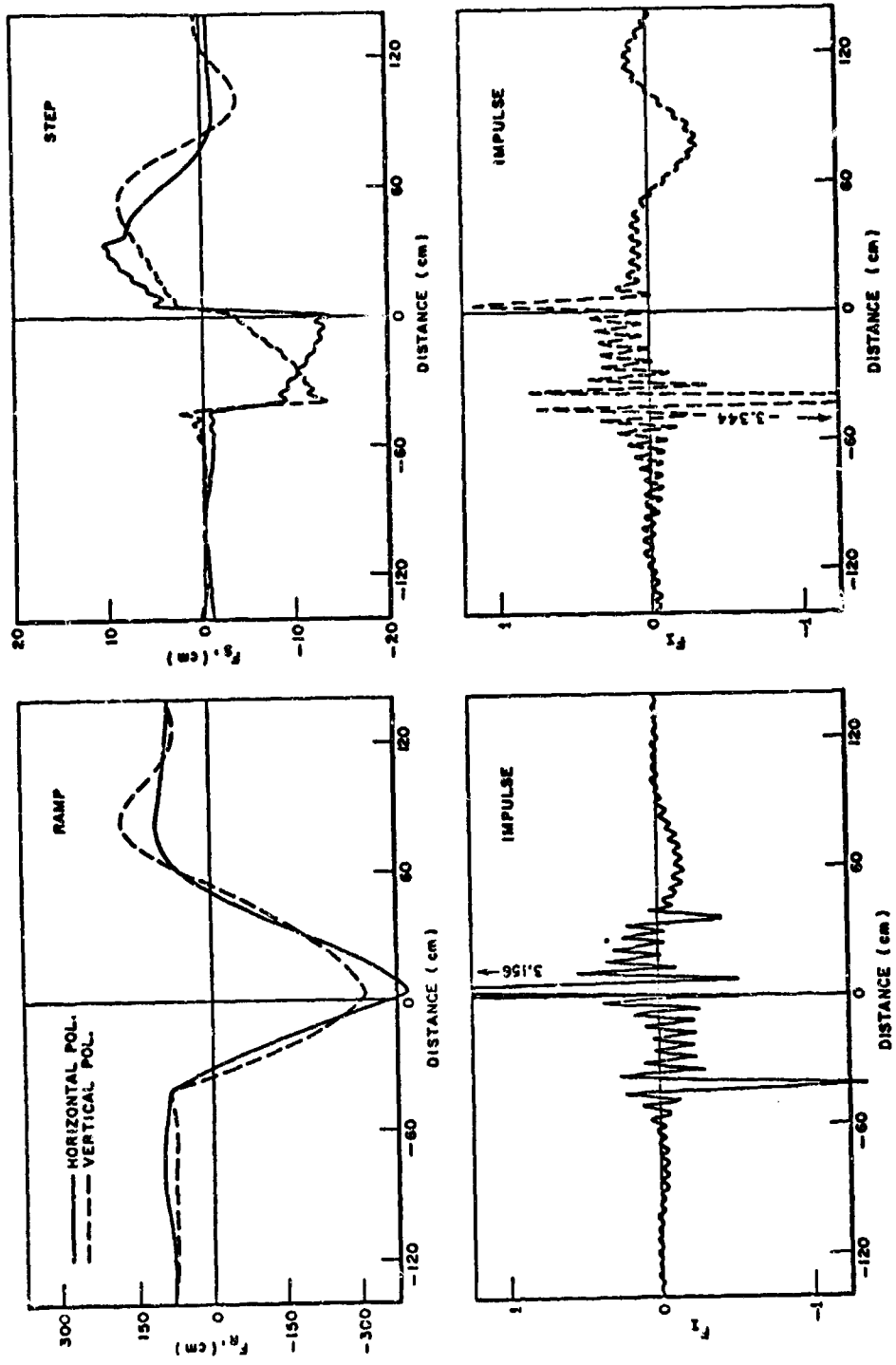


Fig. 39. Combined short-pulse and resonant region approximate response waveforms for the cube, 45° orientation. 5 resonant region harmonics used.

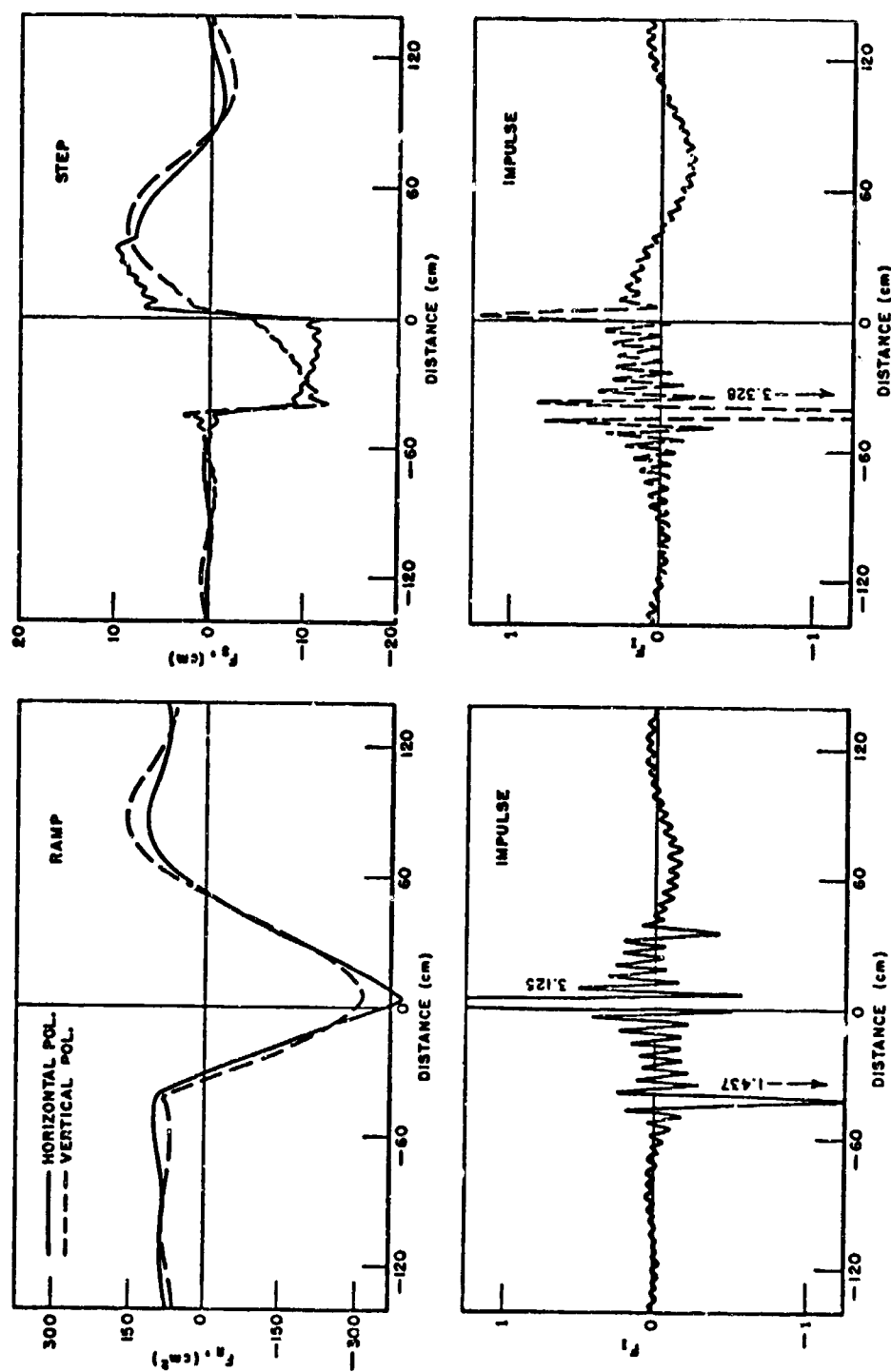


Fig. 40. Combined short-pulse and resonant region approximate response waveforms for the cube, 450 orientation. 3 resonant region harmonics used.

$$\frac{a}{\lambda} = 0.033, 0.067 \dots 1.66$$



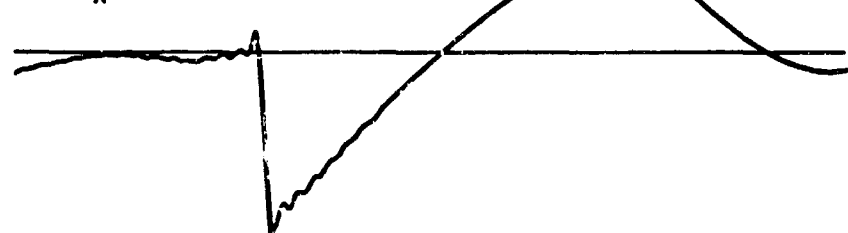
(a)

$$\frac{a}{\lambda} = 0.05, 0.10, 0.15 \dots 2.5$$

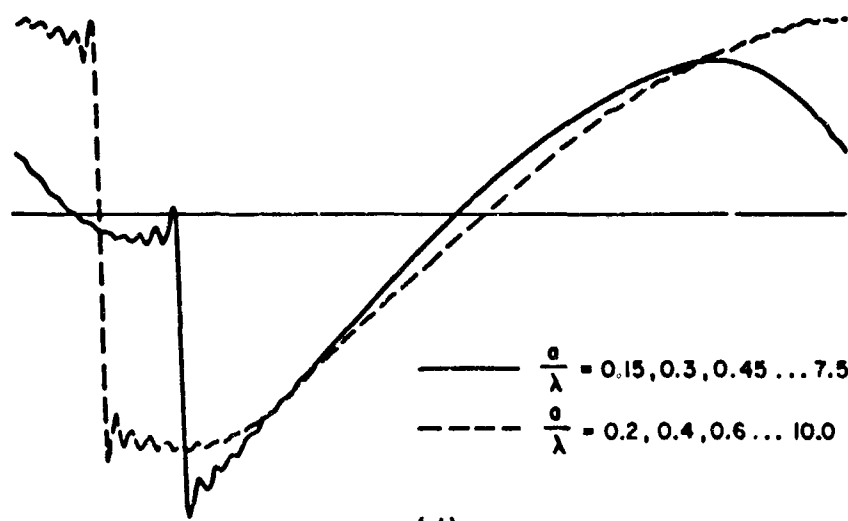


(b)

$$\frac{a}{\lambda} = 0.1, 0.2, 0.3 \dots 5.0$$



(c)



(d)

Fig. 41. Combined short-pulse and three resonant frequency (harmonic number  $n = 1, 2, 3$ ) sphere step response waveforms vs radius in fundamental wavelengths.

#### IV. RADAR IMAGING USING THE TIME-DOMAIN RESPONSE

A portion of the analytical effort on this contract has been devoted to a study of target imaging using the ramp response data which we have measured. Of course a 3-dimensional object picture is a significant indicator of satellite identity. In fact, the questions "What does the satellite look like?" and "What is the identity of the satellite?" are very nearly synonymous. A target image is thus very attractive in an intuitive sense. There are also several objective arguments for obtaining a visual image, however.

One very attractive aspect of a visual image is that it is readily interpreted by the human eye. The component parts of the satellite (antennas, solar cell panels, etc.) are readily assimilated, giving not only physical parameters, but possibly indicating satellite function as well. A newly launched satellite, which may confuse an automated identification process, can be easily identified, classified, and its purpose evaluated with the help of a visual inspection. Changes in the satellite's shape, such as movement of the antenna or solar panels, might also confuse an automated identification scheme, but are readily interpreted and assessed as normal or abnormal using a visual image presentation. In summary, the visual image-human observer team have several capabilities which would be extremely difficult for any automated satellite identification scheme to duplicate.

Because of the sheer quantity and generally routine nature of satellite objects, an automated identification system seems most appropriate for normal operational situations, with the above human observation capability as a supplementary aid. Target imaging techniques have certain advantages in this area as well. An automated identification system, which uses  $N$  measured parameters to classify or look up (library search) a satellite, is most accurate and most comprehensive if the set of  $N$  parameters have physical significance. Thus, by deriving the  $N$  inputs to the automated system from a target image (an artificial replica of the target) a more nearly optimum automated processor should result. A set might include such conventional but significant parameters as volume, motion parameters, maximum dimensions, number and type of major recognizable components, or moment of inertia tensor, all of which can be derived from the object image presentation. The fact that these parameters have physical meaning on their own is another advantage of an image-based input parameter set. It is worthwhile to reiterate that the applicability of all automated processing schemes, no matter how sophisticated, depends on the characteristics of their input parameters, and image-derived parameters offer promising improvements in this respect.

The specific goal of this effort was to investigate techniques for obtaining the target characteristic function  $P(x,y,z)$  where  $P(x,y,z) = 1$  inside the target and  $P(x,y,z) = 0$  outside the target, utilizing ramp response input data. The ramp response waveform was chosen because of

its relative simplicity, ease of measurement, and geometrical significance. The target characteristic function, derived by Bojarski,<sup>12</sup> is a particularly compact and useful approach for defining target shape.

We are aware of another interesting study of imaging by Lewis,<sup>13</sup> and the relationship of the time-domain signature to his technique has been studied. His technique is derived using a physical optics approximation for the current distribution on the scatterer. However, the ramp response on which our studies are based has its major components in the Rayleigh and resonance region of a target's response, where the physical optics assumption does not hold. Hence, the Lewis technique was not used for our study. However, since both studies attempt to define the target characteristic function, a comparison and combination of the results would seem to be a feasible and interesting area for future study.

The subject of this study, the "approximate limiting surface" approach, utilizes the cross-sectional area vs distance information of the ramp response, along with a reasonable assumption on the outlines of the given cross-sectional area, in order to give an approximate target image. For instance, given the cube ramp response waveform of Fig. 42, it is known that the cross-sectional area of a "slice" perpendicular to this line-of-sight at a distance  $x_0$  from the start of the body is  $A$  units. The actual outlines of the slab of cross sectional area  $A$  cannot be deduced from this waveform, however. Let us assume that the slice is elliptical in shape, and centered about a longitudinal body axis. Furthermore, let the ellipticity vary, and permit either a vertical or horizontal elliptical shape. The contour which encloses all ellipses of area  $A$ , either horizontally or vertically oriented, and with varying ellipticities, is shown in Fig. 43, along with some of the ellipses which fit inside it.

A three-dimensional approximate boundary surface is constructed of slices similar to Fig. 43, with sizes proportional to the ramp-response waveform amplitude. For the ramp response waveform of Fig. 42, the limiting surface is shown in an isometric view of Fig. 44. The corresponding target characteristic function is

$$P_1(x,y,z) = 1 \quad \text{where} \quad |y \cdot z| < F(x) + .71 \\ = 0 \quad \quad \quad |y \cdot z| > F(x) + .71$$

$F(x)$  is the waveform in Fig. 42;  $x,y,z$  correspond to the axes in Fig. 44, where the line-of-sight is parallel to the  $x$  axis. Comparing the surface of Fig. 44 to an actual isometric view of the object in Fig. 5, it is obvious that this surface is too approximate at this stage. Note however, that the front face of the object is well represented by the approximate surface. The next step is to add ramp response data from other incidence angles. Surfaces obtained from the top and side views of this object are shown in Figs. 45 and 46 respectively. The corresponding approximate target characteristic functions for these look angles are:

$$P_2(x,y,z) = 1 \text{ when } |x \cdot z| < F(y) + .71 \\ = 0 \text{ elsewhere}$$

for the surface of Fig. 45, and

$$P_3(x,y,z) = 1 \text{ when } |x \cdot y| < F(z) + .71 \\ = 0 \text{ elsewhere}$$

for the surface of Fig. 46,

The improved image is the shape which lies within all three of the above limiting surfaces, and is shown in Fig. 47. The corresponding

$$P(x,y,z) = P_1(x,y,z) \cup P_2(x,y,z) \cup P_3(x,y,z)$$

or

$$P(x,y,z) = 1 \text{ when} \quad \begin{aligned} |yz| &< F_1(x) + .71 \\ |xz| &< F_2(y) + .71 \\ |xy| &< F_3(z) + .71 \end{aligned} \\ = 0 \text{ elsewhere.}$$

The cusps which appear in Figs. 44, 45, 46 and 47 are one error feature of the image which can be eliminated. When this imaging technique is used, such cusps will always appear at locations corresponding to a sharp discontinuity in the input ramp waveforms. When band-limited ramp waveform approximations are used, such as the ones of Fig. 42, their finite rise times and lack of any sharp corners produce the cusp. It can be argued, however, that precisely because of the limited bandwidth of the waveforms, image features with the sharpness of these cusps should not occur in a valid image. If the spatial Fourier transform were calculated for the image of Fig. 47, and then those components above the frequency band of the input waveforms were filtered out, and finally a revised image produced using an inverse spatial Fourier transform, it is estimated that the image of Fig. 48 would result. Comparing this image to Fig. 5 it can be seen that a valid image has resulted for this object at this orientation.

Recent results of combining short pulse data and resonant region data also promise to alleviate the cusp errors. As shown in Figs. 33 through 41, the ramp response waveforms resulting from combining two data types have very short risetimes and faithfully reproduce relatively sharp discontinuities. Use of these improved waveforms in our imaging process should eliminate the need for spatial filtering in order to prevent cusp errors.

The above image figures were hand-drawn. Based on encouraging results the technique was programmed on our instrumentation computer. The program will produce an isometric view of the image from ramp response waveforms for three orthogonal look angles as the input. It should be stressed that the basic imaging technique does not require orthogonal look angles, and that it could use an arbitrary number of looks. Also, the isometric view is only one way of visually presenting the three-dimensional information on total body shape which is contained in the target characteristic function. The storage limitation in our instrumentation computer is one reason for the simplification of the technique to a 3 orthogonal look, isometric view approach.

Several computer-plotted images are shown in Figs. 49 through 57. The input data for these images are denoted on each title as "measured" or "calculated". The measured input data are ten-frequency ramp waveforms from our experimental facility. These waveforms are modified in two ways in the image processing. The D.C. level of the waveforms is shifted so that the amplitude is approximately zero ahead of the target response. Then, the waveform is inverted, and the negative trailing portion is eliminated. Figure 58 shows a typical ramp waveform and its revised form as used in the imaging process.

It is known that a portion of the error inherent in this imaging process is due to the disparity between the ramp response waveform and the actual cross-section vs distance characteristics, as discussed in Section II. This includes the finite rise time due to terminating the Fourier series after 10 terms and the reduced accuracy in the shadow region. The shadow region inaccuracies are observable in Figs. 49 and 53 as a degradation of the image in the bottom and rear quadrants. As indicated in Section II, further study of the ramp waveform, possibly leading to simple modifications for greater correspondence to cross section, are recommended in order to improve image accuracy in the above respects.

In order to examine the characteristics of the basic approach, the ramp response errors were eliminated by using actual cross sectional area vs distance waveforms as input in those images labeled "calculated". The objective is thus to discover a technique which produces perfect images for perfect cross-sectional input data. The "calculated" figures demonstrate that good images can be obtained for a variety of simple shapes.

One problem area for the present imaging process is demonstrated by Figs. 59 through 63, which correspond to a 2:1 square cylinder whose major axis is rotated with respect to the look angle reference frame. It is seen that degradation of the image occurs when the object axes vary more than a few degrees from their alignment with the look angle reference frame. The cause and detection of this type of error have been studied, and a possible solution proposed.

It seems that the principal cause of this error is the original assumption that the center of all cross-sectional slabs for the limiting surface of each look angle must be aligned parallel to the line of sight.

As shown in Fig. 64, the center line of the actual cross-sectional area slabs for the off-axis oriented 2:1 square cylinder do not satisfy this assumption. For the cube image at 45° shown in Fig. 65, several faces of the object are not perpendicular to any of the look angles, the same as for the 2:1 square cylinder of Fig. 63. Yet it is seen that since the centers of the cross-sectional area slices are parallel to the look angles in the case of the 45° cube, a satisfactory image results, thus illustrating the importance that center line alignment plays in this imaging process.

An objective indication of when the images, such as those of Figs. 60 through 63, are in error does exist. If cross-sectional vs distance waveforms of the image of Fig. 62 are calculated, it is found that they differ significantly from the input waveforms, as shown in Fig. 66. Thus, it is known that the image is in error without knowing a priori what the image should look like. With an iterative computer program, it would therefore seem possible for the operator to adjust the limiting surface center-lines until the correct image was obtained. A more rapid and direct method of doing this task seems desirable, however.

The Rayleigh region response amplitude vs polarization appears to be one way of estimating target orientation and gross shape as well. For a 2:1 prolate spheroid, for example, the Rayleigh coefficient vs E field polarization  $\phi$  is shown in Fig. 67. The angle of maximum Rayleigh return corresponds to the orientation of the major axis. Furthermore, the ratio of the maximum to minimum Rayleigh return appears to be approximately equal to the silhouette aspect ratio. For the spheroid, max-to-min Rayleigh return ratio vs silhouette aspect ratio are plotted for several values of incidence angles  $\theta$  with respect to the spheroid major axis. Thus, using polarization control on a Rayleigh region frequency for a target measurement at three look angles it seems possible to define the orientation and shape of an ellipsoidal approximation of a radar target. There was not sufficient time during this program to actually modify our imaging technique to make use of this additional information. Such a modification seems advisable as the next step in an imaging investigation.

From the above discussion it is obvious that the study of radar target imaging using time domain response waveforms has only begun. The promising technique described above will probably be revised as study progresses, and non-orthogonal look angles remain to be investigated. At the present point in this investigation, it can be concluded that:

1. The geometrical implications of time-domain signature data make them especially suitable as a basis for target image studies.

2. The Rayleigh and resonance region scattering data embodied in the ramp response waveform are different enough in character from optical region data to require different, and possibly complimentary imaging methods from the optical data.
3. The preliminary results of ramp response imaging, and the many area remaining for investigation and improvement of the technique merit further concentrated effort in this area.

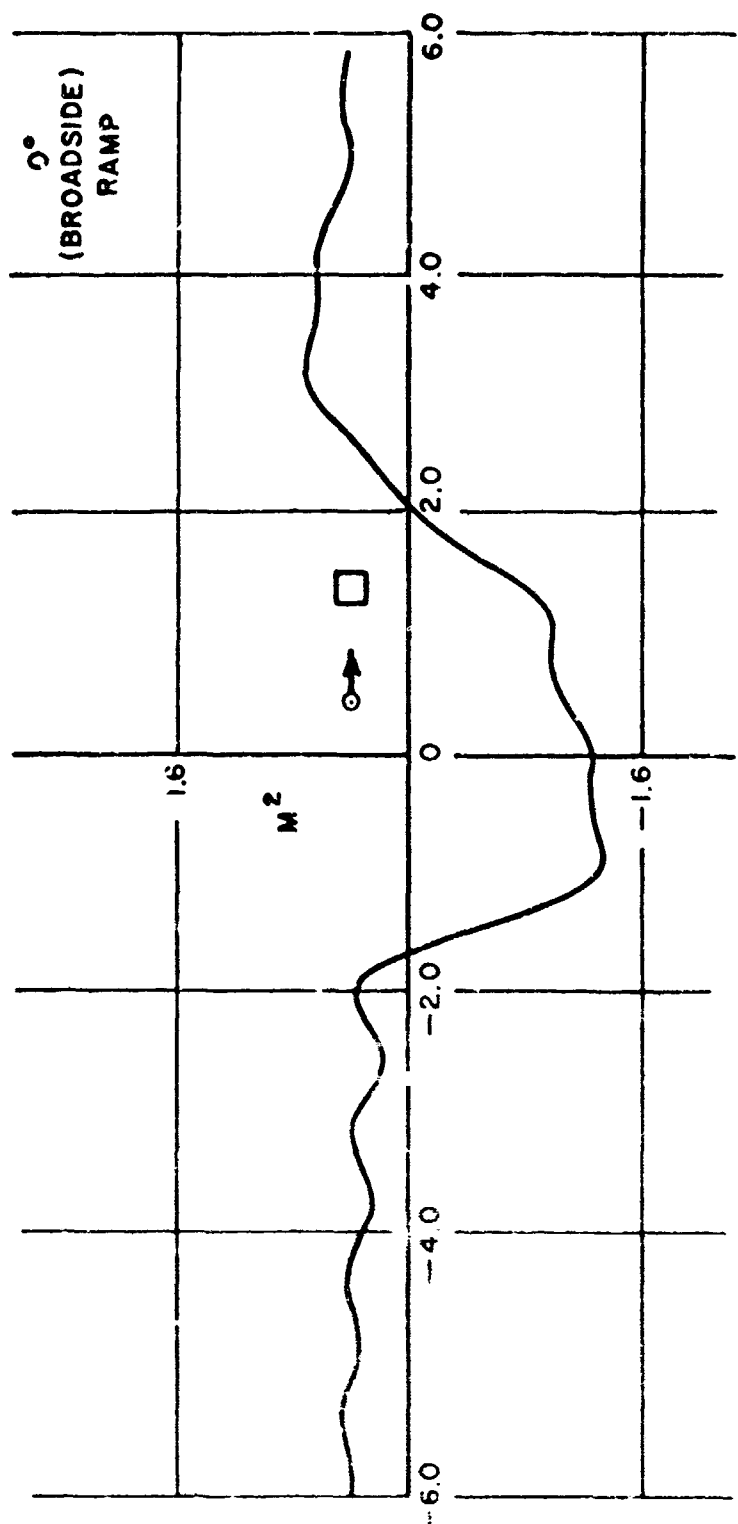


Fig. 2. Cube ramp response waveform.

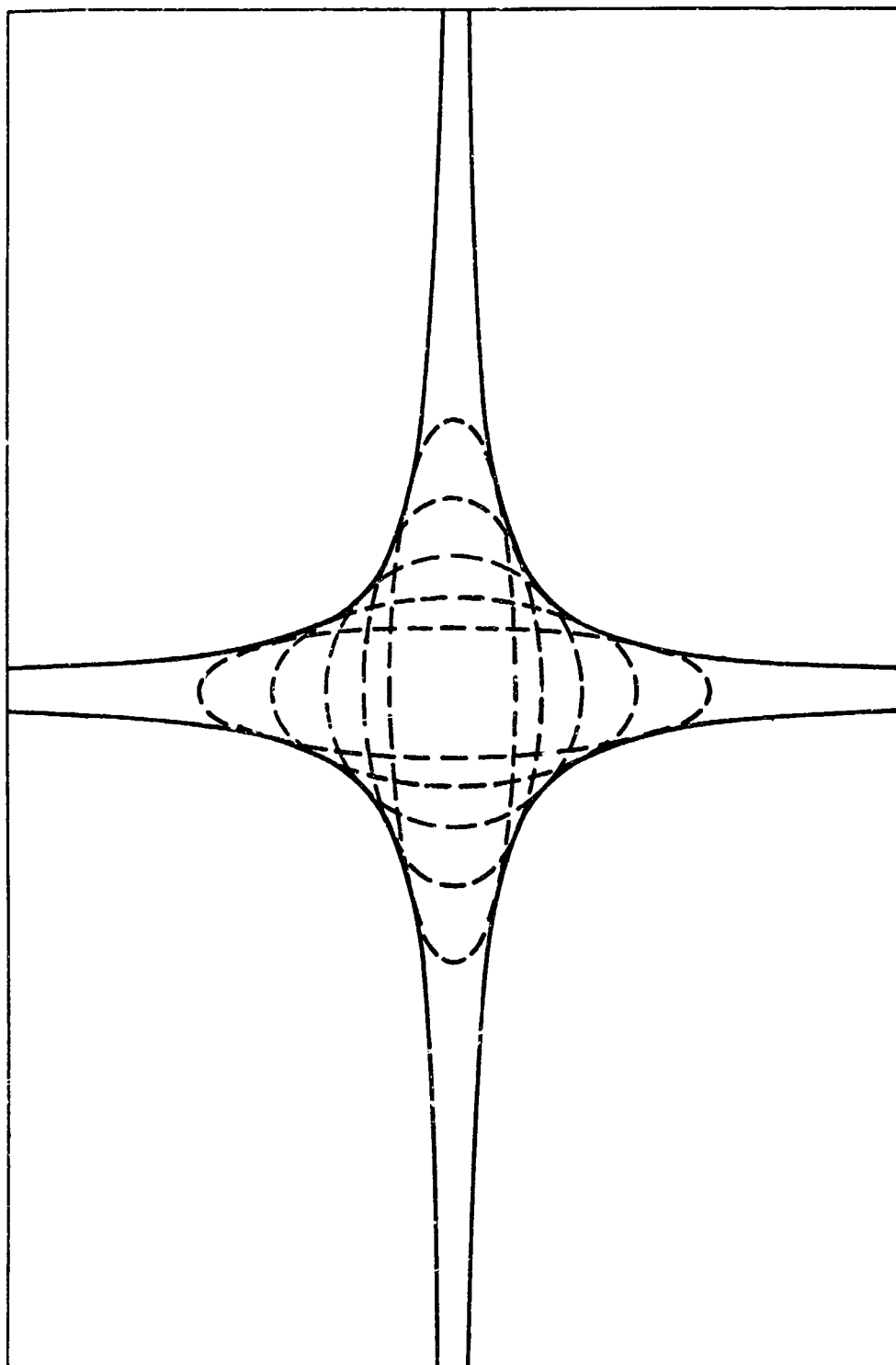


Fig. 43. Approximate limiting contour of a slab  
of given cross-sectional area.

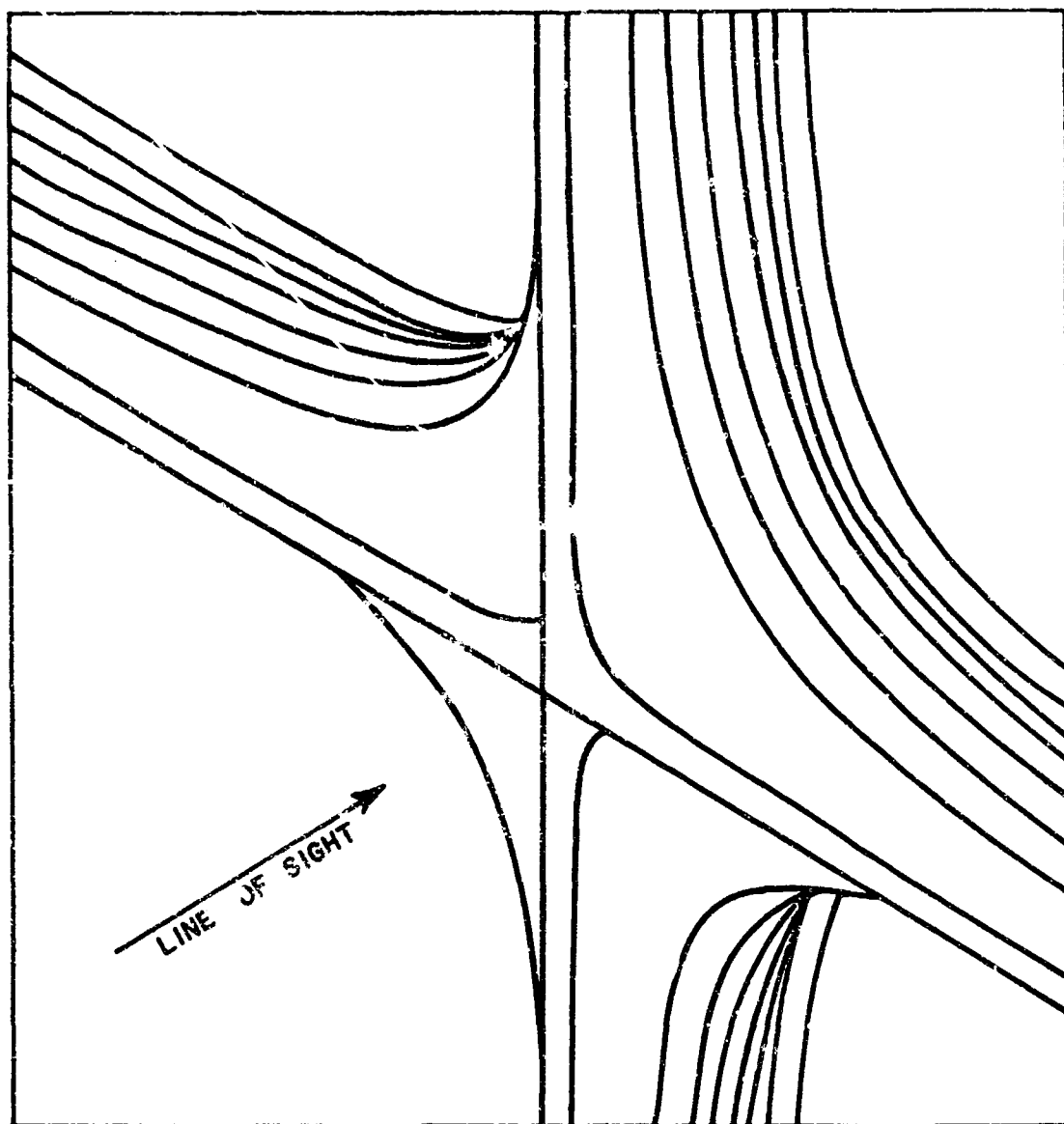


Fig. 44. Approximate limiting surface for a cube,  
derived from front look angle ramp  
response.

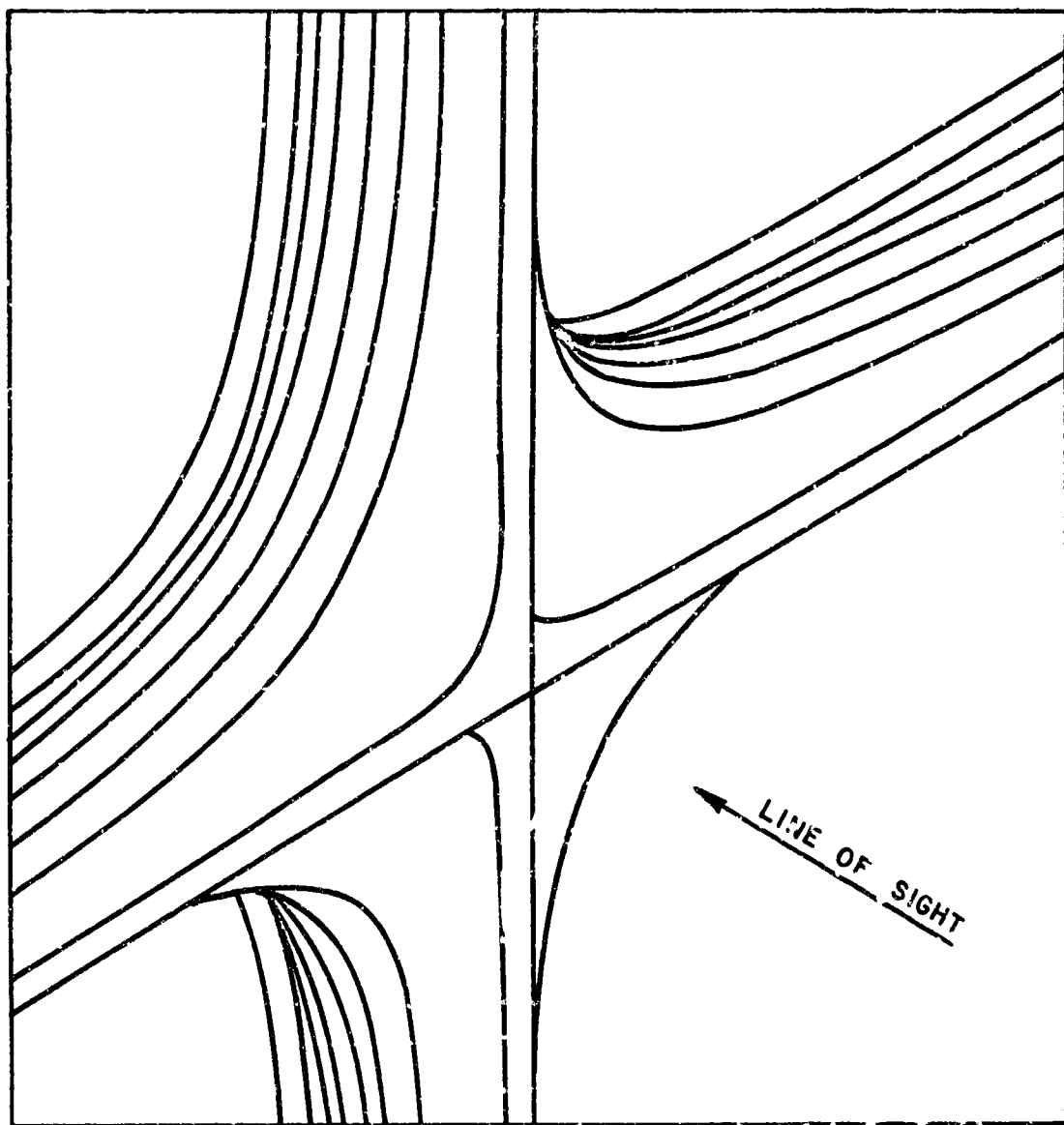


Fig. 45. Approximate limiting surface for a cube,  
derived from side look angle ramp response.

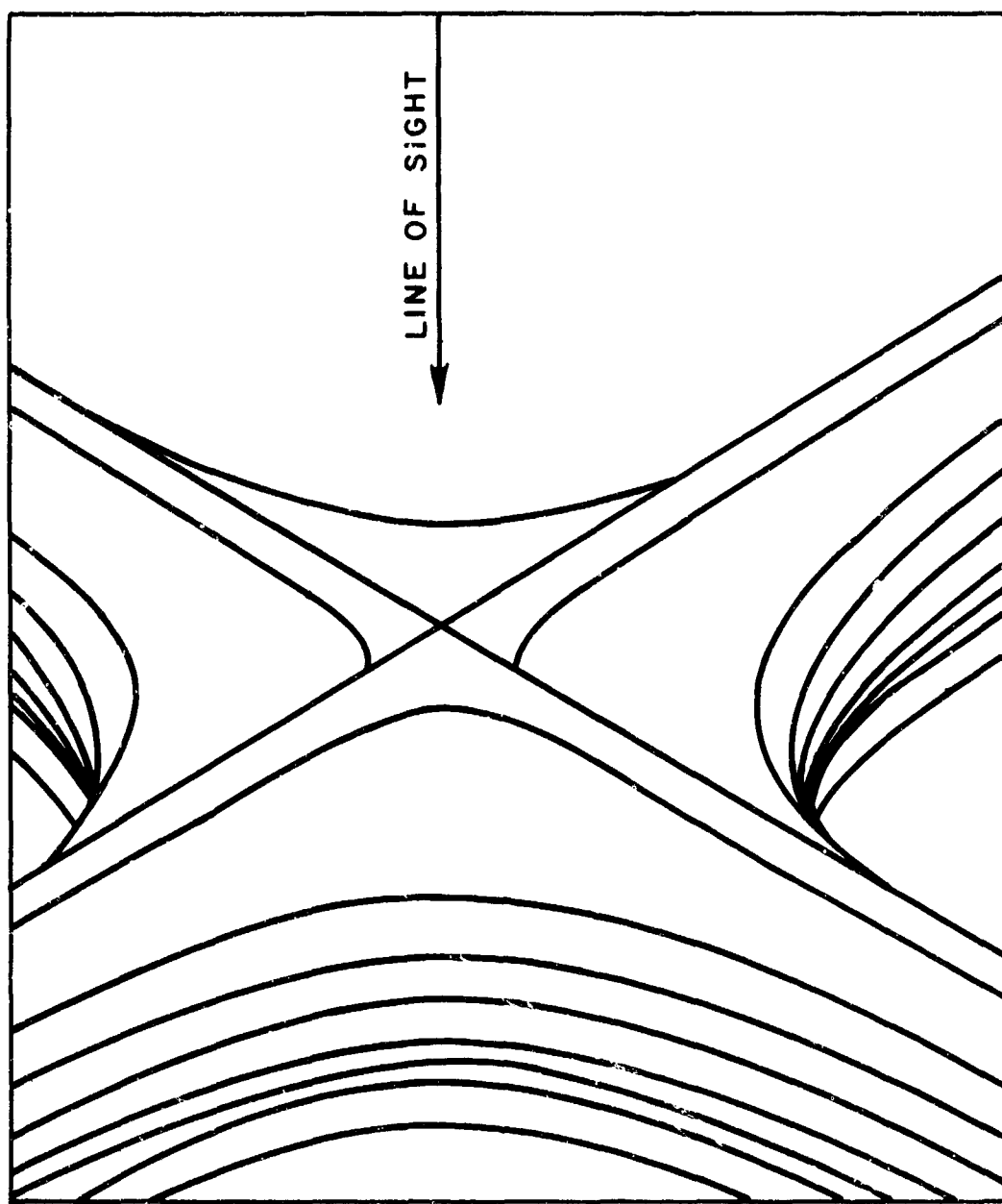


Fig. 46. Approximate limiting surface for a cube,  
derived from top look angle ramp response.

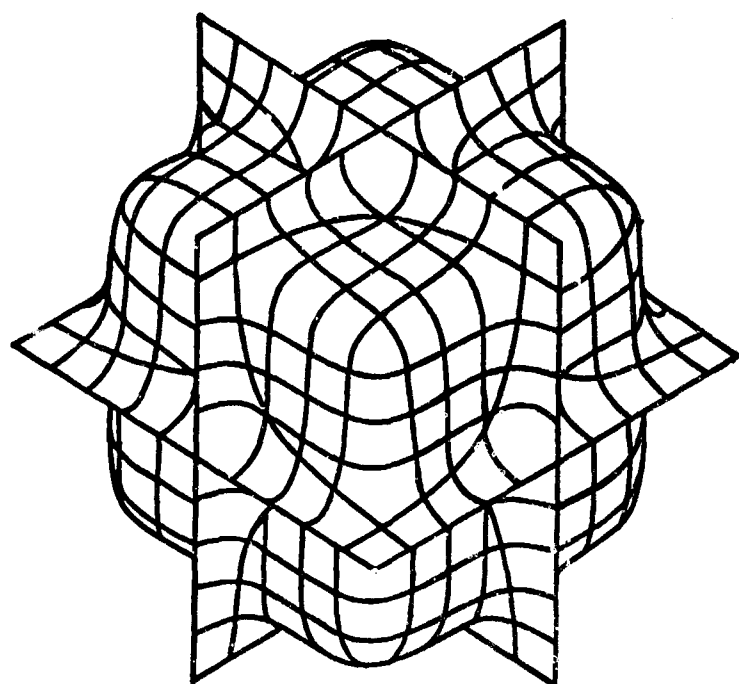


Fig. 47. Approximate limiting surface for a cube,  
derived from all three previous look angles.

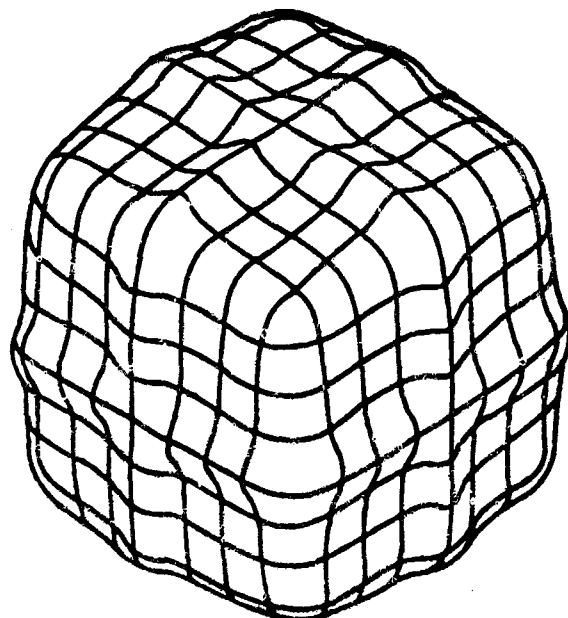
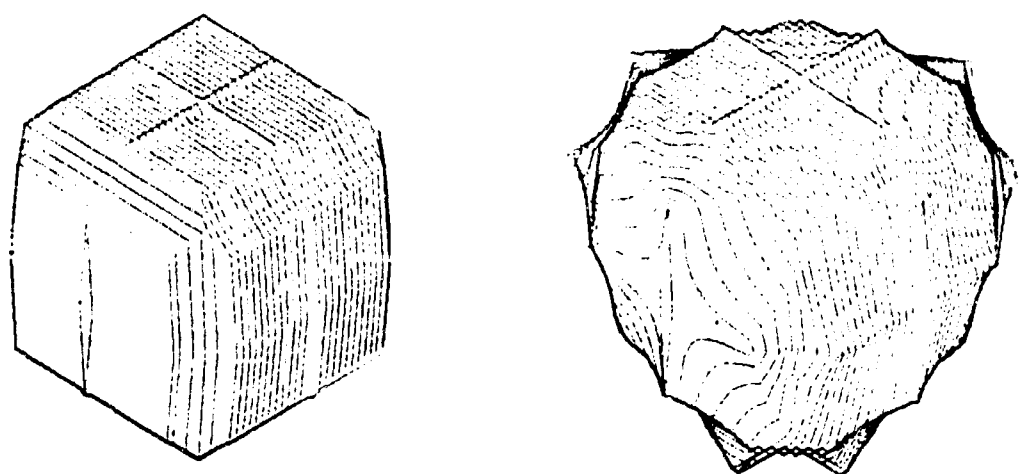


Fig. 48. Spatial filtered version of Fig. 47.



(a) CALCULATED

(b) MEASURED

Fig. 49. Cube images, measured and calculated input data.

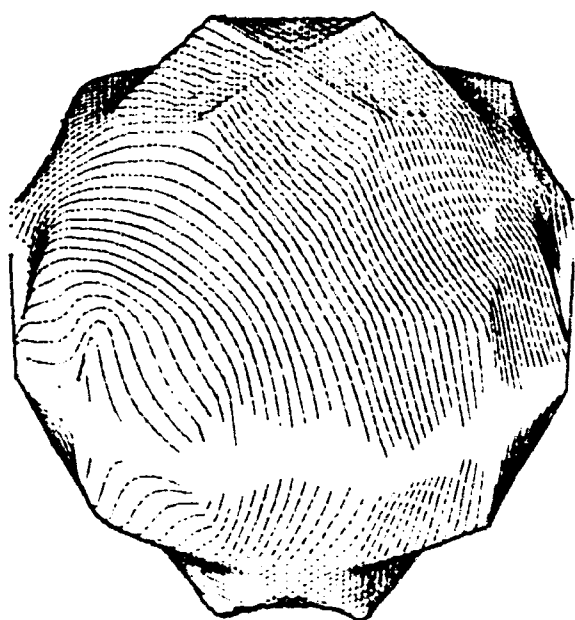


Fig. 50. Sphere image, measured input data.

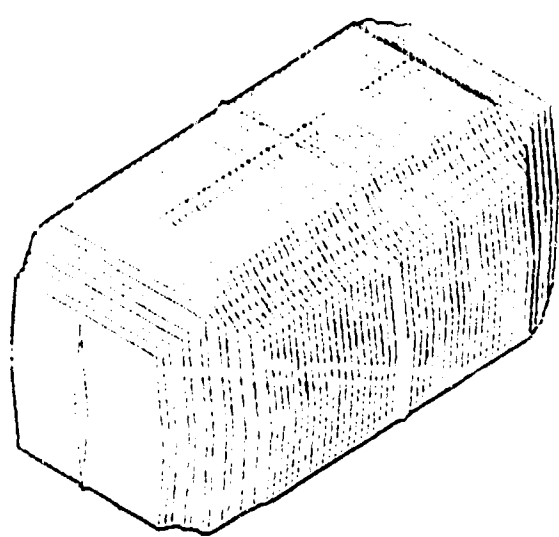


Fig. 51. 2:1 square cylinder image, calculated input data.

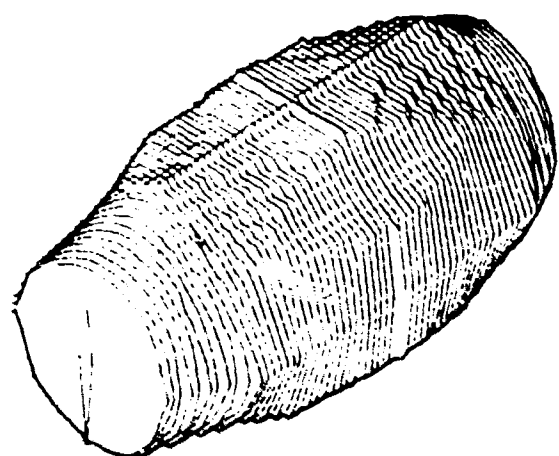


Fig. 52. 2:1 circular cylinder image, calculated input data.

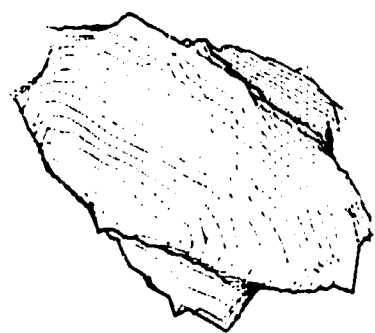


Fig. 53. 2:1 cylinder image, measured input data.

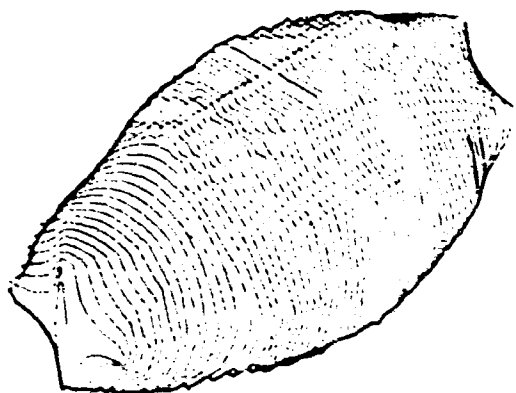


Fig. 54. 2:1 spheroid image, calculated input data.

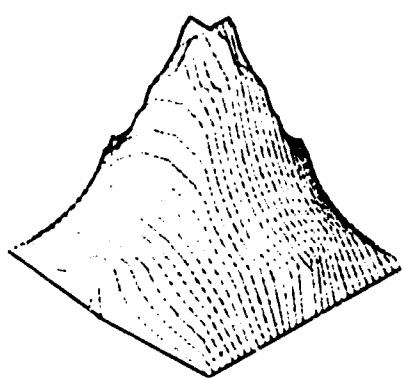


Fig. 55. Erect 60° pyramid image, calculated input data.

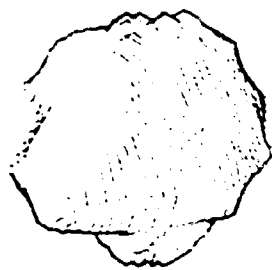


Fig. 56. Forward-facing half 2:1 spheroid image, measured input data.

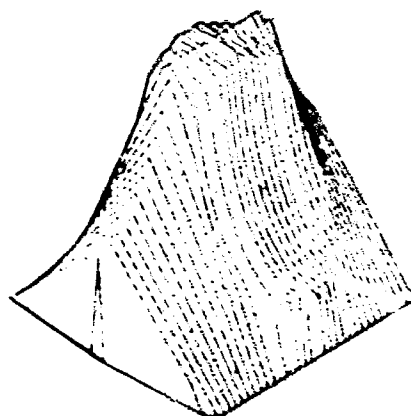


Fig. 57. 1:1 triangular cylinder, calculated input data.

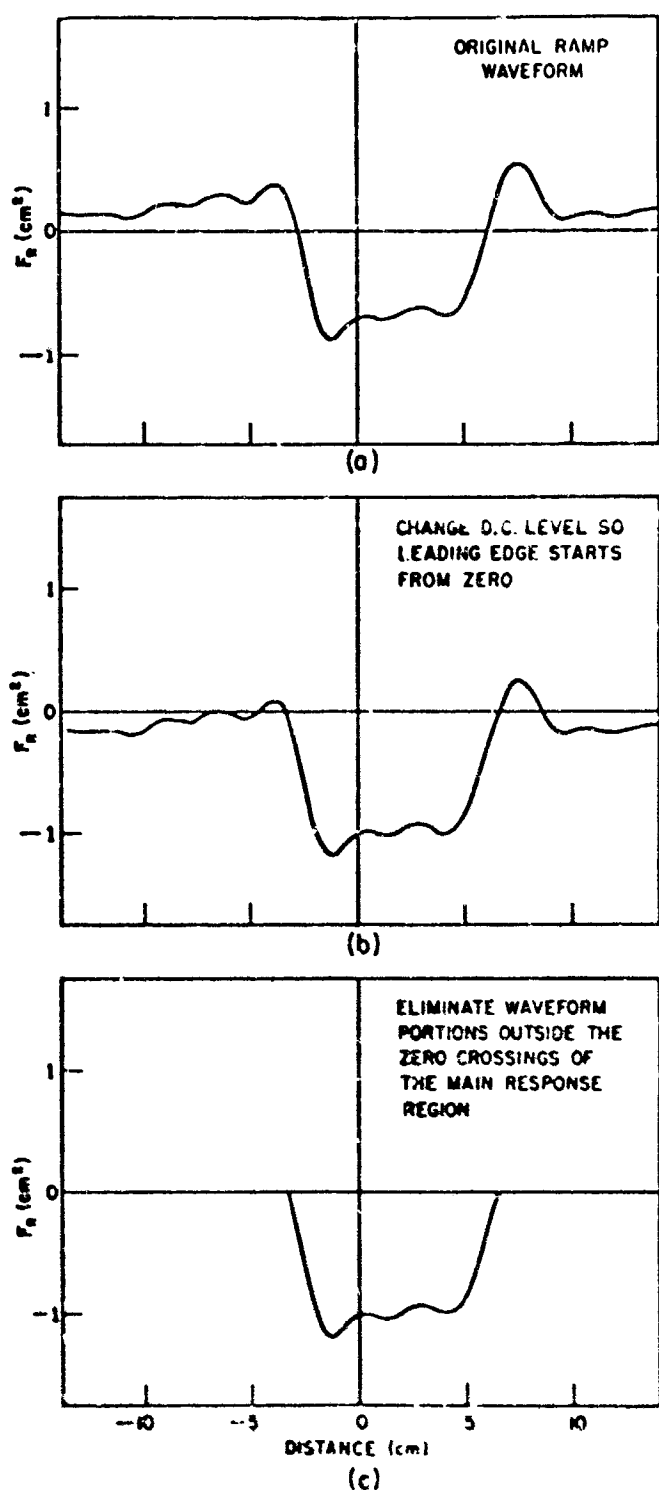


Fig. 58. Modification of ramp waveform for imaging use.

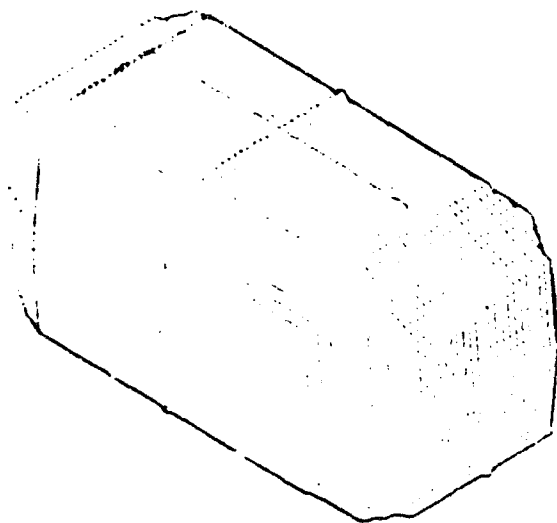


Fig. 59. Image of 2:1 square cylinder, aligned with look angle reference frame, calculated input data.

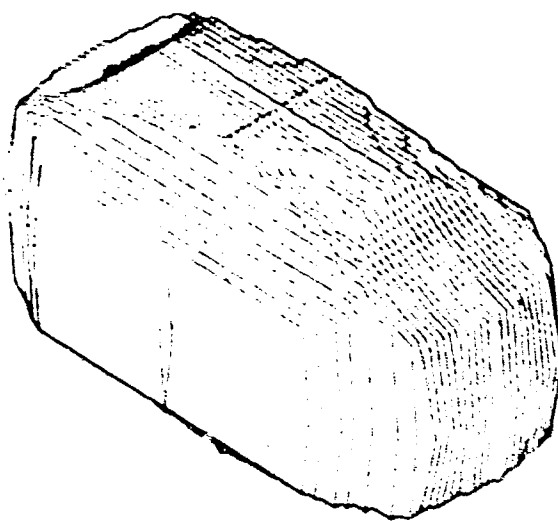


Fig. 60. Image of 2:1 square cylinder, rotated  $7.5^{\circ}$  in YZ plane, calculated input data.

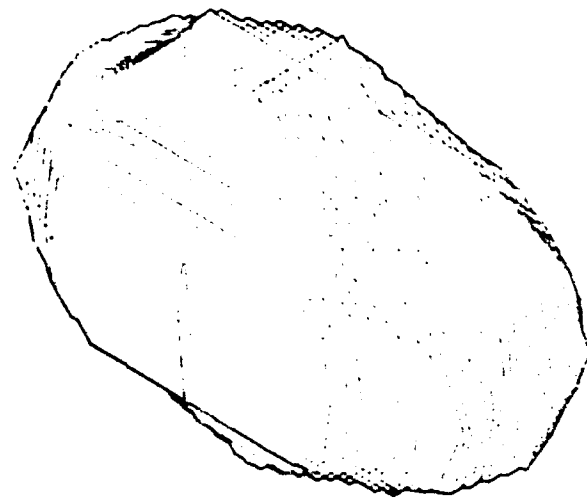


Fig. 61. Image of 2:1 square cylinder, rotated  $15^{\circ}$  in YZ plane,  
calculated input data.

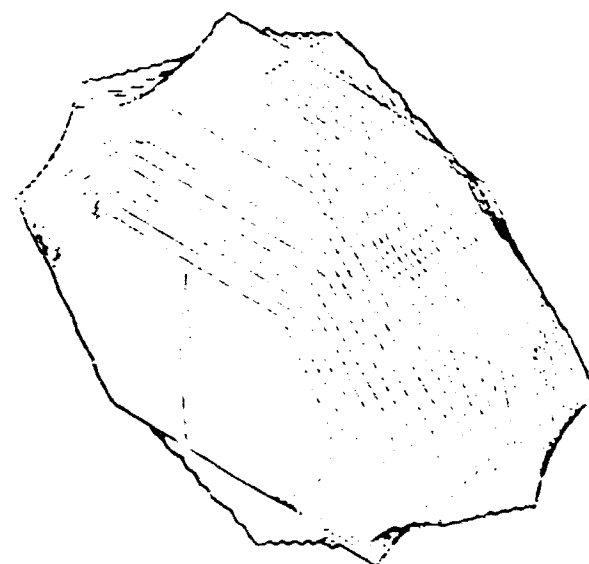


Fig. 62. Image of 2:1 square cylinder, rotated  $30^{\circ}$  in YZ plane,  
calculated input data.

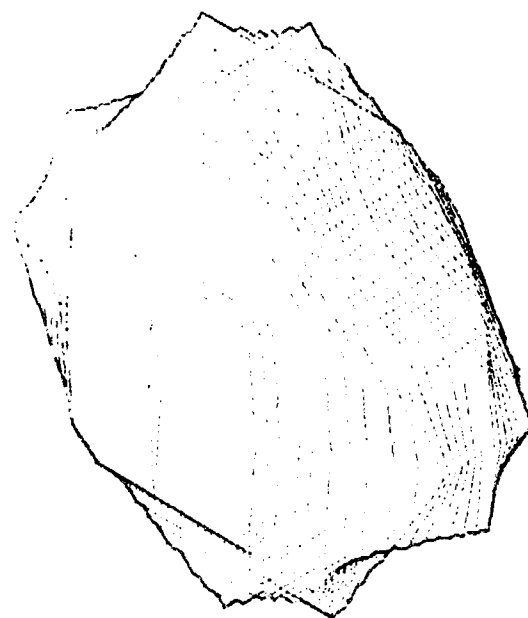


Fig. 63. Image of 2:1 square cylinder, rotated  $45^0$  in YZ plane,  
calculated input data.

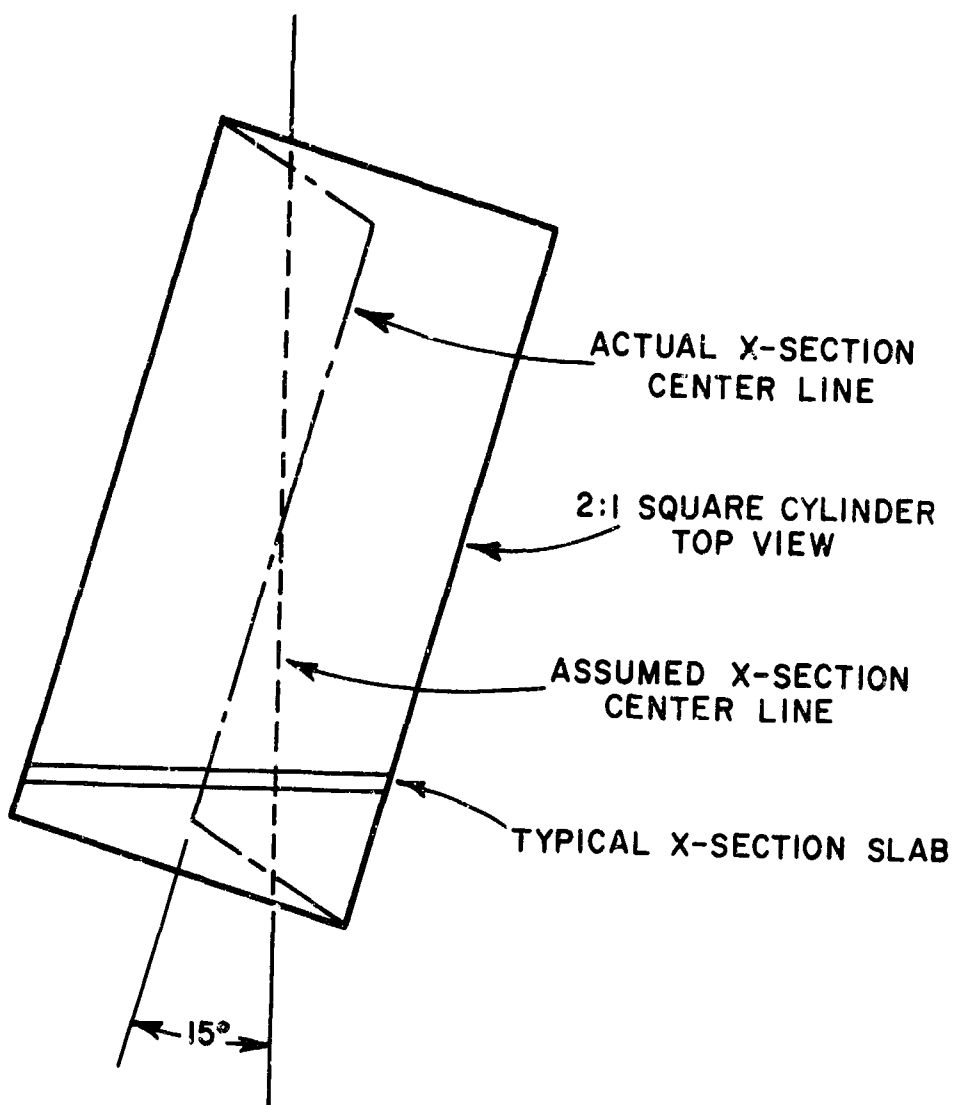


Fig. 64. Center-line of cross-sectional area vs distance for off-axis 2:1 square cylinder, calculated input data.

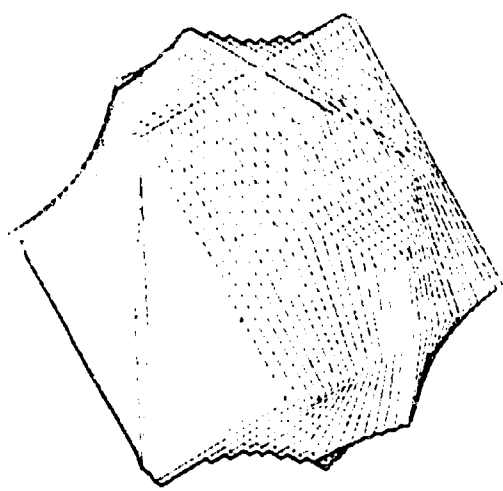


Fig. 65. Image of cube, oriented at  $45^0$  from look angle reference frame, calculated input data.

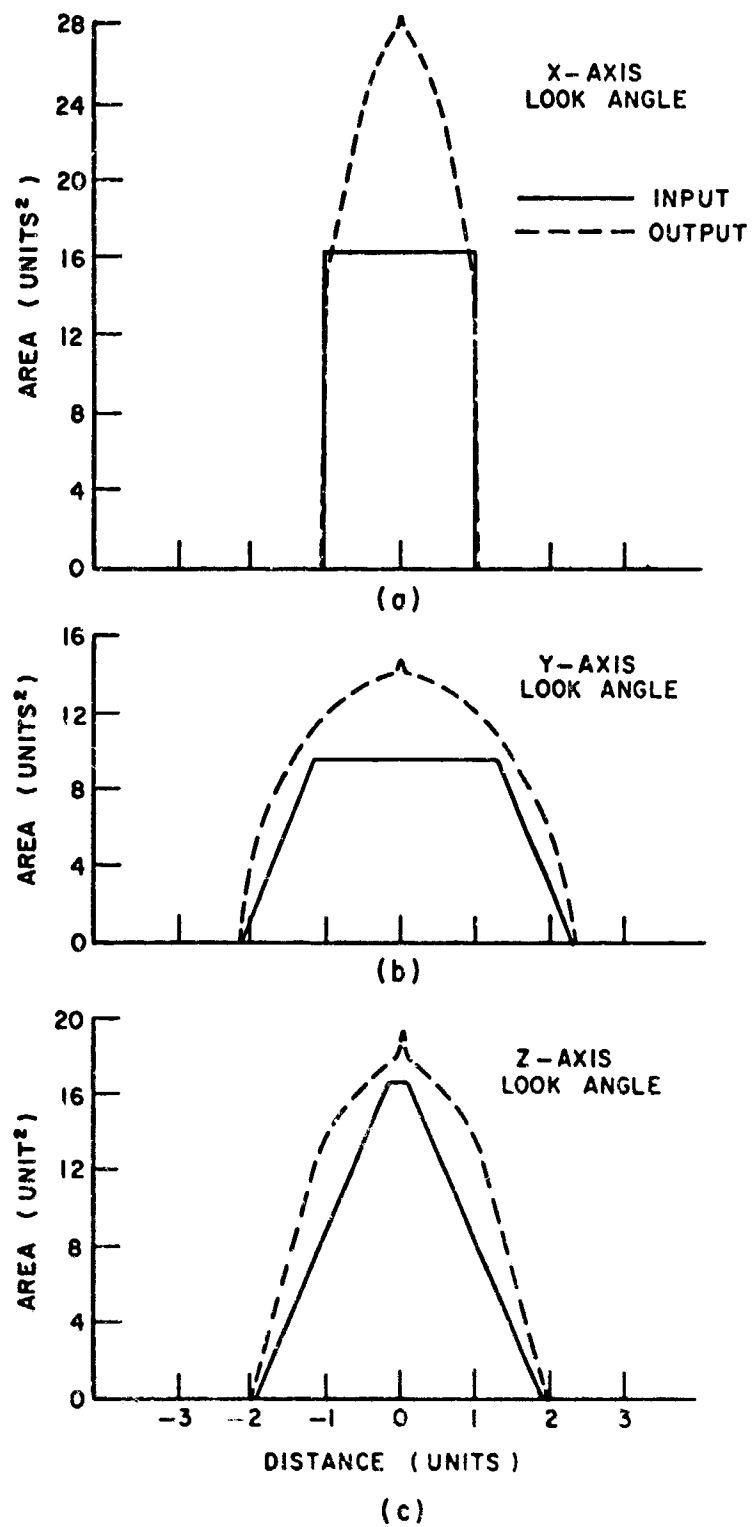


Fig. 66. Input vs output cross-sectional area vs distance waveforms for the image of Fig. 62.

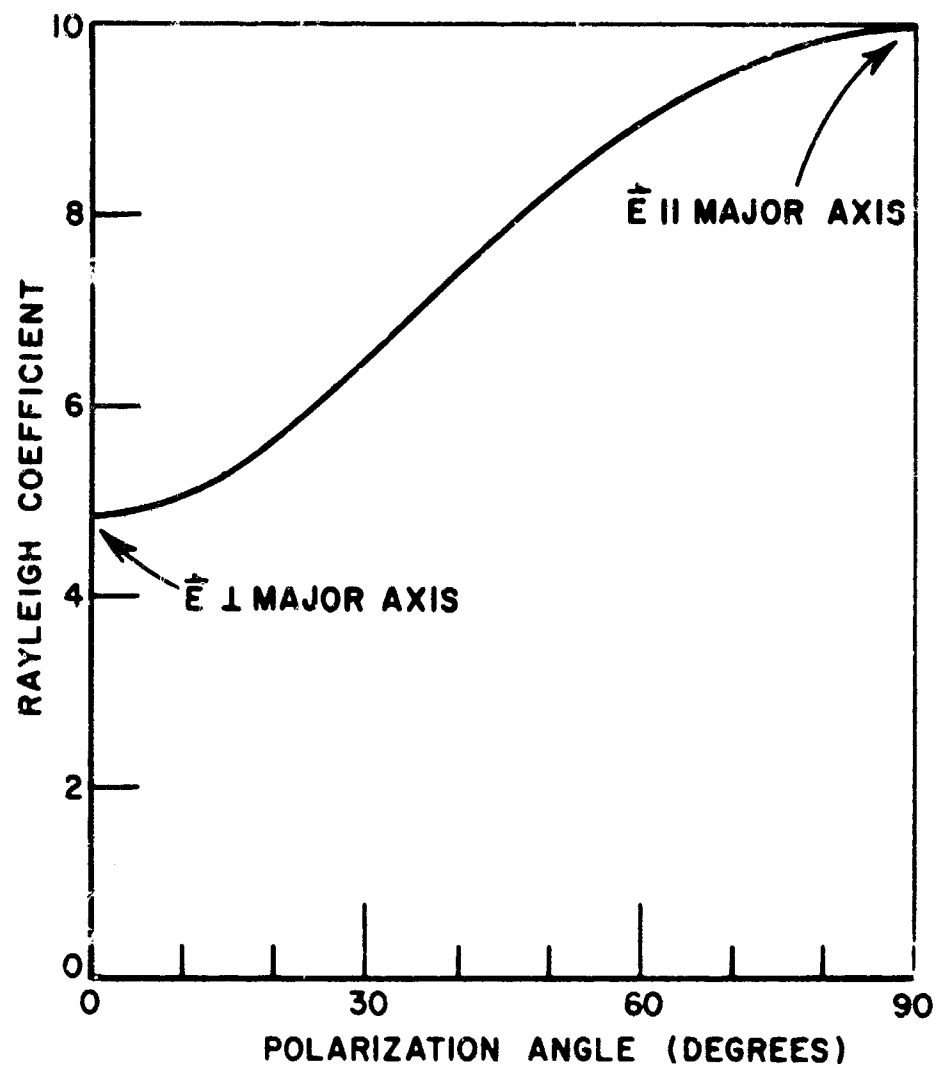


Fig. 67. Rayleigh coefficient vs polarization for 2:1 spheroid.

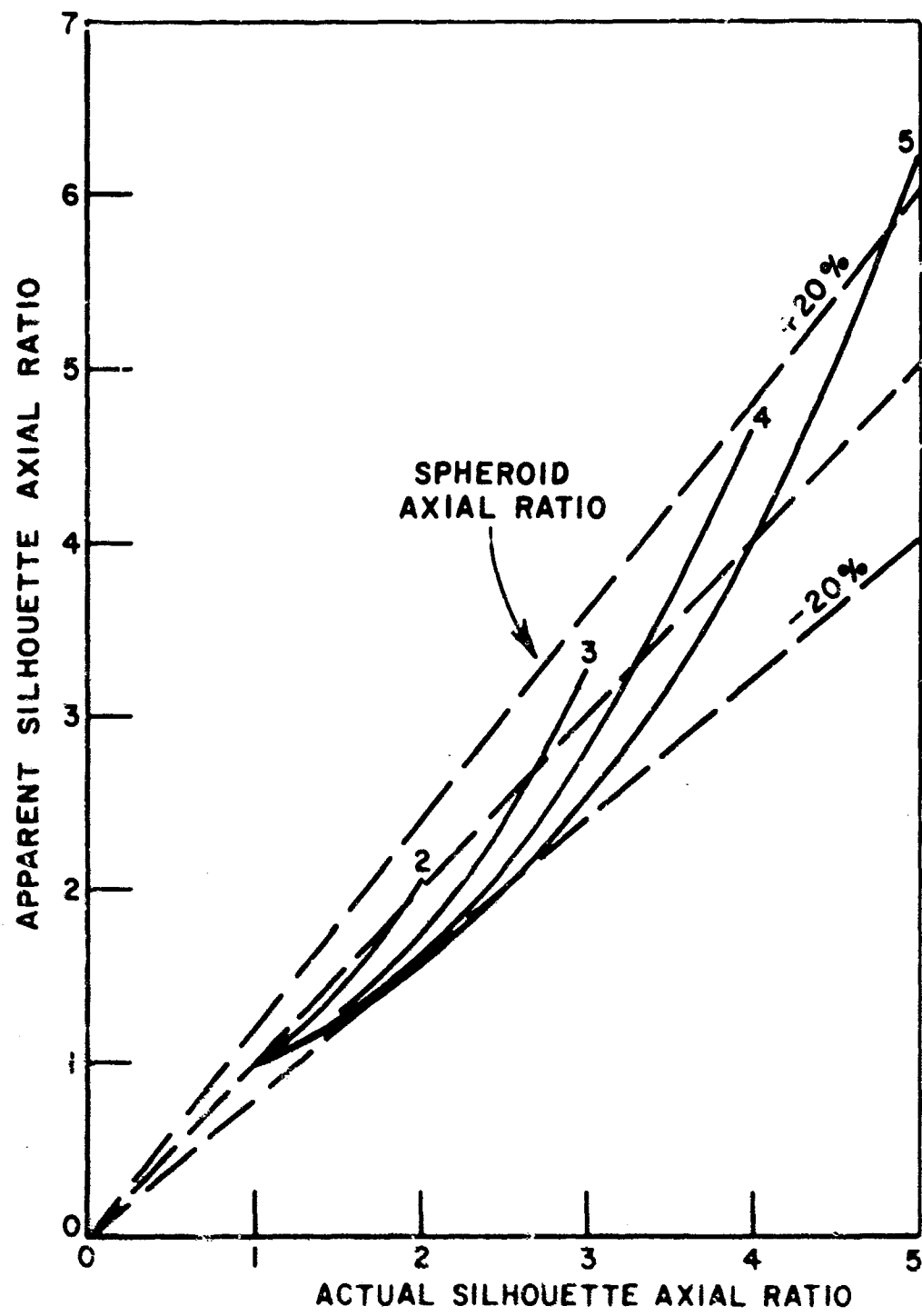


Fig. 68. Max to min Rayleigh coefficient vs silhouette aspect ratio for a 2:1 spheroid.

## V. CONCLUSIONS

Electromagnetic scattering measurements have been made on representative target shapes, using a coherent, harmonically-related ten-frequency system developed for this purpose. The measurements, besides providing quantitative complex spectral scattering data, also furnish characteristic target waveforms for further study of time-domain signature techniques. Analysis of the data has provided insight on the geometrical implications of the time-domain signature, on the feasibility and value of combining resonant region scattering data with short pulse scattering information, and finally on constructing a target image from time domain signature information.

Waveforms generated from the measured data tend to confirm the geometrical characteristics of the ramp response previously demonstrated by sphere and spheroid data. First, the area under the curve is proportional to object volume. In many cases, the waveform amplitude is proportional to the object cross-section vs distance along the line of sight. If the  $E$  field of the interrogating waveform is perpendicular to the major axis of the object silhouette, the constant of proportionality for both cases above is shown to be  $-\pi$ . Furthermore, the ratio of maximum to minimum area under the response waveform as polarization is varied yields information on the orientation and aspect ratio (length/width) of the object silhouette.

Short pulse and resonant region scattering information have been shown to be complimentary, in that the resonant region data is related to the general target shape, while the short pulse data yields information on the scattering centers, which are the important details of the target shape. A new technique for identifying the nature of the scattering centers from short pulse data has been proposed. It has been shown that, if the scattering centers can be identified, then the addition of scattering data at three properly chosen resonance range frequencies to short-pulse derived data results in valid time-domain signature waveforms. Design of a radar system at three frequencies corresponding to realistic target sizes seems feasible as far as propagation is concerned, but needs further study.

An imaging method has been presented which uses ramp response waveforms for three or more look angles to estimate the shape of the target. In its present state, this method obtains excellent images for some objects and orientations, a very simple application of the geometrical aspects of the ramp response. Improvements in the technique, including use of polarization information of short pulse data, should further improve image accuracy for arbitrary targets and orientations. The capabilities of such an improved imaging process, both as a basis for automated identification, and in conjunction with human interpretation, make further study in this area advisable.

In view of the demonstrated physical significance of the time domain signature, in view of the promising techniques for measuring the time domain signature by the addition of a few resonant region measurements to short pulse data, and in view of the new imaging results presented in this report, it is recommended that studies of time domain signature radar identification be continued. Specific areas deserving further effort include:

1. Continue polychromatic radar reflectivity measurements over 10:1 frequency bands for additional space object types. More complex configurations with protruding antennas, etc. are one interesting area for investigation. Further study of target size, orientation, and shape estimation in the presence of system noise, target motion, and small target variations is also recommended.
2. Further study of combined short pulse-resonance region time-domain signature estimates should be undertaken. Computer analysis of appropriate short pulse data to apply the ElectroScience Laboratory scattering center identification technique, and to provide additional combined approximate waveforms for pertinent targets should be included in such a study. A comparison of measured results using such a technique with theoretically predicted impulse waveforms for some pertinent targets would also be interesting.
3. Development of imaging techniques utilizing time-domain signature information. Areas for future study include; 1) polarization information, 2) non-orthogonal look angles, and look angle limitations, 3) addition of short-pulse scattering center information to present techniques, and 4) general performance characteristics vs orientation and shape complexity studies.

## REFERENCES

1. Kennaugh, E.M. and Cosgriff, R.L., "The Use of Impulse Response in Electromagnetic Scattering Problems," I.R.E. National Convention Record, Part 1, 1958.
2. Kennaugh, E.M., "The Scattering of Short Electromagnetic Pulses by a Conducting Sphere," Proceedings of the I.R.E., Vol. 49, No. 1, January 1961.
3. Kennaugh, E.M. and Moffatt, D.L., "Transient and Impulse Response Approximations," Proceedings of the IEEE, Vol. 53, No. 8, August 1965.
4. "Measurement and Analysis of Spectral Signatures," Report RADC-TR-70-94, Rome Air Development Center, Air Force Systems Command, Griffiss Air Force Base, New York.
5. Ryan, C.E., Jr., "Diffraction Analysis of Scattering by a Cube with Application to the Time Response Waveforms," Report 2415-3, 13 March 1970, The Ohio State University ElectroScience Laboratory, Department of Electrical Engineering; prepared under Contract F19628-67-C-0239 for Air Force Cambridge Research Laboratories. (AD 702 874)
6. "Short Pulse Theory and Verification Program," Report RADC-TR-70-133, Rome Air Development Center, Air Force Systems Command, Griffiss Air Force Base, New York.
7. Report RADC-TR-70-133, op cit., p. 92.
8. Dietrich, F.J. and Long, R.L., "An Efficient Moderate-Size Vertical Incidence Ionosonde Antenna for 2-20 MHz Polarization Studies," IEEE Transactions on Antennas and Propagation, Vol. AP-17, No. 5, September 1969.
9. Breeding, K.J. and Ksienki, A.A., "The Inverse Scattering and Target Identification Problem," Report 2768-4, 4 November 1970, The Ohio State University ElectroScience Laboratory, Department of Electrical Engineering; prepared under Contract AFOSR 69-1710A, Department of the Air Force, Air Force Office of Scientific Research, Arlington, Virginia, 22209.
10. Hodge, D.B., "Spectral and Transient Response of a Circular Disk to Plane Electromagnetic Waves," Report 2415-5, 28 May 1970, The Ohio State University ElectroScience Laboratory, Department of Electrical Engineering; prepared under Contract F19628-67-C-0239, Air Force Cambridge Research Laboratories. (AD 707 493)

11. Hill, D.A., "Electromagnetic Scattering Concepts Applied to the Detection of Targets Near the Ground," Report 2971-1, 4 September 1970, The Ohio State University ElectroScience Laboratory, Department of Electrical Engineering; prepared under Contract F19628-70-C-0125, Air Force Systems Command, Laurence G. Hanscom Field, Bedford, Massachusetts.
12. Bojarski, N.N., "Three-Dimensional Electromagnetic Short Pulse Inverse Scattering," Syracuse University Res. Corp., Syracuse, New York, February, 1967.
13. Lewis, R.M., "Physical Optics Inverse Diffraction," IEEE Trans. on Antennas and Propagation, Vol. AP-17, No. 3, May 1969.

## APPENDIX

This section presents the tabulated complex scattering data measured for the targets of Figs. 1-8. Values of normalized complex square-root of cross-section, in cm, are presented for two orthogonal linearly polarized interrogating signals, at frequencies of 1.092, 2.164, ... 10.82 GHz.

The phase reference for these data is approximately, but not exactly at the centroid of the target. Specifically, the styrofoam holders for the targets were designed to accommodate a set of spheres as well. For the 2:1 cylinder and its modified versions (Figs. 1-4) the center of the sphere was located as exactly as possible at the centroid of the 2:1 cylinder portion of the target. For the other targets, the sphere centers were located as near as possible to the centroid of the total shape. The actual zero-phase point, then, is the center of the reference spheres.

The accuracy of these data was estimated by measuring at least two reference spheres along with each target measurement trial. Then after the data was normalized using one reference sphere, the experimental values obtained for the "check" sphere(s) were compared with calculated data to provide an accuracy estimate.

Two sets of accuracy estimates apply to these data. Prior to January, 1971 the system microwave hardware and range configuration were adjusted to a compromise situation to yield satisfactory accuracy and minimum measurement time. Maximum deviation estimates for the above arrangement are given in Table A-1.

TABLE A-1

Frequency	Amplitude Accuracy	Phase Accuracy
1.08 GHz	±10%	±10°
2.16	±10%	±100°
3.24	±10%	±10°
4.32	±20%	±20°
5.40	±10%	±100°
6.48	±10%	±100°
7.56	±10%	±100°
8.64	±20%	±200°
9.72	±20%	±200°
10.80	±20%	±200°

As the waveforms in the text indicate, these accuracy levels are sufficient to assure adequate ramp response waveforms.

More recently, repeated measurement runs with the system optimized for different frequencies have resulted in the accuracies given in Table A-2.

TABLE A-2

Frequency	Amplitude Accuracy	Phase Accuracy
1.08	±10%	±10°
2.16	±10%	±10°
3.24	±10%	±10°
4.32	±10%	±10°
5.40	±10%	±10°
6.48	±10%	±10°
7.56	±10%	±10°
8.64	±10%	±10°
9.72	±10%	±10°
10.80	±10%	±10°

The tables of these data are denoted by an asterisk. Such data is considered suitable for step and impulse as well as ramp response waveforms.

TABLE A-3  
2:1 CYLINDER,  $\phi$  POLARIZATION,  
COMPLEX RETURN VS  $\theta$

Frequency (GHz)	A(cm)	$\theta=0^\circ$		$\theta=15^\circ$		$\theta=30^\circ$		$\theta=45^\circ$		$\theta=60^\circ$		$\theta=75^\circ$		$\theta=90^\circ$	
		$\phi$	A(cm)	$\phi$	A(cm)	$\phi$	A(cm)	$\phi$	A(cm)	$\phi$	A(cm)	$\phi$	A(cm)	$\phi$	A(cm)
1.08	1	487	361	778	336	631	329	687	357	696	4	775	31	740	12
2.16	2	1.58	329	1.63	329	1.74	328	1.95	331	2.22	336	2.49	341	5.89	343
3.24	3	944	309	1.04	255	1.63	292	2.63	300	3.72	312	4.75	323	5.82	325
4.32	4	2.08	109	2.02	111	1.03	123	643	271	2.54	304	4.35	323	4.91	350
5.40	5	4.53	72	4.53	70	4.18	76	2.56	81	859	349	3.59	321	4.69	341
6.48	6	2.32	51	2.63	45	3.74	52	3.88	72	1.68	51	3.60	348	4.39	18
7.56	7	2.80	99	2.12	189	.592	120	1.89	61	1.86	54	1.94	18	2.72	18
8.64	8	5.50	173	5.04	168	3.46	158	1.55	132	.86	63	3.05	33	4.32	51
9.72	9	3.19	191	4.01	179	3.06	158	1.87	150	.759	159	2.00	36	5.35	75
10.80	10	4.50	251	1.15	42	.394	.2	.877	355	1.30	81	5.48	225	5.26	99

TABLE A-4  
2:1 CYLINDER,  $\theta$  POLARIZATION,  
COMPLEX RETURN VS  $\theta$

Frequency (GHz)	A(cm)	$\theta=0^\circ$		$\theta=15^\circ$		$\theta=30^\circ$		$\theta=45^\circ$		$\theta=60^\circ$		$\theta=75^\circ$		$\theta=90^\circ$	
		$\phi$	A(cm)	$\phi$	A(cm)	$\phi$	A(cm)	$\phi$	A(cm)	$\phi$	A(cm)	$\phi$	A(cm)	$\phi$	A(cm)
1.08	1	.626	345	.629	356	.833	348	.933	336	1.23	351	1.36	350	1.42	352
2.16	2	1.40	0	1.69	337	2.72	30	4.15	327	5.82	327	6.91	329	7.51	333
3.24	3	0.787	355	1.00	320	1.73	271	3.70	238	5.75	286	7.10	289	8.01	293
4.32	4	2.05	159	1.86	142	1.43	136	2.17	253	3.76	101	4.66	116	5.24	304
5.40	5	3.74	114	3.81	118	3.36	128	1.47	133	1.68	326	3.91	339	4.78	348
6.48	6	0.916	153	1.17	135	2.94	106	2.82	111	1.06	352	2.90	356	3.38	16
7.56	7	2.45	227	1.41	219	2.71	108	3.48	121	5.77	1	3.74	9	4.78	313
8.64	8	4.74	210	4.09	232	1.59	208	2.15	132	0.634	177	2.75	291	4.70	294
9.72	9	4.06	203	6.86	246	2.49	286	1.57	138	1.86	167	3.89	349	5.27	315
10.80	10	5.44	4	3.74	37	1.37	68	1.45	113	2.88	98	1.32	71	3.70	105

TABLE A-5  
SPHERE-CAPPED CYLINDER,  $\phi$  POLARIZATION  
COMPLEX RETURN VS  $\theta$

Frequency (GHz)	$\theta=0^\circ$		$\theta=30^\circ$		$\theta=45^\circ$		$\theta=60^\circ$		$\theta=90^\circ$		$\theta=120^\circ$		$\theta=135^\circ$		$\theta=150^\circ$		$\theta=180^\circ$		
	$A(cm)$	$\phi$	$A(cm)$	$\phi$	$A(cm)$	$\phi$	$A(cm)$	$\phi$	$A(cm)$	$\phi$	$A(cm)$	$\phi$	$A(cm)$	$\phi$	$A(cm)$	$\phi$	$A(cm)$	$\phi$	
1.08	1	0.805	351	0.548	12	0.715	358	0.802	29	0.706	27	0.738	12	0.614	30	0.75	19	0.67	15
2.16	2	1.40	340	1.56	348	2.02	334	2.31	339	2.76	348	2.49	355	2.03	1.68	7	1.34	13	
3.24	3	0.183	162	0.702	312	1.74	312	3.13	327	4.83	343	3.29	354	1.97	359	0.861	356	0.03	158
4.32	4	3.09	134	2.41	139	5.03	158	1.67	312	5.49	340	2.49	342	3	1.90	121	1.81	2.92	190
5.40	5	3.01	105	3.57	109	3.21	113	1.01	86	5.86	342	1.52	55	2.74	151	3.75	176	3.32	194
6.48	6	0.737	323	1.13	94	2.27	114	1.98	98	5.29	1	1.75	112	2.01	165	2.23	204	0.972	264
7.56	7	4.43	263	3.01	261	0.929	198	1.81	104	3.40	24	1.79	141	1.28	202	2.12	308	4.12	345
8.64	8	2.44	231	3.05	239	2.21	221	1.35	145	4.33	57	1.24	147	2.16	282	3.38	330	3.97	19
9.72	9	3.06	56	0.385	200	0.980	253	2.20	202	6.72	63	0.535	235	1.92	330	2.82	0	3.81	115
10.80	10	0.63	153	1.75	26	1.70	170	3.89	3	6.50	1	2.37	55	1.42	186	11.81	92	3.60	2

TABLE A-6  
SPHERE-CAPPED CYLINDER,  $\theta$  POLARIZATION  
COMPLEX RETURN VS  $\theta$

Frequency (GHz)	$\theta=0^\circ$		$\theta=30^\circ$		$\theta=45^\circ$		$\theta=60^\circ$		$\theta=90^\circ$		$\theta=120^\circ$		$\theta=135^\circ$		$\theta=150^\circ$		$\theta=180^\circ$		
	$A(cm)$	$\phi$	$A(cm)$	$\phi$	$A(cm)$	$\phi$	$A(cm)$	$\phi$	$A(cm)$	$\phi$	$A(cm)$	$\phi$	$A(cm)$	$\phi$	$A(cm)$	$\phi$	$A(cm)$	$\phi$	
1.08	1	0.55	358	1.00	352	1.25	351	1.75	355	1.24	4	1.60	349	1.28	353	0.994	355	0.61	5
2.16	2	1.19	357	2.79	331	5.04	321	6.84	319	10.5	298	7.45	319	2.93	326	1.22	328	1.22	1C
3.24	3	0.48	147	1.31	267	3.40	283	4.98	271	8.79	256	5.07	287	3.12	290	1.18	294	2.22	97
4.32	4	2.0	141	2.73	175	1.75	194	2.24	268	0.64	45	2.42	292	1.36	196	2.25	166	2.67	165
5.40	5	2.32	144	3.99	149	3.20	151	0.335	125	2.31	335	7	149	3.65	145	1.45	2.66	191	
6.48	6	1.01	326	1.57	138	2.74	149	0.398	155	6.98	339	1.28	36	2.49	156	2.05	1.67	1.19	290
7.56	7	3.36	315	1.74	359	1.51	175	2.03	203	5.47	30	0.691	70	1.57	204	1.86	241	3.53	339
8.64	8	2.01	313	3.20	351	0.56	217	2.60	217	5.25	50	0.477	154	1.71	238	2.32	286	3.8	2
9.72	9	1.59	312	2.84	352	1.42	64	2.48	206	6.54	97	0.186	318	1.08	275	1.60	350	3.04	70
10.80	10	2.75	330	0.33	281	.006	298	6.62	313	6.09	197	3.04	132	0.0135	291	4.44	328	3.1	316

TABLE A-7  
CONE CYLINDER,  $\phi$  POLARIZATION  
COMPLEX RETURN VS  $\theta$

Frequency (GHz)	$A(\text{cm})$	$\theta=0^\circ$	$A(\text{cm})$	$\theta=30^\circ$	$A(\text{cm})$	$\theta=60^\circ$	$A(\text{cm})$	$\theta=90^\circ$	$A(\text{cm})$	$\theta=120^\circ$	$A(\text{cm})$	$\theta=150^\circ$	$A(\text{cm})$	$\theta=180^\circ$	
		$\phi$		$\phi$		$\phi$		$\phi$		$\phi$		$\phi$		$\phi$	
1.08	1	0.547	349	0.587	359	0.944	17	0.905	29	0.761	34	0.675	19	0.622	357
2.16	2	1.35	339	1.59	341	2.27	340	2.59	355	2.27	6	1.66	18	1.36	21
3.24	3	0.266	216	0.828	308	3.26	330	5.05	356	3.26	14	0.90	32	3.212	82
4.32	4	2.73	122	1.96	136	2.02	309	5.73	342	2.40	14	1.59	185	2.44	195
5.40	5	2.77	92	3.18	105	0.615	13	5.41	358	1.27	80	3.29	205	3.08	218
6.48	6	1.25	298	0.884	46	1.67	89	3.89	3	1.78	137	2.14	229	1.83	286
7.56	7	3.17	259	1.95	271	1.62	114	3.31	41	1.84	173	1.74	334	3.27	10
8.64	8	3.12	219	2.72	238	1.20	183	5.68	91	1.32	196	3.66	13	4.59	58
9.72	9	1.24	129	0.870	219	0.219	215	5.87	105	0.636	267	2.20	66	3.34	115
10.80	10	1.34	169	0.976	60	1.55	273	4.94	244	15.5	207	6.16	159	6.34	192

TABLE A-8  
CONE-CYLINDER,  $\theta$  POLARIZATION  
COMPLEX RETURN VS  $\theta$

Frequency (GHz)	$A(\text{cm})$	$\theta=0^\circ$	$A(\text{cm})$	$\theta=30^\circ$	$A(\text{cm})$	$\theta=60^\circ$	$A(\text{cm})$	$\theta=90^\circ$	$A(\text{cm})$	$\theta=120^\circ$	$A(\text{cm})$	$\theta=150^\circ$	$A(\text{cm})$	$\theta=180^\circ$	
		$\phi$		$\phi$		$\phi$		$\phi$		$\phi$		$\phi$		$\phi$	
1.08	1	0.591	347	0.892	3	1.66	349	2.09	355	1.70	1	1.01	17	0.808	34
2.16	2	1.24	345	3.14	310	7.80	309	10.3	314	7.37	321	2.71	342	1.31	21
3.24	3	0.233	264	1.61	249	5.28	270	7.79	285	4.85	290	0.699	302	0.416	62
4.32	4	2.43	129	2.24	151	2.39	250	6.02	303	1.37	283	2.66	173	2.39	203
5.40	5	2.57	92	3.80	112	0.747	39	6.02	332	1.93	69	2.41	170	3.55	221
6.48	6	0.352	181	1.81	123	0.452	94	4.93	4	1.45	88	2.30	253	1.72	293
7.56	7	3.11	246	1.56	325	2.44	164	6.66	20	2.20	80	4.43	282	4.03	20
8.64	8	2.29	205	2.45	285	3.14	178	6.47	39	0.728	30	1.21	302	4.22	50
9.72	9	1.53	271	2.49	347	4.64	200	6.65	59	0.458	351	1.01	55	1.47	201
10.80	10	2.49	134	3.68	219	4.83	137	10.76	126	1.76	177	5.99	352	6.50	69

TABLE A-9  
STEP CYLINDER,  $\phi$  POLARIZATION  
COMPLEX RETURN VS  $\theta$

Frequency (GHz)	$\theta=0^\circ$ A(cm) $\phi$	$\theta=30^\circ$ A(cm) $\phi$	$\theta=60^\circ$ A(cm) $\phi$	$\theta=90^\circ$ A(cm) $\phi$	$\theta=120^\circ$ A(cm) $\phi$	$\theta=150^\circ$ A(cm) $\phi$	$\theta=180^\circ$ A(cm) $\phi$
1.08	1	616	352	662	1	0.928	49
2.16	2	1.28	341	1.54	342	1.00	18
3.24	3	524	212	0.783	292	2.25	343
4.32	4	2.46	129	2.01	151	3.23	333
5.40	5	2.44	75	2.57	106	0.646	130
6.48	6	2.39	329	1.44	1	1.42	109
7.56	7	1.42	267	1.92	318	1.12	218
8.64	8	5.21	167	0.792	157	1.68	227
9.72	9	4.58	147	2.15	126	0.30	243
10.80	10	2.03	256	1.88	212	0.55	332

TABLE A-10  
STEP CYLINDER,  $\theta$  POLARIZATION  
COMPLEX RETURN VS  $\theta$

Frequency (GHz)	$\theta=0^\circ$ A(cm) $\phi$	$\theta=30^\circ$ A(cm) $\phi$	$\theta=60^\circ$ A(cm) $\phi$	$\theta=90^\circ$ A(cm) $\phi$	$\theta=120^\circ$ A(cm) $\phi$	$\theta=150^\circ$ A(cm) $\phi$	$\theta=180^\circ$ A(cm) $\phi$
1.08	1	0.616	352	0.955	2	1.77	351
2.16	2	1.26	344	2.22	309	8.25	306
3.24	3	0.379	225	1.75	245	5.35	274
4.32	4	2.09	141	2.48	150	1.74	251
5.40	5	0.09	75	3.36	112	1.31	29
6.48	6	0.634	17	1.08	124	0.904	80
7.56	7	1.01	268	2.19	344	2.21	147
8.64	8	4.24	143	1.67	308	2.79	169
9.72	9	2.37	127	1.09	3	5.21	184
10.80	10	6.61	158	6.80	252	4.23	120

TABLE A-11  
CUBE,  $\phi = 0$ ,  $\phi$  POLARIZATION  
COMPLEX RETURN VS  $\theta$

Frequency (GHz)	$\theta=0^\circ$		$\theta=15^\circ$		$\theta=30^\circ$		$\theta=45^\circ$	
	A(cm)	$\phi$	A(cm)	$\phi$	A(cm)	$\phi$	A(cm)	$\phi$
1.08	1	2.02	2	2.02	356	2.05	4	2.02
2.16	2	6.30	339	6.24	337	6.38	339	6.18
3.24	3	4.04	320	3.92	317	4.36	316	4.44
4.32	4	5.67	90	5.60	97	3.80	92	3.48
5.40	5	9.16	83	8.16	94	6.54	95	4.13
6.48	6	5.27	49	2.08	74	2.69	223	3.19
7.56	7	7.16	141	5.85	144	3.68	174	3.63
8.64	8	7.05	211	5.55	219	2.66	223	1.78
9.72	9	7.59	219	8.67	138	2.21	350	0.663
10.80	10	4.27	138	1.87	84	3.81	189	5.17

TABLE A-12  
CUBE,  $\phi = 0^\circ$ ,  $\theta$  POLARIZATION  
COMPLEX RETURN VS  $\theta$

Frequency (GHz)	$\theta=0^\circ$		$\theta=15^\circ$		$\theta=30^\circ$		$\theta=45^\circ$	
	A(cm)	$\phi$	A(cm)	$\phi$	A(cm)	$\phi$	A(cm)	$\phi$
1.08	1	2.41	0	2.26	357	2.07	359	2.09
2.16	2	6.08	341	6.17	340	6.47	341	6.52
3.24	3	4.02	334	4.79	330	6.19	332	6.87
4.32	4	5.24	84	3.82	72	3.17	348	4.88
5.40	5	8.47	98	6.80	97	3.44	59	3.36
6.48	6	9.73	123	8.47	124	3.31	88	3.18
7.56	7	7.95	151	7.10	148	2.32	133	3.45
8.64	8	7.75	205	7.23	182	2.89	177	4.68
9.72	9	12.2	268	8.05	239	3.15	193	7.00
10.80	10	24.2	302	8.25	294	3.42	347	3.40

TABLE A-13  
CUBE,  $\phi = 150^\circ$ ,  $\theta$  POLARIZATION\*  
COMPLEX RETURN VS  $\phi$

Frequency (GHz)	$A(cm)$	$\theta=0^\circ$	$A(cm)$	$\theta=15^\circ$	$A(cm)$	$\theta=30^\circ$	$A(cm)$	$\theta=45^\circ$	$A(cm)$	$\theta=60^\circ$	$A(cm)$	$\theta=75^\circ$	$A(cm)$	$\theta=90^\circ$	$A(cm)$	$\phi$
1.08	1	1.86	347	1.90	355	1.85	357	2.03	347	1.85	357	1.87	352	2.24	355	
2.16	2	6.41	331	6.58	329	6.49	329	6.39	330	6.32	332	6.43	336	6.30	339	
3.24	3	4.89	309	4.92	308	4.92	305	4.80	306	4.41	309	4.21	317	3.99	320	
4.32	4	3.29	56	3.06	59	2.65	56	2.90	56	3.96	76	5.26	89	6.14	98	
5.40	5	6.98	69	6.17	64	4.42	52	3.92	42	5.44	64	8.00	83	9.61	96	
6.48	6	7.50	80	5.47	80	1.51	98	3.14	159	2.83	96	6.77	101	9.19	110	
7.56	7	5.74	103	4.19	103	2.44	136	2.76	171	3.51	142	5.66	133	6.79	140	
8.64	8	6.91	146	4.97	145	2.48	162	1.92	214	2.56	189	5.77	190	8.15	206	
9.72	9	6.52	159	4.21	152	1.73	224	2.82	275	0.745	192	6.48	213	10.69	240	
10.80	10	3.55	93	2.95	194	2.66	274	2.60	304	1.72	298	6.52	264	11.23	275	

TABLE A-14  
CUBE,  $\phi = 150^\circ$ ,  $\theta$  POLARIZATION\*  
COMPLEX RETURN VS  $\theta$

Frequency (GHz)	$A(cm)$	$\theta=0^\circ$	$A(cm)$	$\theta=15^\circ$	$A(cm)$	$\theta=30^\circ$	$A(cm)$	$\theta=45^\circ$	$A(cm)$	$\theta=60^\circ$	$A(cm)$	$\theta=75^\circ$	$A(cm)$	$\theta=90^\circ$	$A(cm)$	$\phi$
1.08	1	2.15	344	2.02	353	1.77	342	1.96	354	2.05	352	1.91	359	1.84	359	
2.16	2	6.10	321	6.24	320	6.31	319	6.71	326	6.69	347	6.40	335	6.18	340	
3.24	3	4.23	295	4.74	295	6.44	297	6.59	307	5.77	326	5.07	318	4.20	326	
4.32	4	3.71	44	2.67	20	3.42	320	4.64	314	3.55	339	3.57	49	4.83	95	
5.40	5	7.29	42	5.80	38	3.25	2	3.57	333	3.71	310	6.84	66	9.24	103	
6.48	6	5.08	57	4.57	53	2.59	25	2.03	342	1.94	316	5.64	91	7.37	125	
7.56	7	6.74	86	6.02	76	1.86	50	2.90	289	1.21	86	6.83	123	6.96	128	
8.64	8	5.38	119	4.96	106	1.27	97	3.30	267	2.32	124	7.01	154	6.82	182	
9.72	9	5.45	154	4.53	123	1.23	105	3.09	250	1.41	135	6.04	176	7.04	222	
10.80	10	3.72	8	3.17	146	2.46	133	7.48	62	0.849	152	3.83	239	7.11	271	

TABLE A-15  
CUBE,  $\phi = 30^\circ$ ,  $\theta$  POLARIZATION\*  
COMPLEX RETURN VS  $\theta$

Frequency (GHz)	$\theta = 0^\circ$ $A(\text{cm})$	$\theta = 15^\circ$ $A(\text{cm})$	$\theta = 30^\circ$ $A(\text{cm})$	$\theta = 45^\circ$ $A(\text{cm})$	$\theta = 60^\circ$ $A(\text{cm})$	$\theta = 75^\circ$ $A(\text{cm})$	$\theta = 90^\circ$ $A(\text{cm})$
1.08	1	2.05	359	1.80	353	1.73	354
2.16	2	6.85	331	6.36	326	6.60	329
3.24	3	6.13	311	6.31	304	5.73	306
4.32	4	2.72	352	2.05	350	1.41	355
5.40	5	3.77	46	3.48	38	3.16	29
6.48	6	3.73	51	2.54	45	1.41	23
7.56	7	1.47	96	1.13	84	0.775	122
8.64	8	2.90	161	2.37	140	1.52	140
9.72	9	2.36	144	1.43	154	0.442	248
10.80	10	2.19	109	0.06	83	1.39	266

TABLE A-16  
CUBE,  $\phi = 30^\circ$ ,  $\theta$  POLARIZATION\*  
COMPLEX RETURN VS  $\theta$

Frequency (GHz)	$\theta = 0^\circ$ $A(\text{cm})$	$\theta = 15^\circ$ $A(\text{cm})$	$\theta = 30^\circ$ $A(\text{cm})$	$\theta = 45^\circ$ $A(\text{cm})$	$\theta = 60^\circ$ $A(\text{cm})$	$\theta = 75^\circ$ $A(\text{cm})$	$\theta = 90^\circ$ $A(\text{cm})$
1.08	1	2.10	354	2.02	354	2.05	355
2.16	2	6.47	330	6.43	334	6.58	337
3.24	3	4.40	306	4.68	313	5.82	324
4.32	4	2.76	62	2.27	35	2.96	348
5.40	5	4.87	60	4.12	57	2.84	39
6.48	6	2.29	106	2.66	94	2.35	65
7.56	7	3.11	161	2.84	138	1.28	98
8.64	8	3.08	195	2.31	182	0.794	135
9.72	9	1.59	252	1.34	249	0.266	78
10.80	10	4.98	231	0.55	285	1.07	3

TABLE A-17  
CUBE,  $\phi = 45^\circ$ ,  $\theta$  POLARIZATION\*  
COMPLEX RETURN VS  $\theta$

Frequency (GHz)	$A(\text{cm}) \theta=0^\circ \phi$	$A(\text{cm}) \theta=15^\circ \phi$	$A(\text{cm}) \theta=30^\circ \phi$	$A(\text{cm}) \theta=45^\circ \phi$	$A(\text{cm}) \theta=60^\circ \phi$	$A(\text{cm}) \theta=75^\circ \phi$	$A(\text{cm}) \theta=90^\circ \phi$	
1.08	1 1.97	358	1.84	355	2.15	356	1.78	355
2.16	2 6.80	341	6.89	339	6.63	338	6.51	338
3.24	3 7.04	326	6.72	325	6.16	321	5.50	320
4.32	4 5.14	341	4.67	338	3.49	347	2.32	25
5.40	5 3.63	28	3.33	21	2.95	36	3.63	67
6.48	6 3.80	13	3.20	16	2.25	27	2.72	71
7.56	7 4.02	333	2.47	335	2.43	67	1.63	125
8.64	8 5.14	319	2.99	321	1.30	124	2.00	132
9.72	9 5.32	322	2.39	336	2.07	94	1.41	87
10.80	10 5.89	334	2.77	2	1.78	76	0.744	12

TABLE A-18  
CUBE,  $\phi = 45^\circ$ ,  $\theta$  POLARIZATION\*  
COMPLEX RETURN VS  $\theta$

Frequency (GHz)	$A(\text{cm}) \theta=0^\circ \phi$	$A(\text{cm}) \theta=15^\circ \phi$	$A(\text{cm}) \theta=30^\circ \phi$	$A(\text{cm}) \theta=45^\circ \phi$	$A(\text{cm}) \theta=60^\circ \phi$	$A(\text{cm}) \theta=75^\circ \phi$	$A(\text{cm}) \theta=90^\circ \phi$	
1.08	1 2.03	357	2.06	357	1.92	357	2.04	357
2.16	2 6.17	343	6.31	331	6.30	352	6.58	340
3.24	3 4.46	327	4.87	317	5.53	338	6.34	329
4.32	4 2.46	61	2.08	48	2.54	1	4.17	237
5.40	5 3.65	56	3.52	61	2.86	53	4.74	226
6.48	6 1.20	170	1.13	123	2.00	74	3.70	290
7.56	7 3.20	218	1.78	210	1.07	94	0.36	32
8.64	8 3.63	241	2.19	243	1.31	122	0.371	151
9.72	9 4.14	256	2.42	313	4.52	106	3.55	71
10.80	10 3.81	352	2.73	348	0.849	266	2.03	235

TABLE A-19  
60° CONE, ♦ POLARIZATION  
COMPLEX RETURN VS.  $\theta$

Frequency (GHz)	θ=0°		θ=30°		θ=45°		θ=60°		θ=90°		θ=120°		θ=135°		θ=150°		
	A(cm) ♦																
1.08	1	1.35	1	1.30	2	1.47	357	1.56	359	1.57	356	1.70	350	1.59	359	1.54	348
2.16	2	5.93	345	5.67	345	5.79	348	5.76	345	5.23	342	5.49	337	5.67	335	6.13	337
3.24	3	7.36	215	6.64	338	6.25	325	5.45	326	4.82	319	5.39	309	6.26	317	7.16	316
4.32	4	5.68	265	4.75	290	1.87	319	1.52	21	1.41	54	1.68	276	4.02	298	6.41	320
5.40	5	4.66	267	0.53	306	3.03	77	4.86	88	4.03	67	2.45	113	1.25	97	3.08	356
6.48	6	4.45	311	0.684	10m	3.77	135	5.16	123	3.12	85	2.80	82	2.65	52	2.86	329
7.56	7	3.42	223	0.614	36	1.54	90	3.78	148	0.862	191	0.831	144	1.55	115	1.96	27
8.64	8	3.83	256	0.398	22	3.15	185	5.77	200	2.32	228	1.71	226	1.77	183	1.02	89
9.72	9	4.65	230	0.794	76	3.65	212	5.97	213	0.96	265	1.55	269	2.05	207	1.85	182
10.80	10	4.37	183	1.06	84	1.88	251	5.78	261	2.20	355	1.05	344	1.47	232	1.83	105

TABLE A-20  
60° CONE, ♦ POLARIZATION  
COMPLEX RETURN VS.  $\theta$

Frequency (GHz)	θ=0°		θ=30°		θ=45°		θ=60°		θ=90°		θ=120°		θ=135°		θ=150°		
	A(cm) ♦																
1.08	1	1.79	13	1.64	14	1.63	20	1.38	23	1.46	8	1.48	351	1.50	352	1.47	348
2.16	2	5.75	10	5.62	16	5.01	18	5.01	23	4.93	345	5.36	304	5.62	304	5.96	334
3.24	3	7.04	351	6.08	14	6.43	23	7.42	24	5.53	323	5.88	239	6.03	257	7.36	282
4.32	4	5.66	322	3.69	33	4.49	44	5.15	45	1.80	51	3.47	189	3.16	171	4.37	245
5.40	5	2.23	318	2.83	94	5.19	108	5.85	97	2.34	198	3.32	119	0.887	62	4.40	273
6.48	6	1.34	330	3.07	126	5.20	143	4.94	143	1.93	356	2.26	75	1.06	335	4.15	272
7.56	7	3.22	331	2.61	122	3.30	189	5.20	184	0.332	298	1.41	30	1.31	189	1.92	290
8.64	8	2.54	339	2.56	123	4.10	236	6.81	223	1.13	267	0.642	328	2.65	134	1.02	288
9.72	9	4.39	351	3.81	169	3.43	277	5.69	295	1.47	304	1.60	329	3.26	114	2.21	294
10.80	10	9.07	240	0.739	239	0.66	324	5.03	235	3.72	326	3.00	44	1.62	153	0.246	12

TABLE A-21  
HALF SPHEROID,  $\theta$  POLARIZATION  
COMPLEX RETURN VS  $\theta$

Frequency (GHz)	$\theta=0^\circ$		$\theta=30^\circ$		$\theta=60^\circ$		$\theta=90^\circ$		$\theta=120^\circ$		$\theta=135^\circ$		$\theta=150^\circ$		$\theta=180^\circ$		
	A(cm)	$\phi$	A(cm)	$\phi$	A(cm)	$\phi$	A(cm)	$\phi$	A(cm)	$\phi$	A(cm)	$\phi$	A(cm)	$\phi$	A(cm)	$\phi$	
1.00	1	0.56	329	0.624	13	0.525	347	0.526	359	0.569	358	0.532	2	0.522	3	0.627	6
2.16	2	1.96	348	2.05	341	2.07	343	2.05	344	1.92	350	2.04	357	1.96	359	1.82	356
3.24	3	3.78	327	3.79	324	3.83	326	3.82	328	3.93	337	3.38	341	3.74	347	3.79	353
4.32	4	5.68	272	5.09	291	4.73	287	5.17	300	5.82	311	5.70	327	5.83	338	6.30	337
5.40	5	7.51	265	2.06	279	2.26	292	2.40	306	2.86	322	2.86	331	2.78	342	2.95	357
6.48	6	9.34	184	1.37	172	1.07	303	1.07	319	1.40	6	0.823	319	1.63	4	2.09	33
7.56	7	1.01	130	2.12	112	2.02	60	2.62	60	2.25	56	1.03	88	1.29	76	2.64	66
8.64	8	1.14	125	2.14	88	2.64	62	3.54	59	2.94	80	1.80	125	1.86	104	4.30	104
9.72	9	2.26	115	1.09	103	1.46	68	2.91	57	2.62	82	1.62	130	1.08	116	2.66	88
10.80	10	0.629	94	0.741	173	0.634	131	1.57	92	1.80	106	0.951	144	0.733	150	1.55	124

TABLE A-22  
HALF SPHEROID,  $\theta$  POLARIZATION  
COMPLEX RETURN VS  $\theta$

Frequency (GHz)	$\theta=0^\circ$		$\theta=30^\circ$		$\theta=60^\circ$		$\theta=90^\circ$		$\theta=120^\circ$		$\theta=135^\circ$		$\theta=150^\circ$		$\theta=180^\circ$		
	A(cm)	$\phi$	A(cm)	$\phi$	A(cm)	$\phi$	A(cm)	$\phi$	A(cm)	$\phi$	A(cm)	$\phi$	A(cm)	$\phi$	A(cm)	$\phi$	
1.00	1	0.538	40	0.684	30	0.485	19	0.573	395	0.774	44	0.912	2	0.481	359	3.496	357
2.16	2	1.87	344	2.02	348	2.05	354	2.08	352	2.15	351	2.07	352	2.07	355	1.98	359
3.24	3	3.41	325	3.90	328	3.99	336	4.33	334	4.47	332	4.01	330	4.24	337	3.78	348
4.32	4	5.25	290	1.05	304	1.28	310	3.47	313	3.20	304	2.47	301	2.45	309	2.40	325
5.40	5	7.11	267	2.91	309	3.74	328	3.92	336	2.79	321	2.98	324	3.00	334	2.24	325
6.48	6	8.40	178	1.14	352	2.86	35	3.16	356	3.41	340	2.52	340	1.97	21	3.75	28
7.56	7	2.20	132	0.302	58	1.72	13	2.93	13	2.02	54	2.23	200	2.69	206	2.90	39
8.64	8	2.70	138	0.150	83	2.19	34	3.48	44	2.81	66	1.02	119	1.22	68	5.24	72
9.72	9	5.23	212	1.43	192	2.32	63	5.52	93	4.46	100	1.51	133	1.46	86	3.52	93
10.80	10	0.469	99	0.742	42	0.762	331	5.02	151	6.45	135	1.62	200	1.31	195	1.59	155

TABLE A-23  
 LARGE SPHERE-CAPPED CYLINDER WITH STUB  
 $\psi = 0$ ,  $\phi$  POLARIZATION  
 COMPLEX RETURN VS  $\epsilon$

Frequency (GHz)		$\theta=0^\circ$		$\theta=10^\circ$		$\theta=20^\circ$		$\theta=90^\circ$	
		A(cm)	$\phi$	A(cm)	$\phi$	A(cm)	$\phi$	A(cm)	$\phi$
1.08	1	3.14	248	2.64	256	1.76	259	10.77	10 <sup>0</sup>
2.16	2	10.67	147	10.63	146	10.48	137	19.58	10 <sup>0</sup>
3.24	3	6.43	25	7.21	21	8.39	5	16.17	91 <sup>0</sup>
4.32	4	4.60	82	3.80	59	3.62	340	24.29	142 <sup>0</sup>
5.40	5	8.52	0	7.34	342	5.49	294	19.87	209 <sup>0</sup>
6.48	6	4.38	312	3.22	310	1.82	240	32.53	289 <sup>0</sup>
7.56	7	5.44	251	6.26	266	5.09	197	26.78	347 <sup>0</sup>
8.64	8	1.93	259	2.77	230	4.35	142	29.42	51 <sup>0</sup>
9.72	9	6.48	223	4.50	220	4.78	82	42.24	118 <sup>0</sup>
10.80	10	1.86	94	3.40	125	1.64	72	15.54	144 <sup>0</sup>

TABLE A-24  
 LARGE SPHERE-CAPPED CYLINDER WITH STUB,  
 $\psi = 90^\circ$ ,  $\phi$  POLARIZATION  
 COMPLEX RETURN VS  $\theta$

Frequency (GHz)		$\theta=0^\circ$		$\theta=10^\circ$		$\theta=20^\circ$		$\theta=90^\circ$	
		A(cm)	$\phi$	A(cm)	$\phi$	A(cm)	$\phi$	A(cm)	$\phi$
1.08	1	2.27	285	2.40	295	2.30	317	12.38	12 <sup>0</sup>
2.16	2	4.76	59	4.35	64	4.26	59	16.78	354 <sup>0</sup>
3.24	3	10.50	44	11.15	38	11.44	20	14.93	102 <sup>0</sup>
4.32	4	8.05	82	6.97	79	4.65	28	26.06	150 <sup>0</sup>
5.40	5	4.70	4	3.63	350	4.19	264	22.45	210 <sup>0</sup>
6.48	6	6.54	292	5.46	295	4.83	246	32.19	281 <sup>0</sup>
7.56	7	8.08	302	8.89	277	5.64	244	25.22	342 <sup>0</sup>
8.64	8	2.74	358	0.813	266	2.40	108	27.77	55 <sup>0</sup>
9.72	9	6.13	204	5.24	155	9.56	94	35.20	114 <sup>0</sup>
10.80	10	2.48	150	1.90	71	8.59	124	9.51	150 <sup>0</sup>